EL 94

ACTA POLYTECHNICA SCANDINAVICA

ELECTRICAL ENGINEERING SERIES No. 94

Robust Control of Magnetic Bearings in Subcritical Machines

ERKKI LANTTO

Helsinki University of Technology
Laboratory of Electromechanics
P.O.Box 3000
FIN-02015 HUT
Finland

Dissertation for the degree of Doctor of Technology to be presented with due permission for public examination and debate in Auditorium S4 at Helsinki University of Technology, Espoo, Finland, on the 5th of February, 1999, at 12 o'clock noon.

ESPOO 1999

Lantto E. **Robust Control of Magnetic Bearings in Subcritical Machines**. Acta Polytechnica Scandinavica, Electrical Engineering Series No. 94, Espoo 1999, 143 p. Published by the Finnish Academy of Technology. ISBN 952-5148-80-7. ISSN 0001-6845.

Keywords: Active magnetic bearings, robust control, unbalance compensation, generalized Nyquist diagram, Numerical range

ABSTRACT

This publication deals with the robust control of active magnetic bearings (AMB). Methods are developed for the control system synthesis and analysis for subcritical machines.

A new synthesis method is developed for the position control loop. In the method, linearization is achieved using two rotation matrices, and two controllers are designed using SISO (single-input, single-output) methods. The controller structure is based on the H_∞-optimal controller, which is the best solution with respect to the stated physical performance limits. A generalized Nyquist diagram, based on the numerical range, is used to analyze the system. This diagram gives highly nonconservative stability robustness estimates and is mathematically elegant. The effect of the most important nonlinearity, i.e. power amplifier saturation, is carefully analyzed.

For unbalance compensation a simple algorithm is proposed which has only one tuning parameter. By using the generalized Nyquist diagram, it is shown that this simple algorithm generally works in the case of subcritical machines, also at the rigid-body resonance speeds. The single feedback coefficient and robustness can be easily determined using the generalized Nyquist diagram. Finally, AMB is used in mechanical balancing of an elastic rotor.

PREFACE

This work was carried out during the years 1993-1998 as a part of the research project "Development of high-speed electric motors" in the Laboratory of Electromechanics, Helsinki University of Technology. The project was financed by the Technology Development Centre Finland (TEKES) and High Speed Tech Oy Ltd.

I would like to express my gratitude to Professor Tapani Jokinen, Head of the Laboratory of Electromechanics, for excellent working facilities. I also want to thank the laboratory members for helpful discussions and an enjoyable atmosphere to work in. Professor Koivo and other members of the Control Engineering Laboratory deserve thanks for their advice and critical comments. Special thanks goes to the AMB team, Dr. Matti Antila, Mr. Ville Tommila, Mr. Marko Palko, Lic.Tech. Olli Lindgren and Mr. Seppo Lappalainen. During last five years, this team has been solving the problems of this technology without prejudice, showing creativity and great skills. High Speed Tech Oy Ltd. deserves thanks for supplying the problems to be solved and the corresponding test machines. Most of all, I am obliged to my wife Tarja for her understanding and continuous support.

Financial support by the Tekniikan Edistämissäätiö and Emil Aaltosen Säätiö are gratefully acknowledged.

Espoo, December 1998

Erkki Lantto

CONTENTS

LIST OF SYMBOLS

a_{rel}	amplifier saturation level
$\boldsymbol{B}_b$	transformation matrix from bearing forces to generalized forces
c	position stiffness
C,$\boldsymbol{C}$	position controller
C_{opt},$\boldsymbol{C}_{opt}$	solution to H_∞-optimization problem
co()	convex hull
$\boldsymbol{C}_S$	transformation matrix from generalized coordinates to position measurements
$\boldsymbol{D}_{rot}$	rotordynamic damping matrix
F, $\boldsymbol{F}$	force in general, scalar and vector
F_{max}	static load capacity
F_b, $\boldsymbol{F}_b$	bearing force, total
F_{bcur}, $\boldsymbol{F}_{bcur}$	bearing force, controlled part
F_{bpos}, $\boldsymbol{F}_{bpos}$	bearing force, position stiffness part
$F_l(\boldsymbol{P},\boldsymbol{C})$	lower linear fractional transformation with parameters $\boldsymbol{P}$ and $\boldsymbol{C}$
$\boldsymbol{F}_{qX}$, $\boldsymbol{F}_{qY}$	generalized external forces
g	high amplitude actuator response
G_b, $\boldsymbol{G}_b$	bearing model
G_{flim}	transfer function which approximates the dynamic force limit
$\boldsymbol{G}_{rot}$	rotordynamic gyroscopic matrix
h_f	current stiffness
h_v	motion voltage coefficient
i_{bias}	bias current
i_c, $\boldsymbol{i}_c$	control current
i_{cref}, $\boldsymbol{i}_{cref}$	control current reference
i_{fmax}	the coil current when the bearing force is F_{max} at nominal conditions
i_{max}	current limit in the power amplifier
$\mathbf{I}$	unit matrix
j	imaginary unit
k_{cf}	current feedback coefficient
k_{dynf}	dynamic force correction factor
$\boldsymbol{K}_{in}$	uncertain gain matrix at the plant input
$\boldsymbol{K}_{out}$	uncertain gain matrix at the plant output
$\boldsymbol{K}_{rot}$	rotordynamic stiffness matrix
$\boldsymbol{K}_{unb}$, k_{unb}	unbalance compensator feedback matrix and scalar
L_{dyn}	dynamic inductance
$\boldsymbol{L}$	open loop transfer function matrix
$\boldsymbol{L}_F$,$\boldsymbol{L}_p$	open loop transfer function matrix at the bearing force and displacement
$\boldsymbol{M}_{rot}$	rotordynamic mass matrix
$\boldsymbol{P}$	augmented plant in H_∞-optimization
p_b,$\boldsymbol{p}_b$	rotor positions in the magnet locations
p_{max}	maximum allowed vibration amplitude
p_S,$\boldsymbol{p}_S$	rotor positions in the sensor locations
p_{weight}	position weight in H_∞-optimization
$\boldsymbol{q}_X$, $\boldsymbol{q}_Y$, $\boldsymbol{q}_C$	generalized rotor coordinates: XZ plane, YZ plane and complex
r	load resistance

R,$\boldsymbol{R}$	rotor model
$\mathbf{R}_{R1}$,$\mathbf{R}_{R2}$	rotation matrices in the proposed controller structure
s	Laplace variable
S,$\boldsymbol{S}$	sensitivity function $(\mathbf{I}+\boldsymbol{L})^{-1}$
T,$\boldsymbol{T}$	complementary sensitivity function $\boldsymbol{L}(\mathbf{I}+\boldsymbol{L})^{-1}$
U	unbalance
U_{bp}	unbalances reduced into balancing planes
U_n	nth modal unbalance
$\boldsymbol{U}_{X,Y,C}$	unbalance vector, X direction, Y direction and complex
v	bending mode influence factor
$\boldsymbol{v}$	eigenvector
V	voltage
V_c	control voltage
V_{max}	amplifier maximum voltage
W	weight in H_∞-optimization
α_{pulse}	direction of the pulse sensor
β	rotation angle
δ	air gap
Δ	deviation from the equilibrium
$\phi(\boldsymbol{K})$	uncertainty region of $\boldsymbol{K}$
$\varphi(\boldsymbol{L})$	numerical range of matrix $\boldsymbol{L}$
$\varphi_S(\boldsymbol{L})$	structured numerical range of matrix $\boldsymbol{L}$
λ	eigenvalue
μ	structured singular value
$\rho(\boldsymbol{L})$	set of eigenvalues of $\boldsymbol{L}$
$\overline{\sigma}$	largest singular value
$\underline{\sigma}$	smallest singular value
ω_{fmax}	force bandwidth
ω_{pos}	position bandwidth
Ω	rotational speed
Ω_{crfn}	bending critical speeds of the unsupported rotor
$\|\boldsymbol{X}\|_2$	vector 2-norm or induced 2-norm of the matrix $\boldsymbol{X}$
$\|\boldsymbol{X}\|_\infty$	vector ∞-norm or induced ∞-norm of the matrix $\boldsymbol{X}$
$\|\boldsymbol{G}(s)\|_\infty$	system infinity norm; $\|\boldsymbol{G}(s)\|_\infty = \sup_\omega \overline{\sigma}\left[\boldsymbol{G}(j\omega)\right]$

Subscripts

C	complex coordinates
X	X-coordinate axis
Y	Y-coordinate axis
0	nominal value
rot	rotordynamic matrix

Superscripts

H	complex conjugate transpose
T	transpose
‘	coordinates in a rotating reference frame
*	complex conjugate

Abbreviations

AMB	Active magnetic bearing
FEM	Finite element method
Im	Imaginary part
MIMO	Multi-input, multi-output
Re	Real part
SISO	Single-input, single-output

1 INTRODUCTION

1.1 A short introduction to AMB

In this section a short introduction to active magnetic bearings (AMB) and its basic properties is given. More thorough treatment is found in the book of Schweitzer *et al*. (1994) and tutorial papers written by several authors: Haberman and Brunet (1986), Lantto and Antila (1995), Schweitzer (1990) and Zhuravlyov (1992).

The field of electromagnetic levitation applications is wide and there are a number of possible physical principles (Bleurer 1992). In magnetic bearings the most important and technically mature operating principle is magnetic attraction between ferromagnetic bodies. With this approach, reasonably high forces can be generated with conventional magnetic materials used in electric motors. Unfortunately, this type of suspension has a well-known unstable nature (Earnshaw 1842). This can be easily demonstrated by trying to levitate a piece of iron using permanent magnets.

Despite this unstable nature, it is possible to achieve passive levitation in some degrees of freedom. Some degrees of freedom must be actively controlled, i.e. the electromagnet currents are controlled by electronics so that stable suspension is obtained. Although there are lots of applications with combinations of passive and active magnetic bearings, active control has certain benefits that make it very attractive, especially for bigger machines. The most common types of radial and axial bearing geometry are shown in Figure 1.

The radial bearing comprises four electromagnets producing attractive forces on the rotor in four directions. The rotor has a laminated surface to decrease eddy currents caused by rotation. Also, the stator is usually made of steel sheets for manufacturing reasons and to decrease the eddy currents when the flux is rapidly changing. With conventional electric sheet steels a force of about 30 N/cm^2 can be achieved from a bearing cross-section (*LD* in Figure 1). With more expensive cobalt-based materials the achieved force is about double. The rotor lamination is a critical part with respect to material strength. This subject is discussed in detail by Larsonneur (1990).

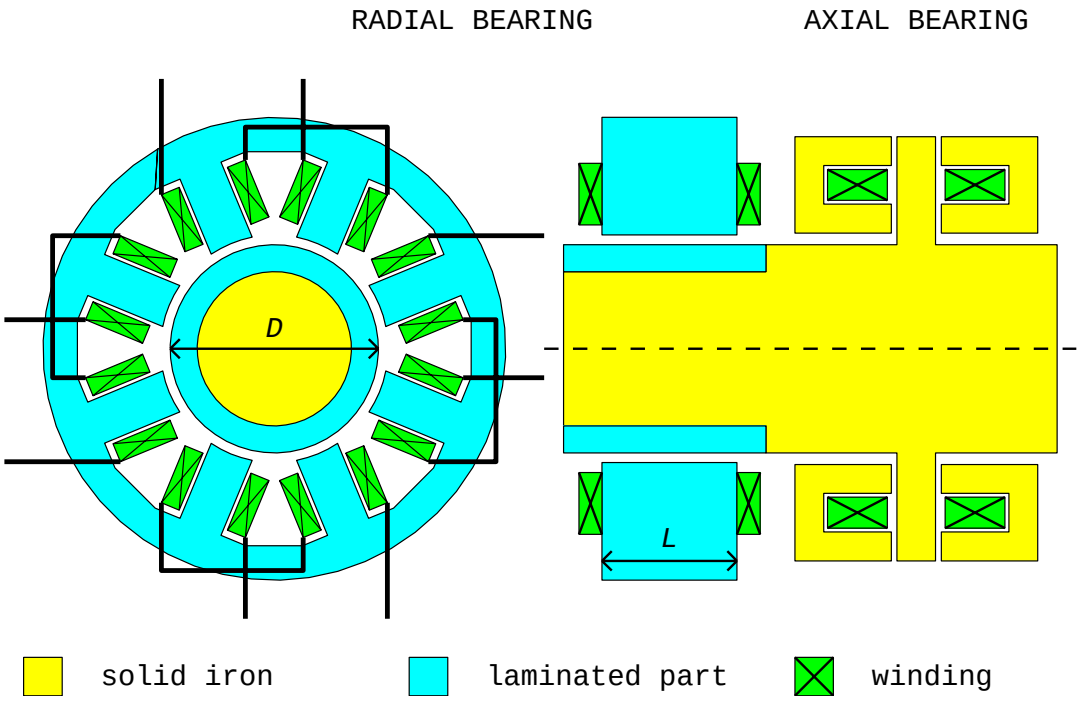

Figure 1. Radial eight-pole magnetic bearing and axial disc-type bearing.

The axial bearing consists of axially symmetric electromagnets in the stator and a disc in the rotor. Because of high centrifugal stress, the rotor part is usually solid. Often, the stator is also made of solid iron. Because of the axial symmetry, there are no eddy currents caused by rotation. However, the axial bearing suffers from the eddy currents caused by flux changes. This means power consumption in the dynamic situation and phase lag between bearing current and bearing force, which slightly complicates the control of the axial bearing.

AMB allows high rotational speeds. Surface speeds of over 200 m/s can be obtained with radial AMB. At a high speed, the friction losses remain low. In high-speed machines the air friction is typically many times higher than the friction caused by iron losses in AMB. For example, in the test machine (Appendix C) the friction caused by the bearing iron losses is 600 W at the maximum speed 540 Hz, while the air friction is several kilowatts.

An AMB system usually controls five degrees of freedom, four radial and one axial. In Figure 2 the most common control system for one degree of freedom is shown. There are also other possible control concepts like flux control, voltage control, position sensorless bearing, etc. These are compared by Buhler *et al*. (1996).

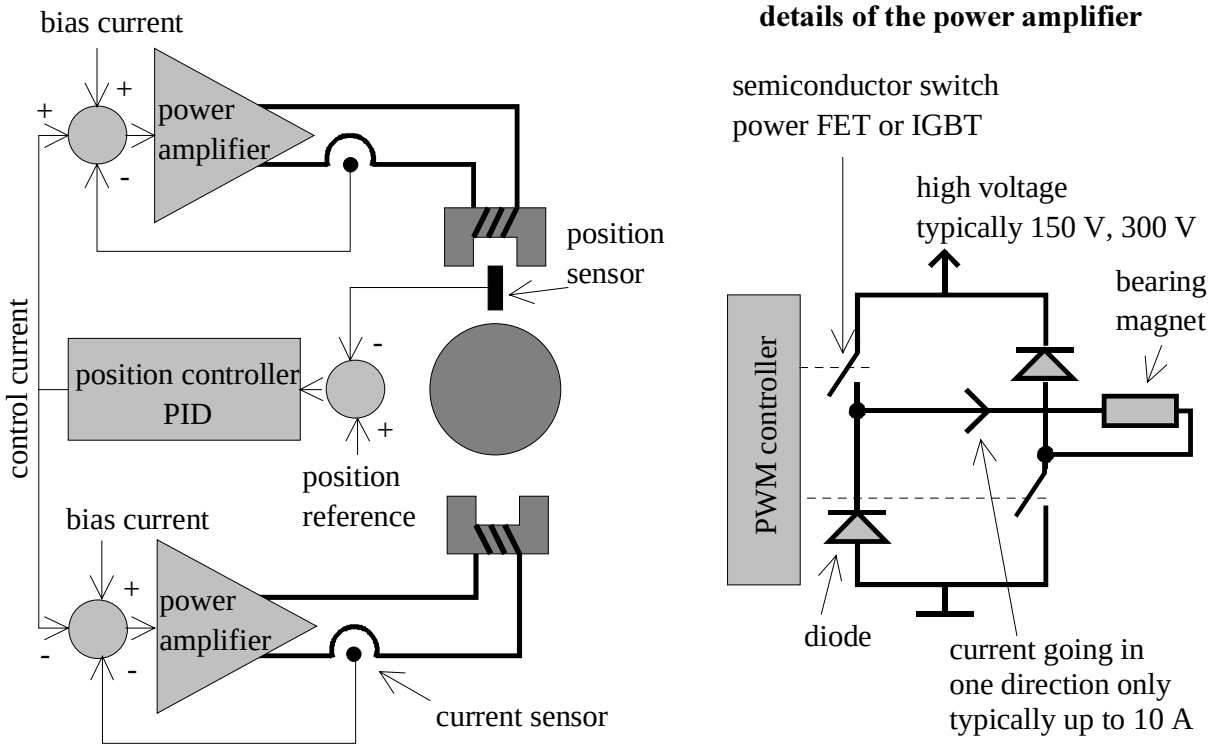

Figure 2. One degree of freedom control system and the half bridge power amplifier.

The electromagnets on opposite sides of the rotor are controlled by the same position controller. The position information is obtained from a position sensor. It is typically an inductive or an eddy-current type sensor but other possibilities exist as well (Boehm 1993). A biasing current is fed into the electromagnets. The position controller computes a control current that is added to one magnet and subtracted from the opposite magnet. Consequently, the attractive force is increased in one magnet and decreased in the opposite magnet. At low flux densities the attractive force is proportional to the square of the current. This nonlinear relationship is effectively linearized by the bias current.

The position controller is basically of the PID-type. As the rotor is moved upwards, the output of the P-term decreases the current in the upper coil and increases in the lower coil. Consequently, a downward force is produced. Therefore, the P-term is acting as a spring. The D-term reacts to the velocity, which produces damping. The integrator is included to clear the static position error. The position of levitation can be adjusted inside the air gap by tuning the position reference.

The right-hand side of Figure 2 shows a typical power amplifier used in AMBs. The half bridge is capable of driving current in one direction only. This is sufficient because the force is independent of the current direction. An important feature of the half bridge amplifier is

that the current can be increased and decreased equally fast. The semiconductor switches change states at high frequency, which is typically of the order of 40 kHz. Accordingly, pulse-width modulated output voltage is generated. Even though a couple of volts is enough to run the steady state currents in the magnets, high voltage is necessary to achieve a sufficiently high current (force) slew rate. With weak power amplifiers, levitation becomes difficult to achieve. The necessary incidental power increases as the size of the levitated rotor increases. An amplifier with a maximum voltage of 150 V and a maximum current of 10 A is sufficient for a subcritical rotor weighing 100 kg.

Retainer bearings, also called emergency bearings, auxiliary bearings and touch-down bearings, are a critical part of the AMB system. These are roller or other types of bearings with a smaller air gap than the electromagnets and the sensors. When the electromagnets are de-energized, the rotor lies on these bearings. The most important function of the retainer bearings is to allow a safe rundown in the case of failure.

Most machines will experience power breakdowns every now and then. To build retainer bearings that last a sufficient number of rundowns from maximum speed is not always possible or reasonable. Then, some kind of uninterruptable power supply is needed. In the case of inverter-fed motors, the uninterruptable power supply can be arranged by turning the motor into a generator in the case of a power breakdown. This kind of power supply uses the kinetic energy of the rotor and fails only after the rotation has stopped.

1.2 AMB applications

In this section, a short review of the applications and benefits of AMB technology is given; see also Dussaux (1990) and Schweitzer *et al*. (1994). As far as the author knows, the first active magnetic suspension system was made by Beams *et al.* (1946). He levitated small steel balls in a vacuum and rotated them hundreds of thousands of revolutions per second to achieve high centrifugal stress. Magnetic bearings are capable of operating in a vacuum, their friction losses are very small and they need practically no maintenance. These properties make them suitable for flywheel energy storage systems, spacecraft attitude control devices and related applications (Nakajima 1988, Kirk *et al*. 1994, Studer 1978, Bichler 1990). In these applications the vibration-free operation is also considered an important feature. With

unbalance compensation, it is possible to eliminate the rotation synchronous bearing force so that the unbalance force is not transmitted to the machine stator and surrounding structures.

A big application area for AMB technology is that of heavy compressors and turbines (Schmied 1990, Canders *et al*. 1994, Moulton and Eakins 1992). In these applications the biggest benefits of AMB are considered to be oil-free operation (to avoid fire hazards and contamination), better rotordynamic control and low maintenance. The inherent condition monitoring in AMB is also a considerable advantage. Rotor unbalance vibrations and compressor forces can be monitored by AMB without additional instrumentation. This information can be used to ensure safe operation and to estimate the need for maintenance.

In high-speed machining, AMB allows high rotational speed and high power due to its high surface speed (Siegwart *et al*. 1990, Brunet and Wagner 1994). In these applications AMB offers also some unique advantages. For example, the cutting force can be controlled based on the AMB currents. AMB has also been used in many other applications like centrifuges (Konuma *et al*. 1994), turbomolecular pumps (Mazzocchetti *et al*. 1994) and vibration dampers for large turbogenerators (Chan 1990). Considerable development work has been done to apply AMB to aircraft gas turbine engines (Meeks *et al*. 1994) and rocket engine turbopumps (Girault 1988).

In Finland the AMB research started in 1985. At the beginning, the goal was to develop an axial magnetic bearing to be used with radial gas dynamic bearings in a high-speed turbogenerator. Later, a radial AMB system was also developed. During recent years, several sizes of one-stage turbocompressors with five-axis AMB have been developed to a commercial level (Lindgren *et al.* 1995, Antila *et al*. 1996, Lantto *et al*. 1997). In Figure 3, a schematic diagram of such a compressor is shown.

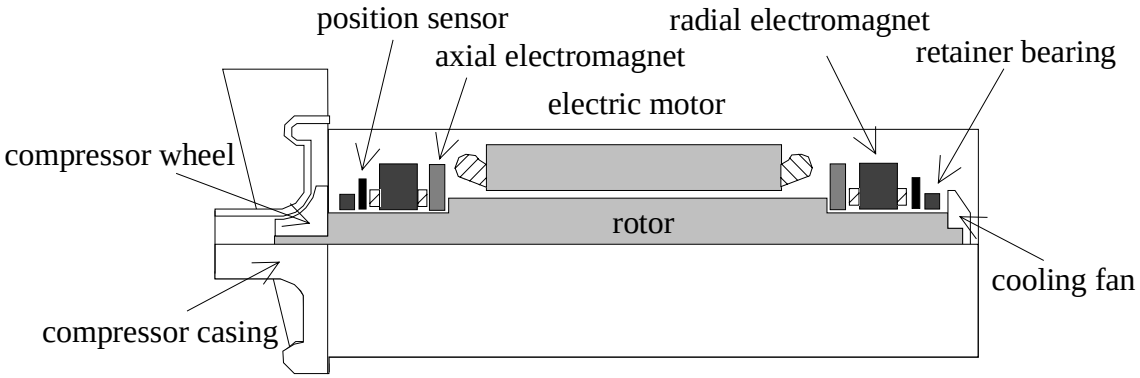

Figure 3. Schematic diagram of a high-speed turbocompressor.

As can be seen, the construction is very compact and simple, with only one moving part. In Figure 4, six 250 kW turbocompressors are shown running in a water treatment plant.

Figure 4. Six 250 kW, 32000 1/min. turbocompressors running in a water treatment plant in Finland. At the right-hand side the frequency converter and the AMB control electronics.

In these high-speed applications AMB becomes necessary to achieve a long lifetime. Oil-free operation is also an important advantage, especially in the water treatment compressors.

A properly designed AMB system is close to the ideal bearing with many superior features, and it has already proven its feasibility in demanding applications. The AMB is, however, a relatively complicated system. Expertise in the fields of mechanics, magnetic fields, electronics and control engineering is needed to build a well-operating AMB system.

Neglecting or misunderstanding the properties and limitations of AMB leads to problems. The most typical pitfalls are discussed by Penfield *et al*. (1995). Today, however, the problems are successfully solved or avoided in hundreds of different applications.

1.3 Contents and purpose of the work

The purpose of the present work is to find methods to build robust and effective AMB control systems and to clarify the physical relationships between different aspects.

Chapter 2 is a short description of the AMB dynamics. In Section 2.1 the linearized actuator model is given. The main emphasis is on the variations of the parameters of the linearized model. In Section 2.2 the effect of amplifier saturation is discussed. The dynamic force limit is

given and the response to high-amplitude reference signals is simulated using a nonlinear bearing model. In Section 2.3 the rotor model is briefly described. Also, the bearing force needed to pass bending critical speeds is studied in order to explain why subcritical operation is preferred in the high-speed machines. In Section 2.4 the disturbance forces are discussed.

In Chapter 3, the position control system is synthesized and analyzed. Section 3.1 is a short literature review. In Section 3.2, suspension of a point mass is first discussed. The physical performance limits are stated and a controller that approaches this limit is synthesized using H_∞-optimization. It is shown that the physical performance limits cannot be obtained at all frequencies, but a compromise should be made. Then, the stabilization of the bending modes is discussed and five different strategies are compared.

In Section 3.3 the uncertainty model of the AMB system is given. A short literature review is done of the methods for analyzing these kinds of systems. Then, the generalized Nyquist diagram, used in this publication, is described. In Section 3.4 the MIMO case is considered. First, it is shown that the decentralized control strategy leads to problems. Then, the physical performance limits are sought using H_∞-optimization. The structure of the optimal controller is found and, based on this observation, a synthesis method is proposed for subcritical, slightly gyroscopic machines. This method is applied to the test machine and the generalized Nyquist diagram is used to analyze the design. In Section 3.5 the design is experimentally tested. The stability borders are calculated and impulse responses are measured. Then, the stability at large signal amplitudes is studied both theoretically and experimentally. Also, the effect of amplifier saturation due to high frequency disturbance is analyzed.

Chapter 4 is devoted to the analysis of the unbalance problem. In Section 4.1 a literature review is presented. In Section 4.2 the mathematical formulation for synchronous signal treatment is given and the effect of different compensation strategies is shown. In Section 4.3 a simple compensation algorithm is proposed and analyzed using the generalized Nyquist diagram. It is shown that the proposed algorithm generally works very well in the case of subcritical AMBs. In Section 4.4 AMB is used in mechanical balancing.

The details and the proofs considering the generalized Nyquist diagram are collected in Appendix A. In Appendix B, the relationships between amplitude and phase curve of a stable minimum-phase system are given. In Appendix C, the details of the test machine are listed.

1.4 The scientific contribution of this work

The biggest scientific contributions of this work are listed below.

1. Extensive use of the numerical range in robustness analysis of a practical process.
2. The synthesis method for the AMB position control loop.
3. Strong results in the field of unbalance compensation.

The numerical range has been proposed as a tool for robustness analysis in the 1980's. In the present publication the power of this approach is shown in the analysis of AMB process. It is used both in the analysis of the position control loop and the unbalance compensation algorithm. The generalized Nyquist diagram, based on the numerical range, is also shown to have certain relationships with the closed-loop singular values. Therefore, it is a useful tool in analyzing performance as well.

The controller synthesis method is straightforward and leads to a controller structure with input and output rotation matrices and a diagonal controller between these. The open loop becomes normal at the plant input and output. A controller structure in which the translatory and conical modes are separately controlled is not a new idea. However, this kind of a controller is a special case of the proposed more general controller structure. Also, a normalizing controller is an old idea in classical multivariable feedback theory. In this publication, however, the controller structure is obtained by searching the physical performance limits and the normality is a consequence of this reasoning. Furthermore, the new way of estimating stability under high-amplitude disturbances and the stability threshold in the case of amplifier saturation, in Section 3.5, proved to be useful.

The proposed simple compensation algorithm is not new. However, with the analysis based on the generalized Nyquist diagram the author has been able to show that this algorithm generally works in the case of subcritical high speed machines also at the rigid-body resonance speeds. The feedback coefficient and the robustness of the algorithm can be easily determined by inspection of the generalized Nyquist diagram.

2 MODELING THE AMB SYSTEM

2.1 The linearized actuator model

In this section, a current-controlled radial 8-pole actuator is discussed. The actuator consists of the electromagnets and the amplifier with current-control loop and bias-current linearization.

Magnetic force is proportional to flux density squared, and the flux density is linearly related to bearing current at low flux densities. As seen in Figure 1, the magnetic circuit is simple. Consequently, simple analytic expressions can be drawn for the linearized model parameters (Schweitzer *et al.* 1994, Lantto and Antila 1995, Zhuravlyov 1992). Unfortunately, many critical aspects are not taken into consideration by these expressions. For engineering purposes, a reluctance network is usually a good enough model. Its accuracy is good when the magnetic circuit is not too heavily saturated. The predictions become increasingly optimistic, however, as the magnetic circuit gets saturated. The flux fringing in particular is not modeled by the reluctance network. If very accurate and reliable results are needed then the finite element method (FEM) should be used (Antila *et al*. 1998). The magnetic circuit analysis described in this section is done using FEM and the calculations were performed by Matti Antila. The bearing geometry is given in Appendix C.

In a current-controlled radial bearing, the position controller computes reference current i_{cref} for every four channels: 1-end X, 2-end X, 1-end Y and 2-end Y. The coordinate system is chosen so that the Z axis is aligned with the rotor. The magnets in the positive direction of the coordinate axes are called UP-magnets and the ones in the negative direction DOWN-magnets. The power amplifier tries to keep the current in the UP-magnet at the value $i_{bias}+i_{cref}$ and the current in the DOWN-magnet at the value $i_{bias}-i_{cref}$. Due to the amplifier structure, the coil current is limited downwards to zero and upwards to i_{max} to protect the amplifier against overheating, see Figure 5. The bias current i_{bias} is a traditional way to linearize the nonlinear current-force relationship. As a consequence, the bearing force depends very linearly on the control current. For the test machine, i_{max}=10 A and i_{bias}= 2.75 A. In Figure 5 the computed and measured force curves are shown.

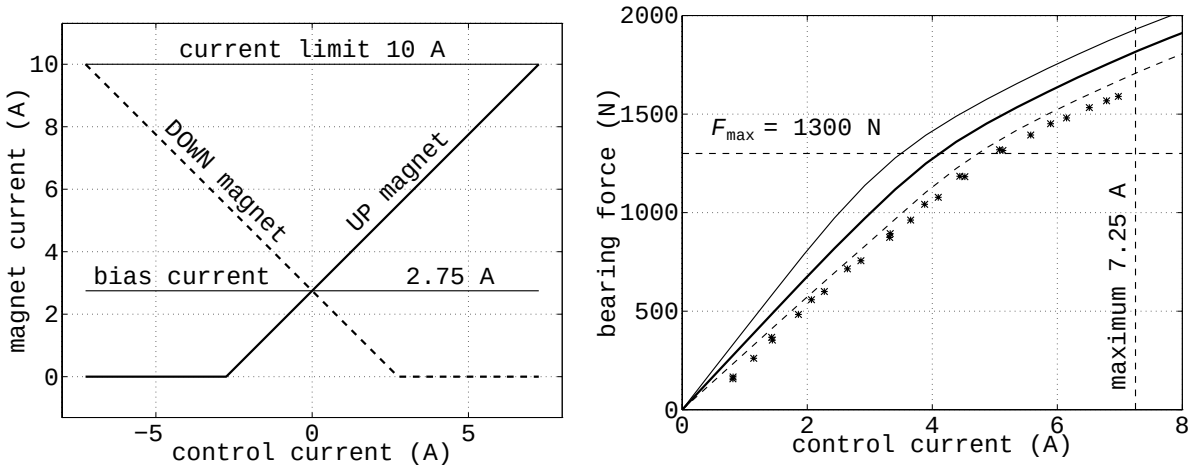

Figure 5. The control of the one coordinate axis on the left-hand side. The bearing force as a function of the control current on the right-hand side. The curves are computed for three different air gaps: 0.55 mm (bold line), 0.5 mm (thin solid line) and 0.6 mm (thin dotted line). The measured points are labeled with asterisks (*).

In Figure 5 the bearing force is drawn as a function of the control current for three different air gaps: with a nominal value of 0.55 mm, with a small one of 0.5 mm and with a large air gap of 0.6 mm. The variation is due to manufacturing tolerances and thermal expansions.

The static load capacity $F_{\max}$ is the load under which the bearing is able to lift the rotor up to levitation from the retainer bearings, whose air gap is 0.25 mm. The static load capacity was determined experimentally. Note that the load capacity is defined in the weakest direction, which is the direction of an electromagnet. In between the magnets, the achieved force is higher. The reason for such a conservative definition for $F_{\max}$ is that, in practice, the rotor may contact the retainer bearing because of some short-term transient. After the transient has gone, the bearings should be able to lift the rotor back to levitation. For traditional silicon steel laminates the static load capacity can be approximated as

$$F_{\max} \approx LD * 20 \frac{N}{cm^2}, \tag{1}$$

where L and D are the stator packet length and rotor diameter shown in Figure 1.

When the bias current i_{bias} is properly chosen, the relationship between control current and bearing force is smooth (Figure 5). This suggests that a linear model is valid in a large neighborhood of an equilibrium point.

This linearized actuator model reads

$$
\begin{aligned}
& L_{\mathrm{dyn}} \frac{d\Delta i_{\mathrm{c}}}{dt} + \left(h_{\mathrm{v}} \frac{dp_{\mathrm{b}}}{dt} + r\Delta i_{\mathrm{c}} \right) = \Delta V_{\mathrm{c}} \\
& \Delta F_{\mathrm{b}} = F_{\mathrm{bpos}} + F_{\mathrm{bcur}} = c\Delta p_{\mathrm{b}} + h_{\mathrm{f}} \Delta i_{\mathrm{c}} \,, \\
& V_{\mathrm{c}} = k_{\mathrm{cf}} \left(i_{\mathrm{cref}} - i_{\mathrm{c}} \right),
\end{aligned}
\tag{2}
$$

where L_{dyn} is the dynamic inductance,
i_{c} is the control current,
h_{v} is the motion voltage coefficient,
p_{b} is the rotor position in the bearing location,
r is the load resistance (coils, cables and amplifier),
V_{c} is control voltage,
F_{b} is total bearing force,
F_{bpos} is the position stiffness force,
F_{bcur} is the controlled bearing force,
c is position stiffness,
h_{f} is current stiffness,
k_{cf} is the current feedback coefficient and
Δ means deviation from the equilibrium point.

Note that the UP and DOWN coils are separately controlled, as shown in Figures 5 and 8. Therefore, the control current i_{c} and control voltage V_{c} are only fictitious quantities, not actually existing in the plant. However, in the linearized model, it is more convenient to replace the two coil currents and voltages by one control current and control voltage. As the coil currents are assumed to follow the curves shown on the left-hand side of Figure 5, the control current i_{c} is well defined. The control voltage V_{c} is defined as the coil voltage of the more loaded electromagnet with proper sign convention, i.e. if the DOWN-magnet is more loaded, the control voltage is the DOWN-side coil voltage multiplied by -1. By this definition, the dynamic inductance is computed for the more loaded electromagnet.

The load resistance is usually of the order of one ohm and its effect on the current-controlled bearing is negligible. So is the effect of the motion voltage term. When the control current in a channel is near zero, then $h_{\mathrm{v}}=h_{\mathrm{f}}/2$ in this channel, and when the current is going only in one magnet (UP or DOWN) then $h_{\mathrm{v}}=h_{\mathrm{f}}$. The motion voltage term diminishes the destabilizing effect of the position stiffness. Thus, it is safe to ignore it. An advantage of dropping the motion voltage term is that the system model is simplified considerably. These coil resistance

and the motion voltage terms are taken into consideration only in Section 4.2 in the analysis of unbalance compensation strategies.

The parameters of the linearized bearing model depend considerably on the air gap, bias-current, static load and eccentricity (the rotor center is deviated from the bearing magnet center). The variation of the parameters is shown in Figure 6. The curves are computed up to a load of 2000 N, but 1600 N is considered to be the maximum load where the control system should “handle” the suspension. To “handle” does not merely mean that the suspension is stable but that it should be possible to run the machine without problems. Note that the changes are not computed with respect to bias current, because it can be assumed accurate. Also, the parameters are not computed for different eccentricities, because practical experience has shown that this machine construction has negligible eccentricity. The variation of the linearized model parameters is studied in more detail by Antila (1998).

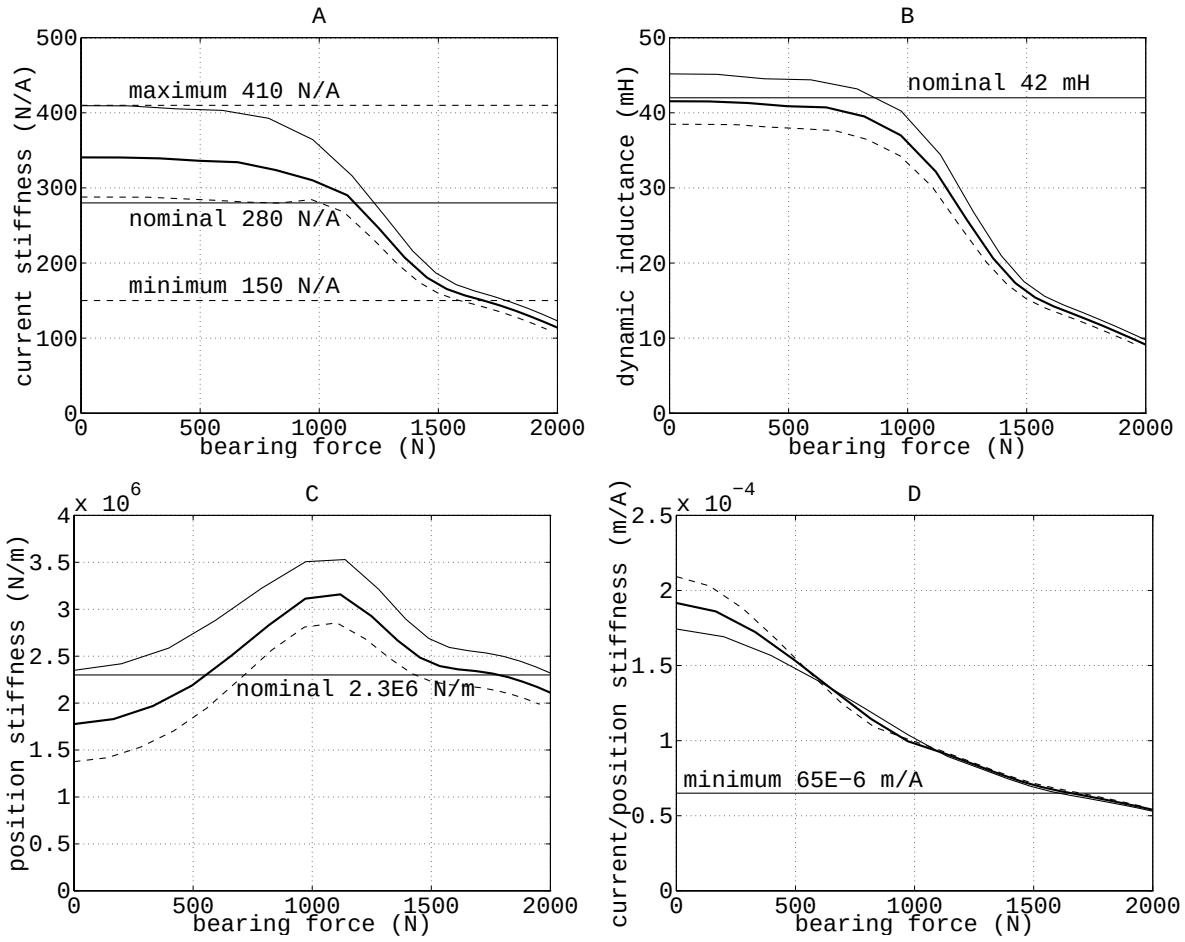

Figure 6. The variation of the parameters of the linearized bearing model as a function of the bearing force. The curves are computed at the center position for three different air gaps: 0.55 mm (bold line), 0.5 mm (thin line) and 0.6 mm (thin dashed line).

It turns out that the most severe parameter variation is the change of the current stiffness. As the load increases, current stiffness drops. When it has dropped enough, instability occurs. Instability also occurs if the current stiffness becomes too high. Let us choose the nominal value as the arithmetic mean of the maximum and minimum, which is h_{f0}=280 N/A. The true current stiffness may deviate from the nominal value by 50 %.

Even though the current stiffness is assumed to be real valued, there is small phase lag between the control current and controlled bearing force. This phase lag is caused by eddy currents and hysteresis in the magnetic circuit. These phenomena also have a small effect in the case of a laminated magnetic circuit and, according to accurate measurements, the phase lag is of the order of 5° (Antila 1998). Further, in the nominal actuator model the X and Y directions are assumed disconnected. In reality, there are cross-connections, especially in the highly loaded conditions. This means that a control current change in the X direction also causes a force change in the Y direction and vice versa. It turns out that the NSNS-pole configuration has very small cross-connections and they need no special treatment in the control system synthesis (Antila 1998). The phase lag and cross-connections are not taken into consideration in the bearing model, but they are kept in mind. Fortunately, the analysis method introduced in Section 3.3, also provides the robustness information with respect to these unidealities.

Let us next consider the effect of the variation of the dynamic inductance. The current is controlled by a P-controller: $V_c = k_{cf}\left(i_{cref} - i_c\right)$, where k_{cf} is the current feedback coefficient. Because of the current measurement noise, a finite value for k_{cf} is used. However, the bandwidth of the current feedback loop is set clearly higher than the unity gain frequency of the position control loop, and therefore even high variations of the dynamic inductance have no significant effect on the suspension dynamics. Because it is safer to drop the dynamic inductance than to increase it, a relatively high value for the dynamic inductance is chosen as a nominal value. The inductance at low load and nominal air gap, L_{dyn0}=42 mH, is a good one. The variation of the dynamic inductance is not considered directly in the analysis. However, this effect is also kept in mind because the decrease in the dynamic inductance introduces a small phase advance at high frequencies and an increase in the dynamic inductance means a phase drop.

The position stiffness has a destabilizing effect. Even though the variation range is quite large, no uncertainty is assumed for the position stiffness. This is because the position

stiffness has the greatest effect at low frequencies, and there the stability threshold is not determined directly by the position stiffness but by the ratio between current stiffness and position stiffness. Considering stability, the most serious situation is when this ratio is the minimum. Let us choose the nominal position stiffness so that when the current stiffness is at its lower limit (at 1600 N load) then the ratio between the true current stiffness and nominal position stiffness is exactly the minimum shown in Figure 6D. This leads to c_0=150 N/A / 65*10^{-6} m/A = 2.3*10^6 N/m. This choice should lead to accurate stability margin predictions.

According to the previous discussions, a simplified linear actuator model which still preserves the essential dynamics can be written

$$F_{\mathrm{bcur}} = G_{\mathrm{b}}(s)\Delta i_{\mathrm{cref}}\,,\; G_{\mathrm{b}}(s) = \frac{h_{\mathrm{f0}}k_{\mathrm{cf}}}{L_{\mathrm{dyn0}}s + k_{\mathrm{cf}}}, \tag{3}$$

where G_{b} is the nominal bearing model transfer function. The position stiffness effect is embedded into the rotor model, as shown in Section 2.3.

How to improve the force response

In this publication, only the traditional current-controlled magnetic actuator is considered. As can be seen, the problems with this approach are a high destabilizing spring effect and large parameter variations due to manufacturing tolerances and operational point changes. The problems arise because we need to control the bearing force and the bearing current is not very well correlated with the force. In the high-speed machines considered in this publication, sufficiently good bearing properties can be obtained with this actuator. However, it is obvious that the variations are too large for certain applications and the force response should be improved somehow.

The bearing force is related directly to the square of the air gap flux density. If the flux density were known, it could be used as a feedback variable. This would lead to very small uncertainty in the actuator and negligible destabilizing effects. We could control the force directly. A big disadvantage of this approach is that new instrumentation is needed.

Even if the air gap flux density is not directly measured, its time derivative can be measured with a simple coil (Brunet 1988). The time derivative can also be approximated from the

control voltage with no new instrumentation. This time derivative signal, with or without a flux detecting coil, can be used to create a flux estimate, which may be used in the control (Hara *et al*. 1996). Using this kind of flux feedback scheme, the above-mentioned unwanted effects can be reduced.

The range of parameter variations can be reduced also by compensating the nonlinearity, shown in Figure 5, with a nonlinearity in the controller. A simple gain scheduling, where a higher gain is used in a highly loaded channel, compensates effectively the drop of the current stiffness.

Suggestions for the actuator design

In AMB, the electromagnet's air gap is an important design parameter. From the electromagnetic point of view it should be as small as possible. The needed power amplifier capacity (V_{max}*i_{max}) in particular increases relative to the air gap. Also, the magnetizing current and consequently the resistive losses increase as air gap increases. There are, however, many reasons why the air gap cannot be made arbitrarily small. First, the retainer bearings should have a smaller air gap than the electromagnets and there should be enough margin that in the worst case the rotor does not contact the electromagnets when it is running on the retainer bearings. Secondly, the relative air gap variations due to thermal effects, manufacturing tolerances and centrifugal enlargements should not be too large. Otherwise, individual tuning becomes necessary or a more complicated control system must be employed.

A second interesting detail is the bias current. The purpose of the bias current is to linearize the actuator behavior. Whether or not the actuator is linear can be checked by drawing the bearing force as a function of the control current, as shown in Figure 5. At a very high load the current stiffness drops to a small value that is independent of the bias current. Choosing too high a bias current raises the current stiffness at zero load to a very high value. Consequently, it will be difficult to achieve a controller that operates well over all the loads. Further, high bias current leads to high resistive losses in the bearings and amplifiers and to high friction losses. The choice of the bias current is considered in more detail by Antila (1998).

A third important detail is the current feedback coefficient k_{cf}. A high value leads to noisy bearings due to current measurement noise. A low value causes a phase lag which must be

compensated with a phase lead in the position controller. In between the values which are too low and too high the choice of the current feedback coefficient is not too critical.

2.2 Effects of amplifier saturation

In this section the consequences of control voltage limitations is discussed. First, the dynamic force limitation is studied. Then, the effect of current and voltage limits to the high amplitude response is simulated. Finally, the effect of the control voltage saturation due to high-frequency disturbance is studied.

Dynamic load capacity

The bearing force is proportional to the magnetic field energy in the air gap. To change the force, the energy has to be transferred into the magnetic circuit or out of it. The rate of the energy change is limited by the power amplifier maximum voltage $V_{\max}$ (150 V in the test machine). Therefore, the force $F_{\max}$ can be obtained only up to a certain frequency ω_{fmax} and at higher frequencies the achieved bearing force decreases as $1/\omega$. Dynamic force limits are studied in detail by several authors; see especially Bornstein (1991) and Maslen *et al*. (1989).

The frequency ω_{fmax} is called the force bandwidth. It is defined as follows. Let i_{fmax} be the current in the loaded electromagnet when the bearing force equals $F_{\max}$ with the nominal air gap. Let t_0 be the rise time for the magnet's current from zero to i_{fmax} when the maximum voltage $V_{\max}$ is applied over the coil. Note that the current in the nonloaded magnet is assumed to vanish when the force is $F_{\max}$. The value of the force bandwidth ω_{fmax} is based on this rise time:

$$\omega_{\text{fmax}} = \frac{2}{t_0}, t_0 = \frac{1}{V_{\max}} \int_0^{i_{\text{fmax}}} L_{\text{dyn}}(i)di \,. \tag{4}$$

For the test machine, i_{fmax}=6.9 A and ω_{fmax}=177 Hz. The definition of the force bandwidth is slightly arbitrary because it is difficult to predict accurately how high a first harmonic force the real nonlinear bearing is able to produce at a certain frequency. To understand the use of Equation 4, assume that i_{fmax}=2*i_{bias}, the dynamic inductance is constant up to i_{fmax} and the

current stiffness is constant. Then the bearing is able to produce an undistorted dynamic force $F_{\max}$ exactly up to the frequency ω_{fmax} achieved from Equation 4.

Because the bearing force is proportional to air gap field energy, the force bandwidth and the power amplifier capacity have the following fundamental relationship

$$V_{\max} i_{\text{fmax}} = F_{\max} \omega_{\text{fmax}} \delta k_{\text{dynf}} \ , \tag{5}$$

where δ is the air gap and
k_{dynf} is a correction factor, typically about 1.3.

A detailed derivation of Equation 5 is given by Bornstein (1991). The correction factor k_{dynf} is bigger than unity, due to stray fluxes and because the magnetic forces of the individual poles do not point exactly in the direction of the total force.

To test the force bandwidth prediction (Equation 4), the maximum achieved bearing force was measured from the test machine as a function of frequency. In Figure 7 the results are plotted. In the measurement, piezoelectric acceleration sensors were installed at the ends of the rotor. The rotor was levitating and sinusoidal disturbance was fed into the 2-end position controller output. The signals of the acceleration sensors were sampled and the Fourier series coefficient of the first harmonic was computed. At every frequency, the amplitude of this first harmonic force in the 2-end bearing was maximized by tuning the amplitude of the sinusoidal disturbance. From the acceleration signals, the bearing forces were determined using the rotor model with one bending mode.

This measurement procedure was not without problems. Below 100 Hz a contact with the retainer bearing occurs before the maximum force is achieved. At frequency 356 Hz, the frequency response matrix from bearing forces to acceleration signals becomes singular and the bearing forces cannot be determined uniquely from the acceleration measurements. This caused errors in the measured forces near 356 Hz.

As seen in Figure 7, the actual maximum bearing force is very near the predicted line achieved from Equation 4. Later, in the controller synthesis, the dynamic force limit is approximated by the following frequency response function (also shown in Figure 7)

$$F_{\text{b}}(\omega) < \left| G_{\text{flim}}(j\omega) \right|, \ G_{\text{flim}}(s) = \frac{\omega_{\text{fmax}} F_{\max}}{s + \omega_{\text{fmax}}}. \tag{6}$$

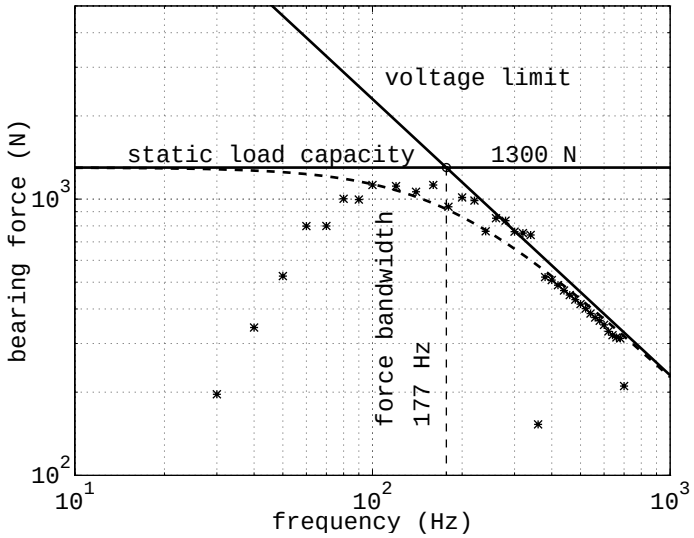

Figure 7. AMB dynamic load capacity. The asterisks (*) are measured points.

High amplitude response

The linearized model, with parameter uncertainty, is a useful actuator model for controller synthesis and analysis. However, at high reference signal amplitudes the force response deviates considerably from the linear model prediction. Let us next analyze how the first harmonic response behaves at large signal amplitudes.

The simulation model is shown in Figure 8. The voltage limit, current limit, variable dynamic inductance and nonlinear current-force relationship are taken into consideration. In the analysis, the sinusoidal reference current i_{cref} is fed into the amplifier at a certain frequency ω. Then, the system is simulated for several periods and the Fourier series expression is computed for the force. Finally, the first harmonic response $g(a_{\mathrm{i}},\omega)$ is obtained. Actually, more interesting than the first harmonic response is the relative response $g_{\mathrm{rel}}(a_{\mathrm{i}},\omega)$, i.e. the deviation from the small signal behavior. Also, the amplitude-scaled version $g_{\mathrm{relA}}(a_{\mathrm{i}},\omega)$ is used. These quantities are defined as follows:

$$i_{\mathrm{cref}}(t)=\mathrm{Re}\left(a_{\mathrm{i}}e^{j\omega t}\right),\ F_{\mathrm{b}}(t)=\mathrm{Re}\left(\sum_{n=1}^{\infty}a_{\mathrm{f}n}e^{j\omega nt}\right)+\text{"unharmonics"},\ a_{\mathrm{f1}}=\frac{2}{NT}\int_{NT}e^{-j\omega t}F_{\mathrm{b}}(t)dt,$$
$$g(a_{\mathrm{i}},\omega)=\frac{a_{\mathrm{f1}}}{a_{\mathrm{i}}},\ g_{\mathrm{rel}}(a_{\mathrm{i}},\omega)=\frac{g(a_{\mathrm{i}},\omega)}{g(0,\omega)},\ g_{\mathrm{relA}}(a_{\mathrm{i}},\omega)=\frac{g(a_{\mathrm{i}},\omega)}{|g(0,\omega)|}, \tag{7}$$

where the first Fourier coefficient a_{f1} is computed by integrating over a sufficient number of periods, N, to eliminate the effect of the unharmonic signals caused by high frequency disturbance i_{hf}.

This kind of a describing function analysis, which forgets the higher harmonics, is useful when the open-loop gain of the system decreases rapidly in the frequency range of interest, i.e. the higher harmonics will be effectively damped. This is the case with AMB, as seen in Chapter 3.

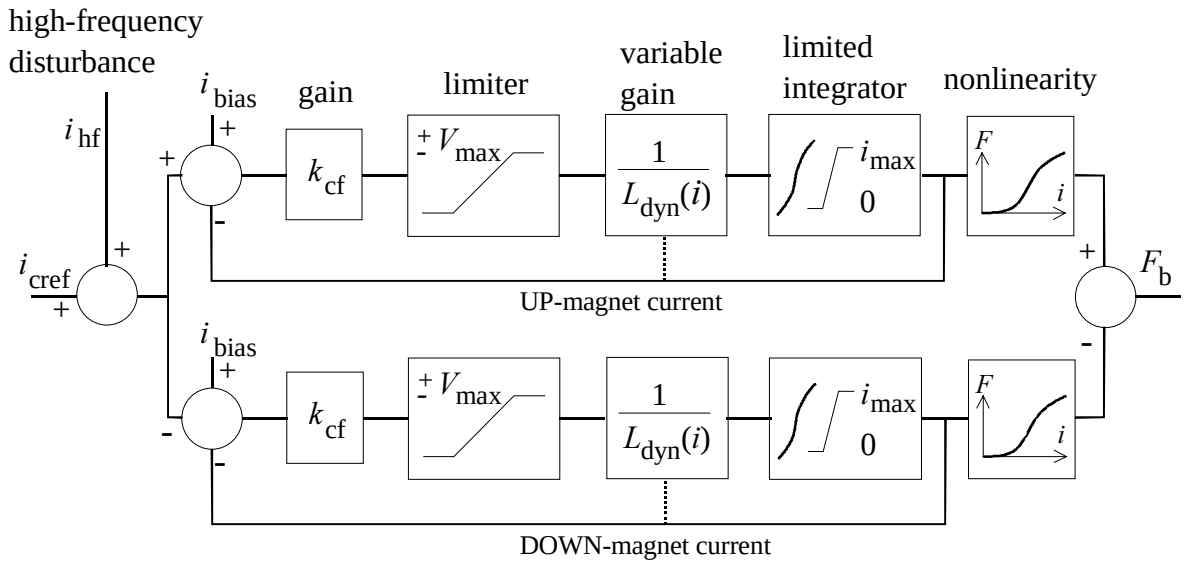

Figure 8. Simulation model for analyzing the amplifier saturation effects.

Let us first analyze the effect of high reference current amplitude alone. The high frequency disturbance i_{hf} is zero. In Figure 9 the response h_{rel} is computed for the frequencies 50, 75, 100, 150, 200, 250 and 300 Hz. The amplitude of the reference current is changed from a small value up to a very high value. The responses are computed with the current feedback coefficient k_{cf} =200 V/A. Values 150 V and 75 V were used for the maximum voltage V_{max}.

At low frequencies, only the gain decreases as the amplitude increases. This is because the dominant saturation is the current limit, which does not introduce phase lag. Actually, there will be a slight phase advance due to the drop of the dynamic inductance at high currents. At the higher frequencies, the voltage limit becomes dominant. Therefore, considerable phase drop occurs. Obviously, the voltage limit becomes dominant near the force bandwidth. As can be seen in Figure 9, the phase drop is clearly higher when the maximum voltage is only 75 V.

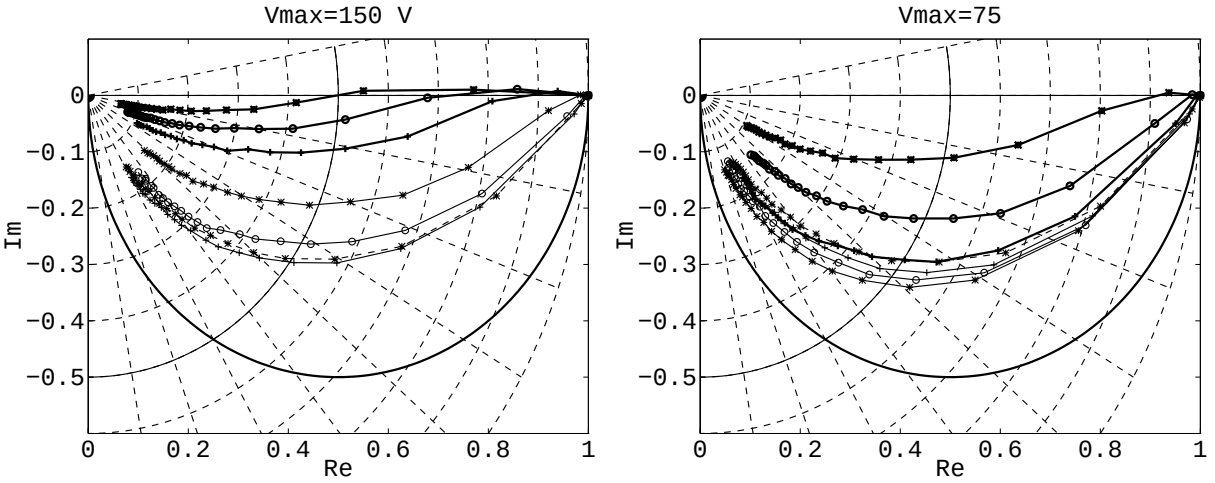

Figure 9. High amplitude actuator response $g_{\mathrm{rel}}(a_{\mathrm{i}},\omega)$. The frequencies are 50 Hz (bold *), 75 Hz (bold o), 100 Hz (bold +), 150 Hz (thin *), 200 Hz (thin o), 250 Hz (thin +) and 300 Hz (dashed line *). The amplitude a_{i} is increased from zero to a very large value. The sector lines are drawn with 10° increments.

The phase lag appearing at high frequency and high signal amplitudes is well known in the AMB community, and its seriousness is pointed out by several authors; see Ahrens and Kucera (1995), Maslen *et al.* (1989), Zmood *et al*. (1990) and Satoh *et al*. (1990). In the present publication, this effect is further analyzed in Section 3.5.

The effect of a high-frequency high amplitude disturbance

Next, the effect of power amplifier saturation due to high-frequency disturbance is analyzed. This may occur if the unbalance compensation has not succeeded in canceling the rotational synchronous current reference, or if there exist higher harmonics or the measurement noise is very strong. The frequency 500 Hz is near the maximum rotational speed of the test machine and a good candidate for high-frequency disturbance. Let us insert a sinusoidal disturbance into the amplifier input: $i_{\mathrm{hf}}(t) = a_{\mathrm{rel}}\mathrm{Re}\left(a_1 * e^{j*2*\pi*500*t}\right)$, where a_{rel} is a kind of saturation level and a_1=1.37 A is the disturbance for which the voltage swing is exactly $V_{\max}$.

Now, the high amplitude response $g(a_{\mathrm{i}},\omega,a_{\mathrm{rel}})$ is also a function of the saturation level. Actually, there no longer exist a Fourier-series expression for the force output. However, the first harmonic force vibration, a_{f1} in Equation 7 is computed as before, i.e. by integrating the force signal multiplied by the phase term over several periods.

On the left-hand side of Figure 10, the amplitude-scaled response $g_{\mathrm{relA}}(a_{\mathrm{i}},\omega,a_{\mathrm{rel}})$ is shown for small signal amplitude (a_{i}=0.2 A) for five saturation levels a_{rel} ={0, 1.25, 1.5, 2, 3}. The current feedback coefficient is k_{cf}=200 V/A. The case a_{rel}=0 is an undisturbed situation and it is computed for reference. On the right-hand side plot, the amplitude-scaled response is computed for higher signal amplitudes for six different saturation levels a_{rel} ={0, 1, 1.25, 1.5, 2, 3}. The saturation level 1 is included because the high amplitude response at the saturation border differs from the response without disturbance. The frequency 75 Hz is chosen because it turns out that the system goes into limit cycle oscillation near this frequency.

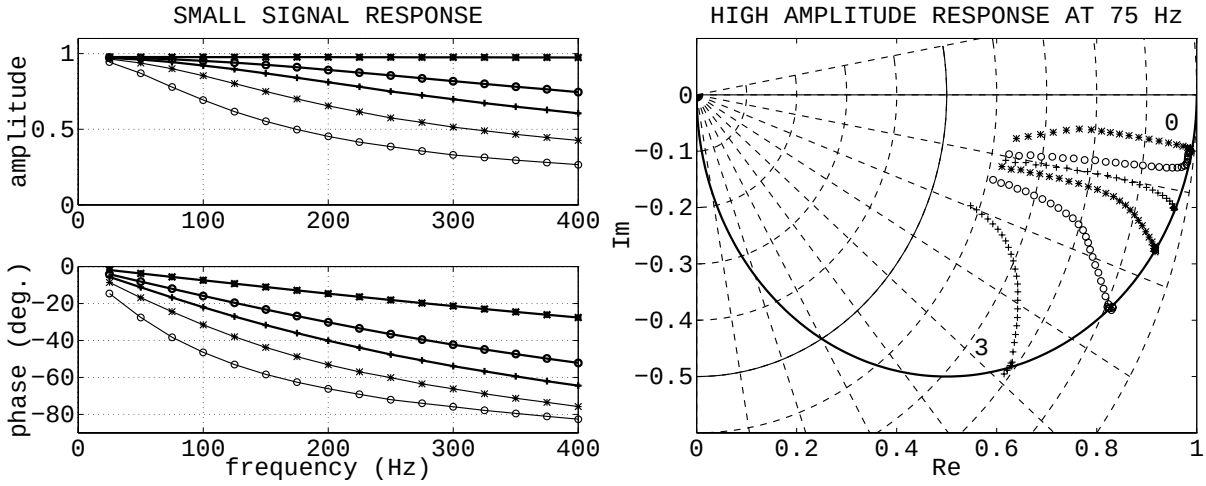

Figure 10. The effect of the amplifier saturation on the actuator response. On the left-hand side are the small signal responses for saturation levels a_{rel} ={ 0, 1.25, 1.5, 2, 3}. On the right-hand side the high signal response at frequency 75 Hz for saturation levels a_{rel} ={0, 1, 1.25, 1.5, 2, 3}.

From Figure 10 it can be seen that even a small saturation causes considerable phase lag. It is clear that amplifier saturation deteriorates the bearing dynamics considerably and high saturation may lead to instability, as shown by Larsonneur (1990). From the right-hand side plot it is seen that the small signal response goes along a semicircle centered at 0.5 and radius 0.5 (this is the reason for plotting amplitude-scaled curves). This is the locus of a first-order low-pass filter. This means that the amplifier saturation has the same effect as the decrease of the current feedback coefficient. Another observation is that the phase lag slightly decreases when the saturation level is high and the signal amplitude is increased. From this, one can predict that the system might go into stable limit-cycle oscillation at a certain saturation level. This is verified in Section 3.5.

2.3 The rotor model

Accurate rotor modeling is essential in the design of high-speed machines. The finite element model based on Timoshenko beam assumptions is accurate enough in the case of high-speed machines (Lantto 1997). The rotor is divided into a finite number of elements, typically about 30 elements. The rotor deformations in XZ- and YZ-planes are defined by the nodal deformation vectors $\boldsymbol{q}_X$ and $\boldsymbol{q}_Y$, respectively. A detailed derivation of the equation of motion is given by Lantto (1997). The equation of motion is

$$\begin{aligned}
&\boldsymbol{M}_{\mathrm{rot}}\ddot{\boldsymbol{q}}_X + \boldsymbol{D}_{\mathrm{rot}}\dot{\boldsymbol{q}}_X + \boldsymbol{K}_{\mathrm{rot}}\boldsymbol{q}_X - c_0\boldsymbol{B}_{\mathrm{b}}\boldsymbol{B}_{\mathrm{b}}^{\mathrm{T}}\boldsymbol{q}_X + \\
&\qquad \Omega\boldsymbol{G}_{\mathrm{rot}}\dot{\boldsymbol{q}}_Y + \Omega\boldsymbol{D}_{\mathrm{rot}}\boldsymbol{q}_Y = \boldsymbol{B}_{\mathrm{b}}\boldsymbol{F}_{\mathrm{bcur}X} + \boldsymbol{F}_{\mathrm{E}X} + \Omega^2\left(\cos(\beta)\boldsymbol{U}_X - \sin(\beta)\boldsymbol{U}_Y\right), \\
&\boldsymbol{M}_{\mathrm{rot}}\ddot{\boldsymbol{q}}_Y + \boldsymbol{D}_{\mathrm{rot}}\dot{\boldsymbol{q}}_Y + \boldsymbol{K}_{\mathrm{rot}}\boldsymbol{q}_Y - c_0\boldsymbol{B}_{\mathrm{b}}\boldsymbol{B}_{\mathrm{b}}^{\mathrm{T}}\boldsymbol{q}_Y - \\
&\qquad \Omega\boldsymbol{G}_{\mathrm{rot}}\dot{\boldsymbol{q}}_X - \Omega\boldsymbol{D}_{\mathrm{rot}}\boldsymbol{q}_X = \boldsymbol{B}_{\mathrm{b}}\boldsymbol{F}_{\mathrm{bcur}Y} + \boldsymbol{F}_{\mathrm{E}Y} + \Omega^2\left(\sin(\beta)\boldsymbol{U}_X + \cos(\beta)\boldsymbol{U}_Y\right), \\
&\boldsymbol{p}_{\mathrm{b}} = \begin{bmatrix} \boldsymbol{B}_{\mathrm{b}}^{\mathrm{T}} & \boldsymbol{0} \\ \boldsymbol{0} & \boldsymbol{B}_{\mathrm{b}}^{\mathrm{T}} \end{bmatrix}\begin{bmatrix} \boldsymbol{q}_X \\ \boldsymbol{q}_Y \end{bmatrix}, \quad \boldsymbol{p}_{\mathrm{S}} = \begin{bmatrix} \boldsymbol{C}_{\mathrm{S}} & \boldsymbol{0} \\ \boldsymbol{0} & \boldsymbol{C}_{\mathrm{S}} \end{bmatrix}\begin{bmatrix} \boldsymbol{q}_X \\ \boldsymbol{q}_Y \end{bmatrix},
\end{aligned} \tag{8}$$

where

Ω	is rotational speed,
β	is rotation angle ($\Omega = \dot{\beta}$),
c_0	is nominal position stiffness,
$\boldsymbol{q}_X$, $\boldsymbol{q}_Y$	are rotor deformation vectors in XZ and YZ-planes,
$\boldsymbol{M}_{\mathrm{rot}}$, $\boldsymbol{D}_{\mathrm{rot}}$, $\boldsymbol{K}_{\mathrm{rot}}$, $\boldsymbol{G}_{\mathrm{rot}}$	are mass, damping, stiffness and gyroscopic matrices,
$\boldsymbol{B}_{\mathrm{b}}$	is transformation from bearing forces to generalized forces,
$\boldsymbol{C}_{\mathrm{S}}$	is transformation from generalized coordinates to displacements in the sensor locations,
$\boldsymbol{U}_X$, $\boldsymbol{U}_Y$	are unbalance vectors,
$\boldsymbol{F}_{\mathrm{bcur}X}$, $\boldsymbol{F}_{\mathrm{bcur}Y}$	are controlled bearing forces,
$\boldsymbol{F}_{\mathrm{E}X}$, $\boldsymbol{F}_{\mathrm{E}Y}$	are generalized external forces,
$\boldsymbol{p}_{\mathrm{b}}$	is rotor displacements in the bearing locations and
$\boldsymbol{p}_{\mathrm{S}}$	is rotor displacements in the sensor locations.

Note that the position stiffness effect is included as a part of the rotor model.

The FEM model is of a high order and too heavy for control system design and analysis. There are several possible reduction techniques, perhaps the most popular being modal reduction. In modal reduction, a modal coordinate transformation is done where the mass and stiffness matrices become diagonal. Also, the damping matrix is usually assumed to be

diagonal. Then, the irrelevant high frequency modes are truncated. The form of the equation of motion is the same as in the higher order model.

Modal reduction is done for unsupported nonrotating rotor. The number of relevant bending modes is typically one, two or three. Modal reduction in free supports works well, because the high-speed rotors are not too gyroscopic, i.e. the rotational speed does not change the bending mode shapes considerably (see Appendix C). Also, the bearings are soft compared to the rotor and they do not change the bending mode shapes too much. In this publication the model after modal reduction is used, except in the rest of this section.

About the bending critical speeds

In the high-speed machines, a subcritical operation is preferred, because the passing of the bending critical speeds is difficult. The fundamental difficulty is not the more complicated bearing control, but the high bearing force needed to pass a high-frequency bending critical speed. The bearing force can be decreased by balancing the rotor, but the balancing requirements may become unpractically tight. The bearing force needed to pass bending critical speed is studied in this section.

As shown by Genta and Delprete (1995), a correct dynamic analysis of the critical speed passing is a complicated task. The vibration amplitudes can be very different when the acceleration is slow or fast. In this short discussion, only the case of very slow acceleration is considered. To analyze the rotational synchronous bearing force needed to rotate steadily at a certain speed, let us introduce a complex equation of motion in the rotating reference frame (see Lantto 1997 for details). The full order FEM model is used.

$$\boldsymbol{M}_{\mathrm{rot}}\ddot{\boldsymbol{q}}'_{\mathrm{C}} + \left[\boldsymbol{D}_{\mathrm{rot}} + j\Omega\left(2\boldsymbol{M}_{\mathrm{rot}} - \boldsymbol{G}_{\mathrm{rot}}\right)\right]\dot{\boldsymbol{q}}'_{\mathrm{C}} + \left[\boldsymbol{K}_{\mathrm{rot}} - \Omega^2\left(\boldsymbol{M}_{\mathrm{rot}} - \boldsymbol{G}_{\mathrm{rot}}\right)\right]\boldsymbol{q}'_{\mathrm{C}} = \boldsymbol{B}_{\mathrm{b}}\boldsymbol{F}'_{\mathrm{bC}} + \Omega^2\boldsymbol{U}_{\mathrm{C}}\ , \quad (9)$$

where j is the imaginary unit,
$'$ refers to the rotating coordinate system and
sub C means complex coordinates:
$\boldsymbol{q}'_{\mathrm{C}} = \boldsymbol{q}'_X + j\boldsymbol{q}'_Y, \boldsymbol{F}'_{\mathrm{bC}} = \boldsymbol{F}'_{\mathrm{b}X} + j\boldsymbol{F}'_{\mathrm{b}Y}, \boldsymbol{U}_{\mathrm{C}} = \boldsymbol{U}_X + j\boldsymbol{U}_Y$.

In the steady state the rotor is stationary in the rotating frame and Equation 9 reduces to

$$\left[\boldsymbol{K}_{\mathrm{rot}} - \Omega^2\left(\boldsymbol{M}_{\mathrm{rot}} - \boldsymbol{G}_{\mathrm{rot}}\right)\right]\boldsymbol{q}'_{\mathrm{C}} = \boldsymbol{B}_{\mathrm{b}}\boldsymbol{F}'_{\mathrm{bC}} + \Omega^2\boldsymbol{U}_{\mathrm{C}} \ . \tag{10}$$

When the matrix $\left[\boldsymbol{K}_{\mathrm{rot}} - \Omega^2\left(\boldsymbol{M}_{\mathrm{rot}} - \boldsymbol{G}_{\mathrm{rot}}\right)\right]$ is nonsingular, the rotational synchronous bearing force can be zero and still the deformation vector remains bounded. This kind of situation is possible and often preferred in the case of AMB (see Chapter 4). However, when the matrix is near singular, the deformations will be very high even for a small unbalance. When it becomes singular, bearing forces become necessary to keep the rotor bending limited.

Assume that the matrix is singular at some speed $\Omega_{\mathrm{crf}n}$. These critical speeds can be calculated from a generalized eigenvalue problem:

$$\Omega^2_{\mathrm{crf}n}\left(\boldsymbol{M}_{\mathrm{rot}} - \boldsymbol{G}_{\mathrm{rot}}\right)\boldsymbol{v}_n = \boldsymbol{K}_{\mathrm{rot}}\boldsymbol{v}_n \ . \tag{11}$$

The eigenvalue problem also has solutions where the eigenvalue $\Omega^2_{\mathrm{crf}n}$ is zero or negative. Physically, the negative eigenvalues correspond to bending modes where the eigenfrequency increases faster than the rotational speed, i.e. the rotational speed never reaches the forward rotating eigenfrequency. The two zero eigenvalues corresponds to the rigid body translatory and conical modes. The smallest positive solution Ω_{crf3} is the first bending critical speed for the unsupported rotor, Ω_{crf4} is the second bending critical speed for the unsupported rotor, etc.

Because the matrices $\boldsymbol{M}_{\mathrm{rot}}$, $\boldsymbol{G}_{\mathrm{rot}}$ and $\boldsymbol{K}_{\mathrm{rot}}$ are symmetric, the eigenvectors and eigenvalues are real. Let us scale the eigenvectors so that the maximum rotor deformation is 1 (m). Let $\Omega = \Omega_{\mathrm{crf}n}$ and multiply Equation 10 from the left by $\mathbf{v}_n^{\mathrm{T}}$:

$$\boldsymbol{v}_n^{\mathrm{T}}\left[\boldsymbol{K}_{\mathrm{rot}} - \Omega^2_{\mathrm{crf}n}\left(\boldsymbol{M}_{\mathrm{rot}} - \boldsymbol{G}_{\mathrm{rot}}\right)\right]\boldsymbol{q}'_{\mathrm{C}} = \boldsymbol{v}_n^{\mathrm{T}}\boldsymbol{B}_{\mathrm{b}}\boldsymbol{F}'_{\mathrm{bC}} + \Omega^2_{\mathrm{crf}n}\boldsymbol{v}_n^{\mathrm{T}}\boldsymbol{U}_{\mathrm{C}} \ . \tag{12}$$

The left part is zero because $\boldsymbol{v}_n^{\mathrm{T}}$ and $\Omega^2_{\mathrm{crf}n}$ are a solution to Equation 11. The term $\boldsymbol{v}_n^{\mathrm{T}}\boldsymbol{U}_{\mathrm{C}}$ is called the nth modal unbalance U_n. It can be interpreted as an unbalance connected to the location of maximum vibration amplitude of the corresponding unsupported mode, and having the same effect on this mode as the true unbalance distribution. If the machine has 2 radial

bearings, then $\boldsymbol{v}_n^{\mathrm{T}}\boldsymbol{B}_{\mathrm{b}} = \begin{bmatrix} b_{n1} & b_{n2} \end{bmatrix}$, where $b_{n1,2}$ are real and their absolute value is the vibration amplitude of the bending mode at the bearing location, when the maximum amplitude of the mode shape is scaled to 1 (m). Therefore, Equation 12 can be written as follows

$$\begin{bmatrix} b_{n1} & b_{n2} \end{bmatrix}\boldsymbol{F}'_{\mathrm{bC}} = -\Omega^2_{\mathrm{crfn}} U_n \ . \tag{13}$$

So, at the unsupported bending critical speed the weighted vector sum of the bearing forces is determined by the modal unbalance. To minimize the greater of the bearing forces it is necessary to make both forces equal in magnitude and in such a phase that they both work against the unbalance. This leads to minimum force demand to pass the unsupported bending critical speed:

$$F_{\mathrm{bmin}n} = \frac{\Omega^2_{\mathrm{crf}n}\left|U_n\right|}{\left|b_{n1}\right| + \left|b_{n2}\right|} \ . \tag{14}$$

It is interesting to see that the minimum bearing force does not depend on the bearing characteristics. Only bearing locations and unbalance distribution affect the minimum force demand (this is also mentioned by Haberman and Brunet 1986). Thus, the unsupported bending critical speeds are important in a fundamental manner.

In this section, it has been shown that a certain rotational synchronous bearing force is needed at the unsupported bending critical speeds and that at other speeds no force is needed, in theory. Of course, to limit the vibration amplitudes, bearing forces become necessary at least near these speeds. However, it is fairly clear that if the bearings are controlled in an optimum way, the highest force is needed exactly at the unsupported bending critical speed. Maslen and Allaire (1992) have studied the bearing force demands under vibration constraints and have come to the same conclusion.

As seen in Equation 14, the force demand increases relative to the square of the critical speed. From Section 2.2 it is remembered that the achieved bearing force decreases as $1/\Omega$ at high frequencies. Further, we notice (see Appendix C) that in a high speed-rotor construction the bearings are often quite near the bending mode nodes and cannot effectively damp the vibration, i.e. the absolute values of b_{n1} and b_{n2} are small. So, it is obvious that passing a high-frequency bending critical speed demands high dynamic load capacity from the bearings

and/or leads to tight balancing requirements. The following numerical example sketches the practical values for the force demand and the effect of the bearing characteristics.

A numerical example of the passing of the first bending critical speed

Let us consider passing the first bending critical speed with the test machine (Appendix C). The first unsupported bending critical speed is 685 Hz according to FEM calculations. To estimate the practical unbalance levels, let us use the balancing results in Section 4.4. There, the first modal unbalance was 265 gmm before balancing and 22 gmm after balancing. For this test machine b_{31}=0.15 and b_{32}=0.25. With 22 gmm modal unbalance this leads to a minimum force demand of 1000 N at 685 Hz. This is clearly above the dynamic load capacity shown in Figure 7. The bearing could produce 300 N at this frequency, which would allow a 6 gmm modal unbalance. Even though that small unbalance can be obtained by tedious balancing, the unbalance is not likely to remain below this limit in the long run. For example, tension relaxations in the rotor could easily raise the unbalance above the allowed limit. So, in this machine type the electromagnets are slightly too small and the power amplifier is clearly too weak to make a practical supercritical machine. However, these facts do not prevent us from using this machine as a fictitious example.

Assume that the bearing dynamics at the frequencies near the first bending critical speed can be described by a single spring and viscous damper: $\boldsymbol{F}_{\mathrm{b}} = -k\boldsymbol{p}_{\mathrm{b}} - \left(d / \Omega_{\mathrm{crf3}}\right)\dot{\boldsymbol{p}}_{\mathrm{b}}$. Further, let us use similar bearings at both rotor ends. Three different cases were computed. In all the cases d=30*10^6 N/m. Three different values were given for k: –30*10^6 N/m (thin line in Figure 11), +30*10^6 N/m (dashed line) and 0 N/m (bold line). No unbalance was assumed for the rigid body modes and the first bending mode unbalance was assumed to be 22 gmm. The bearing force and the vibration amplitude at 2-end bearing are plotted in Figure 11. At the 2-end bearing the force and the vibration are higher.

As seen in Figure 11, the resonance maximum can be shifted by bearing characteristics, but the bearing force can’t be dropped near the unsupported critical speed. Another observation is that the smallest peak force is achieved when the bearings are acting as pure dampers. Generally, it is a well-known fact that at bending critical speed the bearing characteristics should be as pure a damper as possible (Haberman and Brunet 1986).

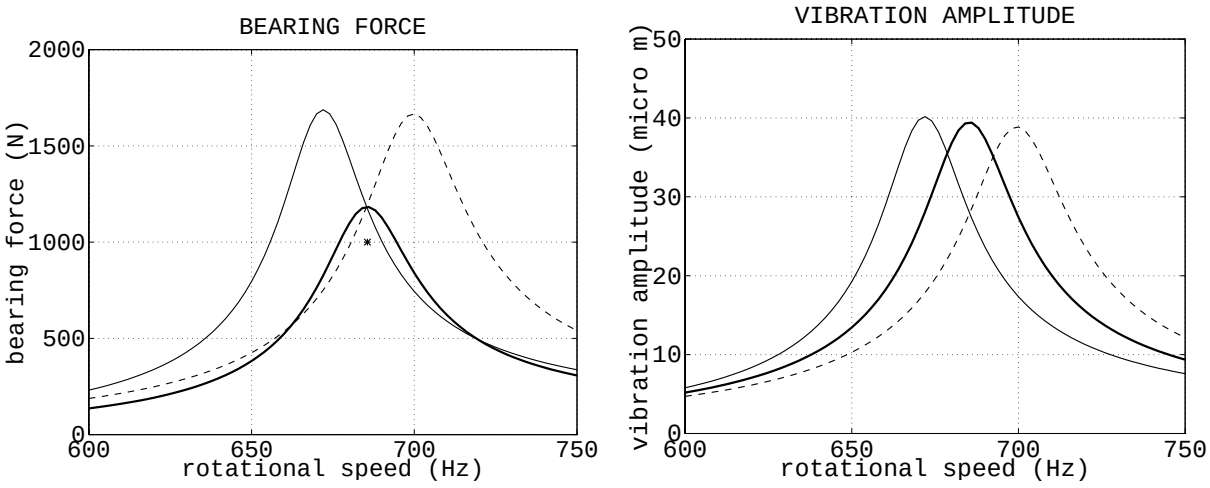

Figure 11. Passing of the first bending critical speed. Bearing force is on the left-hand side and vibration amplitude on the right-hand side. The minimum force at the unsupported bending critical speed 685 Hz is 1000 N, labeled with an asterisk (*). Solid line: negative stiffness, dashed line: positive stiffness, bold line: no stiffness, only damping.

The reason why the force in Figure 11 is not exactly the theoretical minimum is that the bearing stiffnesses are assumed the same at both bearings. Consequently, the bearing forces are not equal, because the first bending mode is vibrating slightly more in the 2-end bearing.

One special feature that should be kept in mind in the passing of the bending critical speeds is the power consumption. At the bending critical speed, the electric motor pushes energy into the rotational movement. The unbalance distribution transforms this rotational energy into lateral vibrations and the bearings transfer this vibration power out of the mechanical system. Thus, AMB is behaving as a generator and power is going from the electromagnets to the electronics. In the present example, this power was only 280 W. The power depends on the bearing characteristics and would be 1 kW if d=10*10^6 N/m. At least in theory, this power might be bigger than the power loss of the amplifier and electromagnets, and consequently the power supply should push the extra power somewhere.

The following conclusion can be made about the passing of the bending critical speed with AMB: First, the unsupported bending critical speeds to be passed should be shifted to as low a frequency as possible by mechanical design. Secondly, the bearing locations should be chosen so that the bearings are able to damp the relevant bending modes effectively. Thirdly, the AMB dynamic load capacity should be high enough to handle the practical residual unbalances.

2.4 Disturbance forces

The rotor is subjected to many kinds of disturbance forces that should be handled by AMB. Some types of forces can be described as pure external disturbances. Many forces, however, depend on the rotor displacement and consequently affect the dynamics of the suspension.

Electric motor forces

The electric motor is usually large compared to AMB and the flux densities are of the same order as in AMB. Consequently, the electric motor might cause considerable radial forces compared to the AMB load capacity. The radial loads caused by the induction motor are studied in several works of Arkkio (1994, 1995, 1996, 1997). In this section a short summary of these studies is given.

In the case of a slotted rotor, there may be considerable high frequency radial forces due to strong local interactions between stator and rotor teeth, see Arkkio (1995). With a bad choice of slot numbers, these forces will be strong enough to excite rotor bending modes and other structural resonances. However, in the high-speed motors being made in our project, the most common motor construction is a two-pole solid rotor type induction motor with no slots in the rotor. In this kind of motor, the radial forces are negligible if the rotor is perfectly rotationally symmetric, rotating around its geometrical axis and located in the center of the stator packet. There are, however, several kinds of unidealities that produce considerable radial forces.

In the case of static eccentricity the rotor is symmetric and rotates around its center. This rotation axis is shifted from the stator center. This case is analyzed by Arkkio and Lindgren (1994) and Arkkio (1996). In this case, a static radial force component is generated which points in the direction of eccentricity. There is also a force component perpendicular to the displacement, pointing in the direction of the rotation. This perpendicular force component disappears already at low speed. The force is approximately linearly dependent on the eccentricity. So it cannot be described only as an external disturbance force, but as a destabilizing spring, like the position stiffness in AMB. This effect is highest at very low speeds (below 1 Hz), and at higher speeds it settles to a considerably smaller constant value which is small enough to be negligible considering suspension dynamics. Consequently, the static load at high speed also remains at a low level. The static force increases as the motor is

loaded. The increase is not, however, very great and the frequency converter effectively prevents overload situations. Due to static eccentricity a rotating force at a frequency twice the field rotation speed is also generated. This force is almost independent of the rotational speed and its magnitude is so low that it has no significant effect.

Dynamic eccentricity is an unideality where the rotation axis is deviated from the rotor's geometric center. Dynamic eccentricity causes a rotating force at frequency Ω, see Arkkio (1996). This force is almost independent of the speed and its magnitude is relatively high. Motor loading decreases the force caused by dynamic eccentricity. A force rotating at the same speed as the rotor is not so dangerous because the unbalance compensator prevents the power amplifier from saturation.

Also an asymmetric rotor causes considerable radial forces, see Arkkio (1997). The asymmetry may be due to broken rotor bars in ordinary cage-induction motors or asymmetry in the copper coating in the case of a high-speed rotor. This kind of unideality results in a rotating force with pulsating amplitude. This force might become a problem because the unbalance compensation is not able to follow the pulsation, and consequently power amplifier saturation may occur if the force is high enough.

Aerodynamic forces

In the high speed machines made in our project, the load machine is most often a one-stage centrifugal air compressor. Even though the pressure ratio is typically only 2:1, considerably static aerodynamic forces affect the impeller (Antila *et al.* 1996). The axial forces are typically much higher than the radial ones. Fortunately, the axial forces can be predicted quite accurately. Radial forces are more difficult to predict but, in the low-pressure compressors, they are small compared to the radial bearing load capacity. In high-pressure compressors, however, the radial loads may be significant and should be carefully analyzed (Agahi 1994).

Besides the static loads, the air flow causes stochastic excitation at low frequencies, below 100 Hz, in radial and axial directions. In normal operation, these forces remain quite low. However, when the air flow is choked too much, the flow becomes unstable and starts oscillating at a frequency that depends on the compressor and surrounding pipes (Hampel 1995). In this surge condition, high vibrating radial and axial forces will occur. The frequency

of such forces is typically below 30 Hz and the amplitude may become high, compared to the AMB load capacity.

Generally, in turbomachinery, the seals and other small clearances between the rotor and stator may have a considerable effect on the rotordynamics, see Vance (1988). The effect of these small clearances can be described as direct and cross-connected stiffness and damping coefficients. However, in the compressors dealt with in this publication, these effects are negligible, due to relatively large clearances and low pressures.

The compressor forces are not only a nuisance. The radial and axial forces correlate very well with the operational point of the compressor as shown by Antila *et al*. (1996). Consequently, the force measurements achieved from AMB can be utilized for compressor control purposes. For example, an effective surge protection system can be realized with AMB.

Unbalance

Actually, the rotor unbalance is not an external force. However, it can be interpreted as a disturbance force rotating at the rotational speed. In the case of AMB the rotational synchronous bearing force can be eliminated effectively by a special unbalance compensator, described in Chapter 4. Because of that, highly unbalanced rotors can be rotated with AMB. Also, if the unbalance is too high, AMB can be used as a balancing machine (see Section 4.4). Of course, in the case of supercritical machines the unbalance associated with the passed bending modes will be of major importance, as seen in Section 2.3.

Other forces and disturbances

All machines on earth are subject to gravitational load. This static load can be easily predicted. If AMB should operate in a moving vehicle, then the accelerations of that vehicle may increase the load capacity demand. Even in stationary installations there are norms for the base vibrations that the machine should tolerate. These vibrations could be caused by, for example, surrounding machines and geological factors.

The position sensor may have certain unidealities that cause disturbance signals. For example, the rotor side of the sensor may be eccentric, its shape can be deviated from a circle

or its surface may have small errors. A pure eccentricity can be interpreted as a rotor unbalance and it is not so dangerous. Other unidealities cause higher harmonics that are more difficult to handle.

The effect of the disturbance forces on the AMB design

AMB has limited load capacity and practically nonexistent instantaneous overload capacity. Usually, building bearings which are clearly too strong is not a good practice, because it leads to a longer rotor and smaller margin to the first bending critical speed. Also, very strong amplifiers are costly. So, the disturbance forces should be accurately predicted and sufficiently strong electromagnets and power amplifiers are chosen with some safety factor depending on the reliability of the disturbance force predictions. Next, assume that the bearing magnets and amplifier are given and the question is, how should the disturbance force characteristics affect the AMB control system design ?

First, the unbalance is not given great consideration in the position controller design. That is because the rotational synchronous signals can be effectively manipulated by a special unbalance compensator. Using this compensator, AMB can be made to tolerate as high an unbalance as is physically possible.

Secondly, we notice that there exist forces that can be described as springs, i.e. they affect the suspension dynamics. The bearing stiffness should be clearly higher than the destabilizing effects of the electric motor and other factors. In high-speed motors, the stiffness will be high enough already for other reasons.

The third observation is that the most considerable forces exist at low frequencies: forces caused by the electric motor and surge. So, if some kind of compromise should be made between high and low frequencies, then the low frequencies should be slightly preferred. However, there are also forces at high frequencies that cannot be handled by the unbalance compensator, like the pulsating electric motor force, rapidly changing unbalance vibrations in fast accelerations and decelerations, measurement noise caused by surface runout, etc. Accordingly, the high frequencies must not be forgotten.

3 POSITION CONTROL LOOP

3.1 Literature review

The AMB suspension is an interesting system from the control engineering point of view. It is an unstable multivariable plant with changing parameters, nonlinearities and unmodeled dynamics. To handle the nonlinearities and uncertainties, some nonlinear approaches have been tested. For example, Tian and Nonami (1994) and Charara *et al*. (1996) have used sliding mode control to make a robust system. Even though the results are promising, the true advantage of the nonlinear approaches compared to well-designed linear controllers has not yet been shown very clearly.

Actually, the AMB suspension is not so nonlinear as one might expect, because the bias current linearizes the actuator very well. Also, the interactions between control channels are sometimes quite small. Therefore, the most common controller structure is decentralized control where all channels are separately controlled by PID-type controllers. In the case of a rigid rotor this approach often works well. However, when the bending modes become near the control bandwidth, a simple PID-controller is no longer sufficient and higher order controllers are needed. Often, a decentralized controller which is good enough can be obtained by human intuition and process knowledge, as shown by Förch *et al*. (1996), Delprete *et al*. (1994), Schmied (1990) and Matsushita *et al*. (1992). At some point, however, the decentralized control strategy is insufficient and cross-connections become necessary. Then we talk about centralized control. For example, highly gyroscopic rotors need cross-connections between X and Y channels to handle the gyroscopic effect, see Ahrens *et al*. (1996) and Zhuravlyov *et al*. (1994). Also, with negligible gyroscopic effects, the cross-connections between the two rotor ends sometimes become necessary, especially when the bending modes need to be controlled effectively. At some point, the system becomes too complicated and powerful design tools are needed.

The traditional LQG-theory is used by several authors, see especially Maslen (1991). A problem with the basic theory is that the controller will be of a high order and difficult to implement with analog circuits or a digital controller. Therefore, parametric optimization is

used to achieve the parameters of a predefined low-order controller; see Bleurer (1984) and Larsonneur (1990).

H_∞-theory is also widely used to achieve the performance limits of an AMB system and to synthesize the controllers. Yamashita *et al*. (1996) have used H_∞-optimization for low-frequency disturbance attenuation. Matsumura *et al*. (1996) have used H_∞-theory to obtain a controller to achieve good dynamic properties combined with rotational synchronous vibration cancellation. Fujita *et al*. (1993) have used the loop-shaping approach. Herzog *et al*. (1992) have studied compliance minimization and revealed certain nontrivial performance limitations using H_∞-theory.

In the case of AMB, H_∞-theory is useful in determining performance limits and synthesizing the controllers. However, the robustness is not correctly taken into consideration, particularly because many of the potential uncertainties are structured. For example, uncertain sensor sensitivity and uncertain current stiffness lead to real parameter uncertainty. To synthesize controllers to optimize worst-case performance, μ-synthesis has been used. Stephens and Knospe (1996) and Fittro *et al*. (1996) have used μ-synthesis for point compliance minimization in the case of an elastic rotor. They modeled the uncertainties in the correct way and obtained robust performance which was clearly better than the result achieved by the PID-controller. Also Fujita *et al*. (1992) and Nonami and Ito (1996) have used μ-synthesis to obtain a controller for an elastic rotor.

The problem with all the modern synthesis methods, especially with the μ-synthesis, is the high order of the resulting controller. Also, the necessary sampling rate in the AMB system is high. However, modern signal processors have made it possible to implement these high-order controllers. Thus, the use of modern synthesis methods is well established if they really provide better properties than simple approaches. Point compliance minimization is a problem in which the actual performance demand can be quite easily formulated into mathematical form. Consequently, the modern synthesis methods are very useful. However, in the case of subcritical compressor applications, which are the main subject of this thesis, the performance objective is not so clear. The main demand is that the machine can be run without problems in all the operational conditions. In practice, it has been seen that this goal is achieved when the open loop has a certain “shape”.

In this chapter the performance limits are first sought for the suspension of a point mass. It is shown that this limit cannot be achieved at every frequency, but a compromise should be made. Then the damping of the bending mode is studied in the scalar case, the ideas are generalized to the multivariable system and it is shown that the optimal controller has essentially a structure where the plant is diagonalized by two constant rotation matrices, and a diagonal controller is constructed for this diagonalized plant. It turns out that the open loop of a good control system is normal at both the plant input and plant output. Based on the structure of the optimal controller, a straightforward synthesis method is proposed where the diagonalization is done by the rotation matrices and the two controllers are designed using the SISO synthesis. To analyze the robustness of the resulting multivariable system, a generalized Nyquist diagram is proposed. This method gives nonconservative stability robustness estimates, especially in the case of almost normal open loop. At the end, the amplifier saturation effects are studied both theoretically and experimentally.

3.2 The SISO case

Let us first study the SISO magnetic suspension. Even though the real AMB system is usually a true MIMO plant, this study gives a valuable physical insight into the problem. Further, in the synthesis method developed in Section 3.4 the plant is separated into two SISO systems. For these reasons, it is worth studying the SISO case in detail.

Physical performance limit for a point mass suspension

The fundamental function of AMB is to keep the rotor in levitation under the disturbance forces. In Section 2.4 it was found that many disturbance forces are acting at one frequency simultaneously. Thus, a reasonable starting point for analyzing the achievable limits is to study how high a sinusoidal disturbance force the suspension system might tolerate at different frequencies if the bearings were used in an optimal way.

Assume that the levitated object is a point mass that moves only in one direction. The mass is m_r=22 kg and the position stiffness is c_r=2.1*10^6 N/m. At this point, we really study the suspension of a point mass. However, the mass and position stiffness are computed for the test

machine with the assumption that the two rotor ends do not interact. This choice is made in order to test this synthesis strategy later. The computing of these parameters is explained in Section 3.4.

Two forces are acting on the rotor: the disturbance force F_{d} and the controlled bearing force F_{bcur}; see Figure 12. To be accurate, the position stiffness effect should be considered as a part of the controlled bearing force because control voltage is needed to produce the destabilizing effect. However, the position stiffness is here included into the rotor model because it makes this analysis more clear and has practically no effect on the following results. The system model is simply

$$\begin{aligned} p_{\mathrm{x}}(s) &= R(s)\left[F_{\mathrm{bcur}}(s) + F_{\mathrm{d}}(s)\right], \\ R(s) &= \frac{1}{m_{\mathrm{r}}s^2 - c_{\mathrm{r}}}. \end{aligned} \tag{15}$$

A clear performance objective is that the bearings should prevent the rotor from contacting the retainer bearings. The retainer bearing air gap is 250 μm, so let us choose the maximum allowed displacement $p_{\max}$=200 μm.

Assume a sinusoidal disturbance force F_{d}*sin(ωt). The disturbance force can be maximized when the absolute value of the controlled bearing force is maximum, i.e. $\left|G_{\mathrm{flim}}(j\omega)\right|$ (Equation 6) and exactly in the opposite phase compared to the disturbance force, and the position vibration is exactly $p_{\max}$. The disturbance force is then

$$F_{\mathrm{dmax}}(\omega) = \left|R^{-1}(j\omega)p_{\max}\right| + \left|G_{\mathrm{flim}}(j\omega)\right|. \tag{16}$$

The first part is called “inertial force” because it is the force needed to vibrate the mass, and the second part is the dynamic bearing force. This maximum force is drawn in Figure 12. As can be seen, the suspension system tolerates very high forces acting on the rotor at high frequency. This is due to the large air gap. The force needed to cause a certain vibration amplitude increases relative to the square of the frequency. At low frequencies, the maximum force is limited by the static load capacity. The discrepancy at low frequencies (Figure 12) is because the position stiffness effect is included in the rotor model.

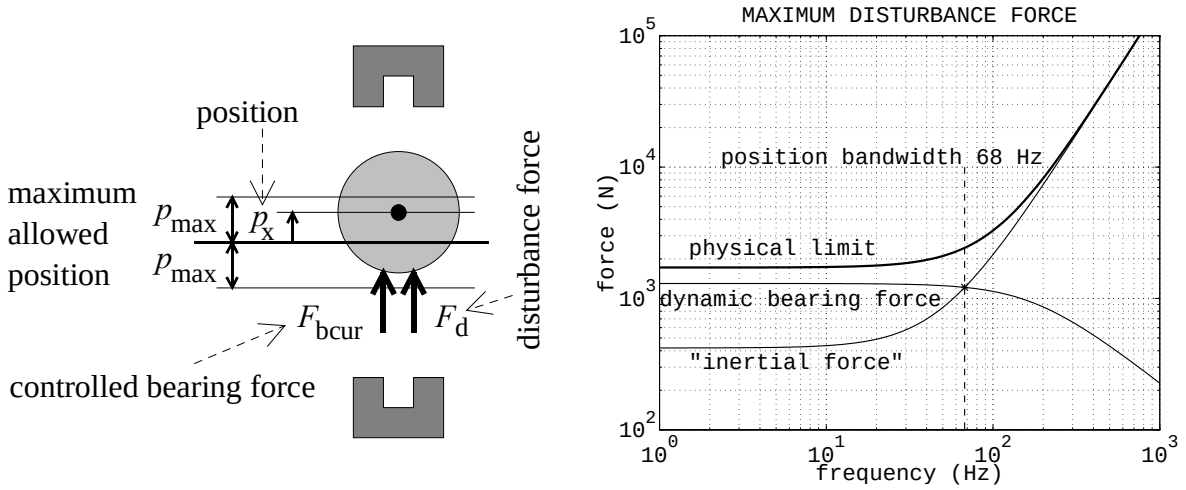

Figure 12. The point mass suspension and the physical performance limit.

The frequency where the maximum bearing force equals the force needed to cause vibration p_{max} is called position bandwidth ω_{pos}; in this case ω_{pos}=68 Hz. Well below this frequency the bearing is able to control the rotor position effectively, and well above this frequency, the bearing force cannot change the rotor vibration considerably.

If the bearing force is produced by feedback from the position measurement, then the optimum feedback coefficient is obviously $F_{bcur}(j\omega) = k_b p_x(j\omega)$, where $k_b = |G_{flim}(j\omega)|$. This feedback cannot be produced by a rational transfer function, and it would lead to an unstable system. Thus, it is obvious that a single controller cannot achieve the physical performance limit at every frequency.

Worst frequency optimal controller for point mass levitation

Because the physical performance limit cannot be achieved at every frequency, let us study how far from this limit we are pushed at the worst frequency. H_∞-optimization is an obvious method for such study. The system $R(s)$, which is essentially a slightly unstable double integrator (a textbook inverted pendulum), is not too difficult to control and H_∞-optimization is not needed to find a good controller. However, in the present analysis, H_∞-optimization is used to ensure that the achievable limit is really obtained. The plant layout is shown in Figure 13. The nearly constant weights suggest that this optimization does not give the best possible controller for practical AMB suspension. However, we are not yet searching for such a controller, but a solution to the problem stated above.

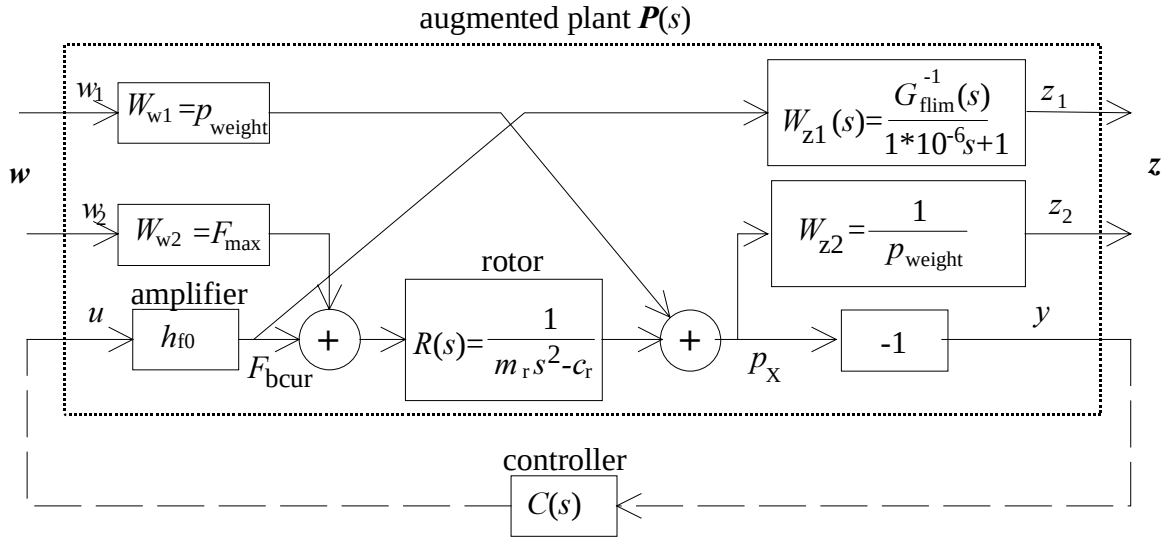

Figure 13. Plant layout for H_∞-optimization.

Let us analyze why the proposed plant layout with the chosen weights is suitable for the present analysis. Consider the situation $p_{weight}=p_{max}$. Then the disturbance w_1 represents the first force component in Equation 16, and the disturbance w_2 represents the second force component. Of course, the weight W_{w2} should be G_{flim} to be perfectly accurate. However, this approximation has only a marginal effect on the maximum force curve as can be seen from Figure 12. Also, if W_{w2} was G_{flim}, the H_∞ optimization would produce a controller with a real pole and zero near each other. This pole zero pair would have practically no effect on the frequency response of the controller and could be removed. The error signal z_1 is the weighted bearing force and the error signal z_2 is the weighted displacement. The filter in W_{z1} is inserted to make the plant proper. The time constant is so small that it has practically no effect on the results. A signal amplitude bigger than unity in z_1 or z_2 indicates power amplifier saturation or vibration which is too high, respectively. Let $F_l(\boldsymbol{P},C)$ denote the lower linear fractional transformation with parameters $\boldsymbol{P}$ and C, i.e. the transfer function from $\boldsymbol{w}$ to $\boldsymbol{z}$ in Figure 13. Now, the goal is to find such a stabilizing controller C that minimizes the largest possible amplitude of z_1 and z_2 with the requirement that amplitudes of w_1 and w_2 are smaller than 1. Thus, a stabilizing controller C that minimizes the largest induced infinity-norm of $F_l(\boldsymbol{P},C)$ over all frequencies should be found. As far as the author knows, there are no practical tools for such optimization. However, H_∞-optimization is available if the induced infinity norm is replaced by the induced 2-norm, i.e. the largest singular value. For 2×2-matrices $\boldsymbol{A}$ holds $\|\boldsymbol{A}\|_2 / \sqrt{2} \le \|\boldsymbol{A}\|_\infty \le \|\boldsymbol{A}\|_2 \sqrt{2}$. Consequently, if H_∞-optimization is used to minimize the

maximum induced 2-norm, then the smallest worst-case induced infinity-norm cannot be more than 30 % smaller. Therefore, the H_∞-optimization gives a very good approximate solution to the problem.

Next, the solution is computed for three different weights. In the first case, called the low-stiffness solution, p_{weight}=800 μm. The second case, called the medium-stiffness solution, is the actual optimum solution to the stated problem. In this case $p_{\text{weight}}=p_{\max}$=200 μm. The third one, called the high-stiffness solution, is computed with p_{weight}=50 μm. In the H_∞-optimization, a stabilizing controller C that minimizes $\left\|F_l(\boldsymbol{P},C)\right\|_\infty$ is sought where "∞" means the system infinity norm. Commercial software (Balas *et al*. 1993) that uses the solution method from Doyle *et al*. (1989) was used to calculate the solution. When the minimum is obtained within 0.01 tolerance, the corresponding central controller is accepted as a suboptimal solution.

The optimal controllers have some poles and zeros very far away from the origin that have practically no effect on the interesting frequency range. When these high frequency poles and zeros are removed, the controllers can be written as

$$
\begin{aligned}
C_{\text{opt1}}(s) &= \frac{(2\pi 200)^2}{s^2 + 2*0.85*(2\pi 200)s + (2\pi 200)^2}(9900 + 32s)\,, \\
C_{\text{opt2}}(s) &= \frac{(2\pi 257)^2}{s^2 + 2*0.79*(2\pi 257)s + (2\pi 257)^2}(14000 + 42s)\,, \\
C_{\text{opt3}}(s) &= \frac{(2\pi 398)^2}{s^2 + 2*0.75*(2\pi 398)s + (2\pi 398)^2}(31000 + 68s)
\end{aligned}
\qquad (17)
$$

and the obtained H_∞-norms were 7.84, 4.35 and 4.22, respectively. Thus, the optimal controller is a PD-controller with a second-order low-pass filter and the tolerated disturbance at the worst frequency is about 25 % of the physical limit. The Bode diagram of these controllers and the open loop is shown in Figure 14.

The open-loop Bode diagram shows the reason why the physical performance limit is unachievable. The gray areas are the low- and high-frequency demands for the open loop to achieve the physical performance limit. At low frequency the gain of the amplifier and controller should be higher than $F_{\max}/p_{\max}$. Thus, the open loop gain should be larger than

$|R(j\omega)F_{max}/p_{max}|$. At high frequencies the bearing has practically no effect on the rotor vibration and the gain of the amplifier and controller should be less than $|G_{flim}(j\omega)/p_{max}|$ in order to prevent amplifier saturation. Thus, the open-loop gain should be less than $|R(j\omega)G_{flim}(j\omega)/p_{max}|$. From Figure 14 it can be seen that the open-loop gain should drop about 40 dB in a frequency range of one decade, around the gain cross-over frequency. This is known to be impossible by the relations between the phase and amplitude of an analytic function; see Appendix B and textbooks by Doyle *et al*. (1992), Maciejowski (1989) and Skogestad and Postlethwaite (1996).

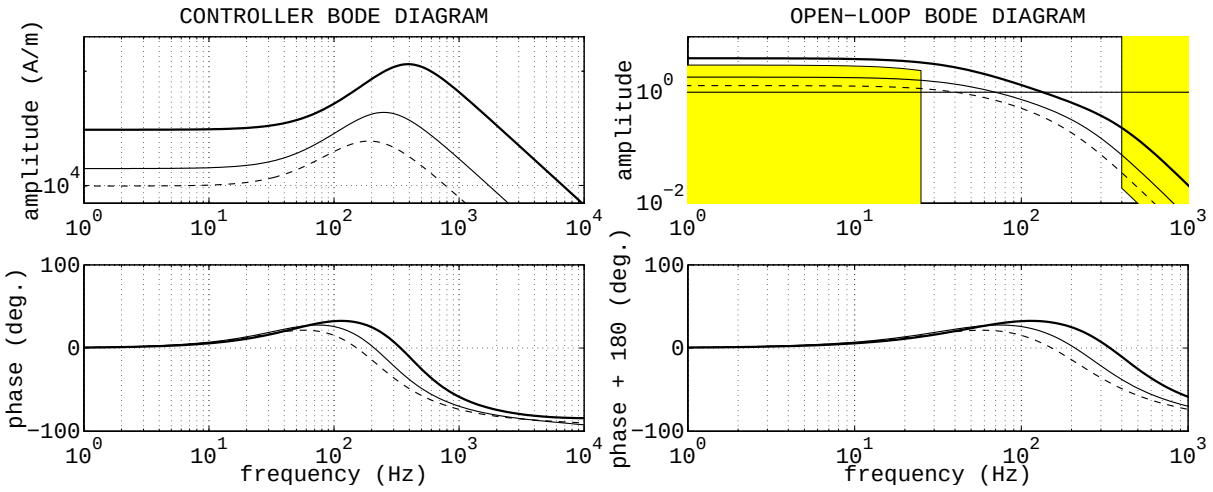

Figure 14. The Bode diagram of the optimal controllers on the left-hand side and the Bode diagram of the open loop on the right-hand side. The low-stiffness solution is drawn by the dashed thin line, medium-stiffness solution by the thin line and high-stiffness solution by the bold line.

Another observation is that the gain cross-over frequency is in all three optimal controllers near the corresponding position bandwidth, i.e. the position bandwidth computed with $p_{max}=p_{weight}$. Below the position bandwidth, the bearing force is the dominant part of the tolerated force; see Figure 12. So, at these frequencies the controller gain should be high in order to avoid contact with the retainer bearings. Above the position bandwidth, the inertial force dominates. This means that the bearing force cannot considerably increase the tolerated disturbance force. The control strategy at these frequencies is to keep the controller gain as small as possible to avoid amplifier saturation. Therefore, the gain cross-over frequency occurs naturally near the position bandwidth.

The third observation is that the phase margin is only 30°. This is quite small compared to traditional design preferences used in servo systems. This is because of the tight demand of

the loop gain roll off. If the force bandwidth were higher, the loop gain could decrease more slowly and the phase margin would increase.

In Figure 15 the open-loop Nyquist diagram and the maximum tolerated disturbance forces are shown for the three designs. The maximum tolerated force is the smaller of the disturbance forces which cause maximum bearing force or maximum allowed vibration. The darkened regions in the Nyquist diagram are drawn to help the manual tuning and are explained later. In Figure 15 these regions are drawn as a reference to show where the Nyquist curve goes in the optimal controllers.

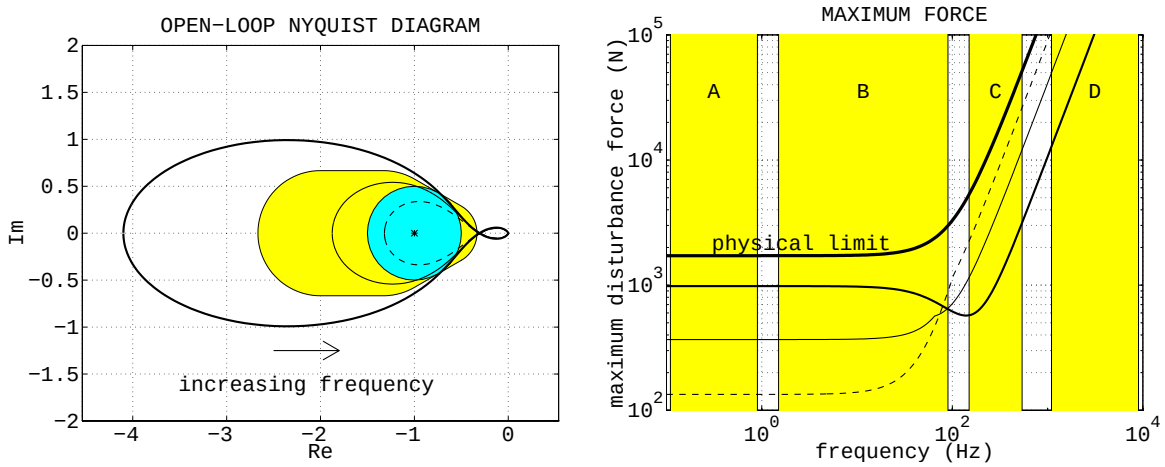

Figure 15. The open-loop Nyquist diagram and the achieved maximum tolerated disturbance force.

It is obvious that there is an inherent trade-off to be made between low and high frequencies. With one controller we cannot achieve the physical performance limits at low and high frequencies at the same time. Actually, there exists a kind of waterbed effect, i.e. if the maximum force is increased at low frequencies, it is decreased at high frequencies and vice versa. In high-speed machines there are considerable forces at low frequencies (frequency range B in Figure 15) such as aerodynamic forces caused by compressor surge and electric motor forces. Thus, the low-stiffness approach is out of the question. To achieve a load capacity which is high enough at low frequencies, the high-stiffness solution “3” is most suitable.

The consequence of such a choice is that the bearing does not tolerate the maximum force in the frequency range C, where the rotor unbalance is the biggest problem. This means that the power amplifier is saturated at a clearly smaller vibration amplitude than 200 μm. Fortunately,

the unbalance force is a highly structured disturbance acting exactly at the rotational frequency. Therefore, it is possible to increase the tolerated force in a narrow frequency band near the rotational frequency with a special unbalance compensation; see Chapter 4.

Stiffness that is too high is not a good solution either, because there exist disturbances other than the unbalance force in the frequency ranges C and D. There are, for example, higher harmonics in the position signals, measurement noise and unmodeled structural dynamics, all of which may cause problems if the controller gain is too high.

Manual design of a practical controller

The purpose of the previous optimization was to find a controller that minimizes the deviation from the achievable tolerated force at the worst frequency. Therefore, it is clear that the obtained controller is not the best possible in a wider sense. Actually, the preceding controller lack some important properties. First of all, the controller is only of the PD-type, which means that under static load the rotor moves. This is not acceptable because the small clearances will decrease in some direction. This problem is solved by inserting an integrator into the controller. Secondly, at high frequencies the controller gain should drop faster. This is achieved by introducing a finite current feedback coefficient and an additional filter into the derivator. The third problem is the robustness. The low-stiffness and medium-stiffness solutions do not tolerate the current stiffness decrease to half of the nominal value. The high-stiffness controller tolerates the drop, but when the current stiffness is increased by 50 %, which is the postulated uncertainty, the behavior becomes bad. The mentioned drawbacks are due to the optimization layout and used weights. The demands of high frequency rolloff, robustness and high static stiffness could be fulfilled by shaping the weights as a function of frequency. However, in the present problem a good controller can be easily obtained by manually tuning the parameters of a predefined controller structure.

Next, a controller that corrects the listed drawbacks is constructed by hand tuning. This is done by stating a low-order controller structure and manually tuning the parameters of this controller. Good initial values are obtained from the optimal design 3. The manual iteration is done using the Nyquist diagram. For this purpose, forbidden regions are drawn in the Nyquist diagram. The darkest region is centered at -1 and its radius is 0.5. Inside this region the sensitivity function for the nominal plant becomes larger than 2. The larger gray region is

constructed as a convex hull, i.e. the smallest convex region, containing the following three circles. First, we demand that the sensitivity function is less than 2 even if the loop gain is increased by 50 %. Thus, the nominal Nyquist curve should go outside a circle centered at -2/3 and radius 1/3. Secondly, we demand that the complementary sensitivity function for the nominal plant remains below 2. So, the Nyquist curve should go outside a circle centered at -4/3 and radius 2/3. The third circle is obtained by moving the second circle centered into -2. The construction of this "forbidden" region is slightly arbitrary. However, it is based on practical experience and the shape of the open loop with optimal controllers with the additional demand of robustness. Thus, it is well established. A suitable practical controller was done by the trial and error method using the Nyquist diagram and the result is

$$C_{\text{practical}}(s) = \frac{(2\pi 600)^2}{s^2 + 2*0.4*(2\pi 600)s + (2\pi 600)^2} * \left(25000\left(1+\frac{1}{0.15s}\right)+\frac{45s}{0.0001s+1}\right)\left(\frac{1}{0.00021s+1}\right), \tag{18}$$

where the last part represents the current control loop time constant (k_{cf}=200 V/A), which is not actually a part of the position controller. Even though the controller has seven parameters, the tuning of these parameters is straightforward. First, the current feedback coefficient is chosen so that the bandwidth of the current control loop is about 7 times the position bandwidth. Secondly, the proportional gain (25000) is determined so that the Nyquist curve crosses the real axis before the forbidden region at low frequencies. The integration time is chosen as small as possible so that the Nyquist-curve does not come considerably closer to the forbidden region than without the integrator (0.15 s is generally a good value). The derivator gain (45), the time constant (0.0001 s), the low pass filter pole radius (600 Hz) and the damping coefficient (0.4) are tuned so that the Nyquist curve goes near the border of the forbidden region and the high frequency gain drops as fast as possible. The effect of these parameters to the Nyquist curve is learned by short training. The controller Bode diagram and the open-loop Nyquist diagram are shown in Figure 16.

As can be seen in Figure 16, with the practical controller the system tolerates loop gain increase by 50 % and still the performance remains good. The only disadvantage is the amplitude peak, which decreases the tolerated disturbance force near 600 Hz.

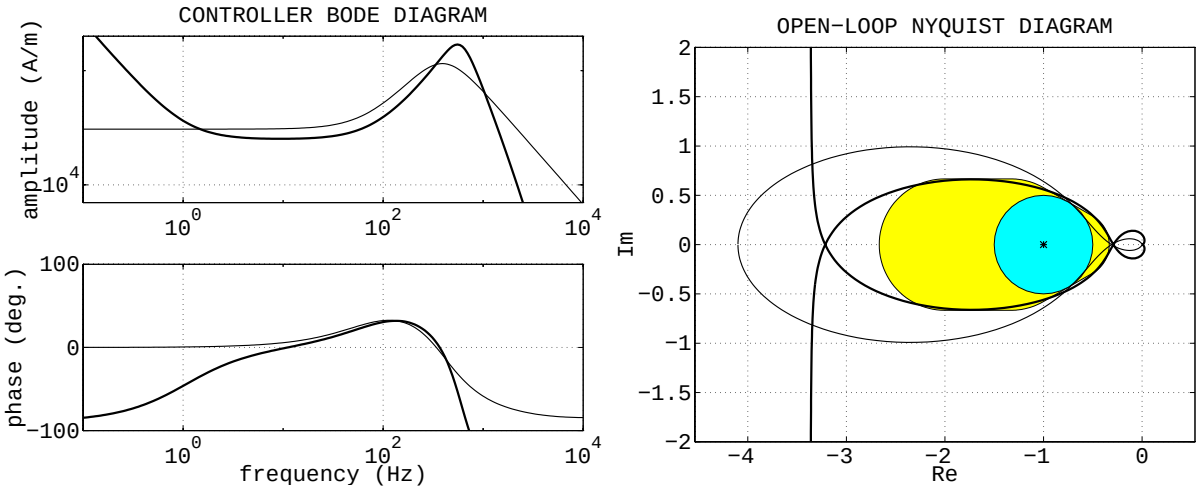

Figure 16. The Bode diagram of the practical controller (bold line) and the optimal controller "3" (thin line) on the left-hand side. The open-loop Nyquist diagram on the right-hand side.

Handling the bending modes

So far the rotor has been assumed to be rigid. Next, let us study how the first bending mode changes the situation. The SISO model with the first bending mode included is

$$R(s) = \frac{1}{m_{\mathrm{r}} s^2 - c_r} + \frac{v_3}{m_3 s^2 + d_3 s + k_3}, \tag{19}$$

where m_3=3.84, d_3=63 and k_3=64.5*10^6 are the third modal mass, damping and stiffness,

$v_3 = \boldsymbol{B}_{\mathrm{b3,2}} \boldsymbol{C}_{\mathrm{S2,3}}$=0.1 is the third modal influence factor, at the 2-end.

The computing of these parameters is considered in Section 3.4. Often, in the case of high-speed rotors, only the first bending mode is needed in the controller synthesis. However, the stability of the higher bending modes should be analyzed after synthesis. The rotor frequency response is shown in Figure 17. As is seen, there is a very high peak at the rotor response at the bending eigenfrequency (652 Hz). The height of this peak is determined by the rotor material damping, which is typically of the order of 0.002. All the previously introduced rigid-body controllers lead to an unstable closed loop. The problem is that the controller phase is between 0 and -180° at the first bending eigenfrequency. The phase should be between 0 and +180° to achieve a stable bending mode.

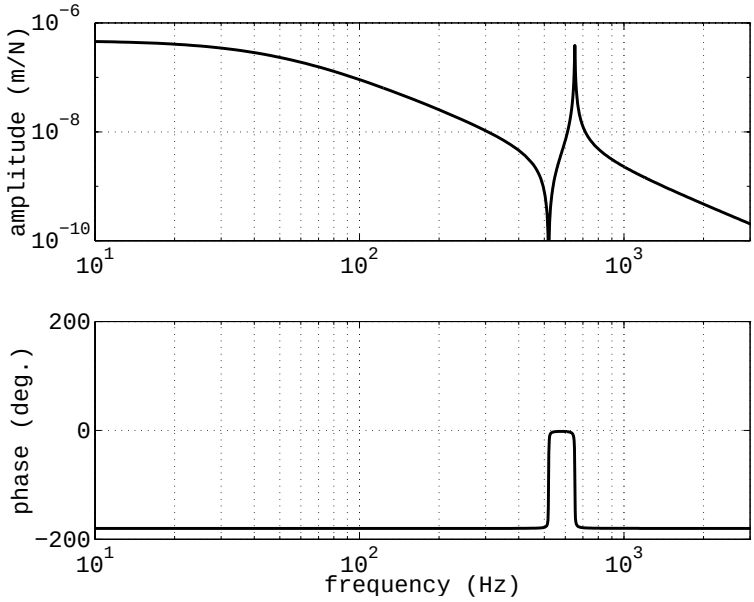

Figure 17. Bode diagram of the elastic rotor. The first bending eigenfrequency is 652 Hz.

Let us correct the phase using four straightforward strategies, which can be found in the literature. A: Modify the practical rigid-body controller so that the phase drops below -180°. B: A complex pole zero pair is inserted into the rigid-body controller to achieve a faster phase drop than with the real poles. C: Another idea is to keep the controller gain above 0° at the first bending eigenfrequency. This is done by decreasing the filtering in the practical controller. D: The phase lead is done by inserting a complex pole zero pair into the controller to achieve a sharp phase lead. These controllers are listed in Equation 20 and the frequency responses of these controllers and the original practical controller are shown in Figure 18.

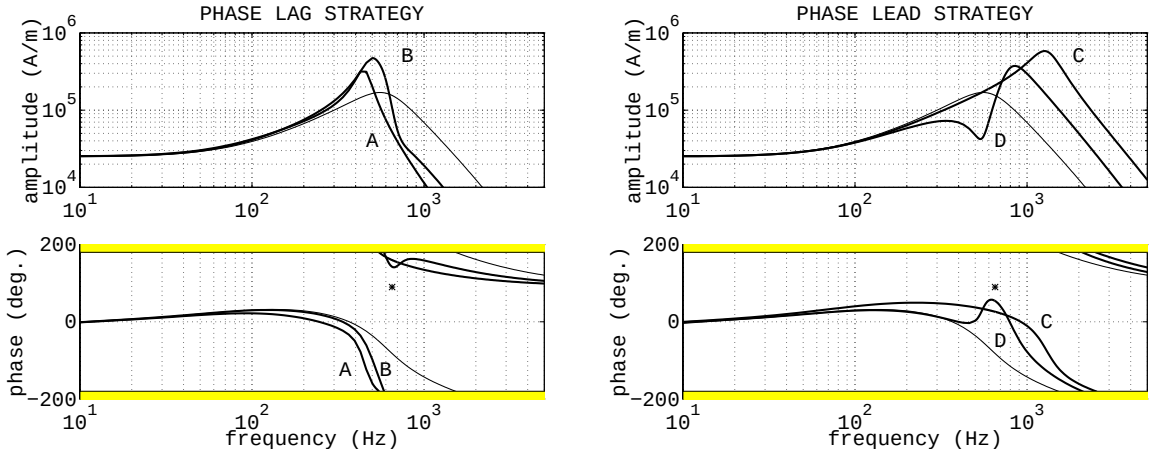

Figure 18. The frequency response of the controllers for bending mode handling. The original practical controller is drawn with a thin line.

$$
\begin{aligned}
C_{\mathrm{A}}(s) &= \frac{(2\pi 450)^2}{s^2 + 2*0.1*(2\pi 450)s + (2\pi 450)^2}\left(25000\left(1+\frac{1}{0.15s}\right)+\frac{45s}{0.0004s+1}\right)* \\
&\quad \left(\frac{1}{0.00042s+1}\right), \\
C_{\mathrm{B}}(s) &= \frac{(2\pi 500)^2}{s^2 + 2*0.15*(2\pi 500)s + (2\pi 500)^2}\left(25000\left(1+\frac{1}{0.15s}\right)+\frac{45s}{0.0002s+1}\right)* \\
&\quad \frac{s^2 + 2*0.13*(2\pi 700)s + (2\pi 700)^2}{s^2 + 2*0.13*(2\pi 600)s + (2\pi 600)^2}\left(\frac{600}{700}\right)^2\left(\frac{1}{0.00028s+1}\right), \\
C_{\mathrm{C}}(s) &= \frac{(2\pi 1300)^2}{s^2 + 2*0.2*(2\pi 1300)s + (2\pi 1300)^2}\left(25000\left(1+\frac{1}{0.15s}\right)+\frac{45s}{0.00005s+1}\right)* \\
&\quad \left(\frac{1}{0.00014s+1}\right), \\
C_{\mathrm{D}}(s) &= \frac{(2\pi 800)^2}{s^2 + 2*0.6*(2\pi 800)s + (2\pi 800)^2}\left(25000\left(1+\frac{1}{0.15s}\right)+\frac{45s}{0.0001s+1}\right)* \\
&\quad \frac{s^2 + 2*0.1*(2\pi 550)s + (2\pi 550)^2}{s^2 + 2*0.2*(2\pi 800)s + (2\pi 800)^2}\left(\frac{800}{550}\right)^2\left(\frac{1}{0.00021s+1}\right).
\end{aligned}
\tag{20}
$$

In Equation 20 the last part in every controller represents the power amplifier time constant. In Figure 18 it seems to be that all the manual designs increase the controller gain at some frequency range, i.e. the tolerated disturbance force decreases at these frequency ranges. To see whether this is inevitable to stabilize the bending mode, let us use the previously introduced optimization.

The rotor model in Figure 13 is replaced by the elastic rotor model with one bending mode. The weights are the same as previously with p_{weight}=50 μm, i.e. the high stiffness design. For synthesis purposes the bending mode is made slightly unstable, $d_3 = -2*0.002*\sqrt{m_3 k_3}$. The computed suboptimal controller is

$$
\begin{aligned}
C_{\mathrm{optb}}(s) &= \frac{(2\pi 442)^2}{s^2 + 2*0.66*(2\pi 442)s + (2\pi 442)^2}(29000 + 65s)* \\
&\quad \left(\frac{s^2 - 2*0.14*(2\pi 618)s + (2\pi 618)^2}{s^2 + 2*0.18*(2\pi 587)s + (2\pi 587)^2}\right)\left(\frac{587}{618}\right)^2.
\end{aligned}
\tag{21}
$$

The achieved H_∞-norm was 4.51, which is only marginally larger than the norm achieved with the rigid body (4.22). In Figure 19 the achieved controller and the optimum controller for a rigid body are shown.

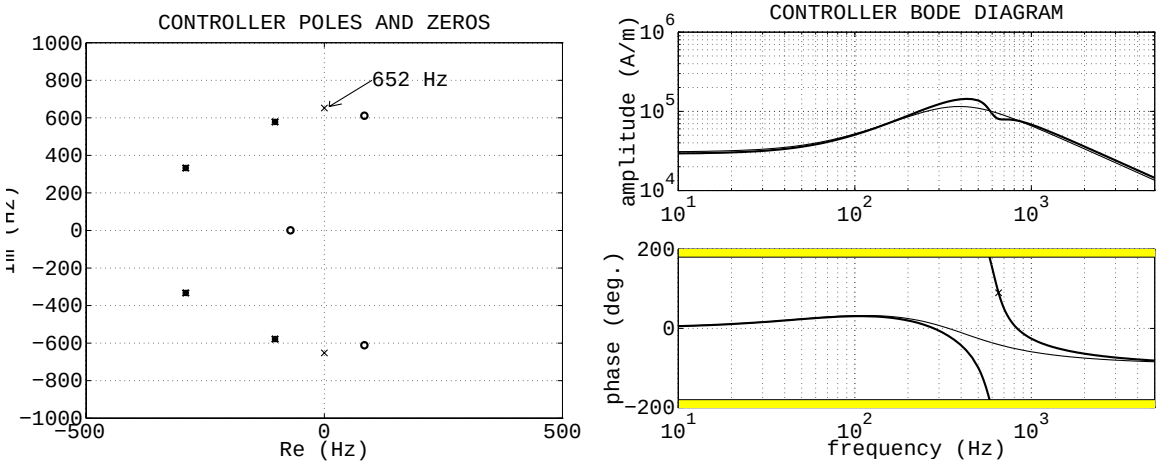

Figure 19. The pole-zero diagram of the optimal elastic rotor controller on the left-hand side. The poles are labeled with an asterisk (*) and the zeros by circles (o). On the right-hand side the Bode diagram of the optimal elastic rotor controller (bold line) and the rigid-body controller (thin line). The bending mode eigenfrequency (652 Hz) is labeled by (x) in both figures.

Thus, the optimal controller is essentially the rigid-body controller with a second order all-pass filter. Let us denote this solution E. As can be seen in Figure 19, the amplitude peaks in the controller amplitude curve vanish. A non-minimum phase controller is a small surprise at first sight. However, if the phase is modified by a minimum phase transfer function (strategies A..D), a gain increase appears inevitably: see Appendix B. The assumed damping of the bending mode affects considerably the solution near the bending mode. If the damping was assumed less negative or even slightly positive, the controller would still have zeros in the right half plane. Then, however, the zero would come very close to the imaginary axis and the frequency range in which the bearing behaves as a damper becomes impractically narrow. The damping was chosen so that the obtained controller can be considered as a practical one.

Now, there are five different strategies to handle the bending mode. Let us next study which might be the best one in different situations. If the first bending mode is at a very high frequency, solution A is clearly the best because the controller phase is correct with only small, if any, modifications to the original rigid-body controller.

If the first bending mode is very near the gain crossover frequency, then strategies A, B and E are not good. With strategies A and B the amplitude peak becomes extremely high. This is

an inevitable consequence of a fast phase drop, as seen in Appendix B. The all-pass filter solution is not acceptable either, because the complex pole and zero go near the imaginary axis, and consequently the frequency range where the controller phase is correct becomes narrow. This leads to problems with a rotating machine because of the splitting of the bending mode into the forward and backward modes. Typically, at maximum speed their eigenfrequencies are about 5 % higher and lower, respectively, than the eigenfrequency of the nonrotating rotor. Therefore, if the damping frequency band is too narrow, the forward or backward mode, or both, may become unstable at full speed.

In the present case, the first bending mode is neither far away nor close, but somewhere between these. Therefore, all the strategies A...E could be used. In the following, the properties of the different solutions are analyzed. In solution A, the necessary phase drop is obtained by two real poles and one complex pole pair. Due to the real poles, the phase drop is not so fast as it could be. This leads to the deteriorating of the rigid-body dynamics, which is clearly seen as a phase drop in the Bode diagram (Figure 18). With two complex pole pairs, strategy B, a faster phase drop is achieved and the good rigid-body dynamics and robustness are recovered. This is achieved at the expense of a higher amplitude peak in the controller at frequency 500 Hz. Thus, both strategies A and B lead to an increase in the controller gain in the normal operating speed range 400 Hz - 540 Hz. Even though we have an effective unbalance compensation algorithm, this increase is dangerous because of the pulsating electric motor force and rapid changes in the unbalance vibration, caused by fast accelerations and decelerations. A nice feature of solutions A and B is that after having once gone below -180°, the phase remains between -180° and -360°. Also, the high-frequency gain is dropped from the original value. Thus, we have no problems with the high-frequency disturbances or higher bending modes. Solutions C and D do not introduce an amplitude peak in the rotational speed range but they increase the controller gain in the high-frequency range. Because of that, we should also consider the second bending mode in the controller synthesis. Then the controller phase should be dropped below -180° in between the first and second bending modes. This, however, may be difficult as the gap between these frequencies is narrow. The high gain at high frequencies also increases the noise. One nuisance is that the bearing has negative damping at a certain frequency range after the first bending mode. This is unpleasant, because sometimes, in the maintenance or testing, the rotor is used without the compressor wheel. Then the bending mode shifts into this destabilizing frequency range and another controller is

needed to levitate the rotor without the compressor wheel. The optimal solution, solution E, does not increase the controller gain at the rotational frequency range or at high frequencies. The problem with this solution is that there also exists a negative damping frequency range after the first bending eigenfrequency.

In the present case the influence factor is positive, i.e. the bearing magnet and the position sensor are on the same side of the bending mode node. If the node is between the sensor and the magnet, the controller phase should be between 0° and -180° to keep the bending mode stable. Actually, this would be simple because the phase is there naturally.

The previous strategies for bending mode damping have already been discussed by several authors. Matsushita *et al*. (1992) have proposed a third-order low-pass filter to drop the bearing stiffness phase below -180° at the bending mode. This is strategy A. They also pointed out that the antiresonance frequency (the gain drop seen in Figure 17) can be used to compensate the amplitude peak in the low pass-filter. Also Förch *et al*. (1996) have applied the phase lag strategy to control a rotordynamic test rig. They used a complex pole-zero pair to adjust the phase more effectively, which is similar to strategy B. They also noted that the noncollocation of the sensor and actuator is not necessarily a nuisance in stabilizing the bending modes, but it can be utilized. Delprete *et al.* (1994) have tested an ordinary PID-controller, a controller with two lead compensators and a complex lead section. These methods are close to the phase-lead strategies C and D in the present publication. They also noted that these strategies lead to an increase in the high-frequency gain. As far as the author knows, a second order all-pass filter has not been proposed for bending mode damping. However, using modern synthesis methods some authors have synthesized controllers with right half plane zeros; see Carrere *et al*. (1994).

3.3 The generalized Nyquist diagram

Before going into the MIMO case, a method for analyzing these kinds of MIMO systems is described. First, the model for AMB suspension is given for robustness and performance analysis. Then, a short review of the different methods for analyzing such systems is given. Finally, the generalized Nyquist diagram is briefly described. The detailed derivations and proofs are given in the references and Appendix A.

Uncertainty model

The block diagram of the magnetic bearing suspension system for robustness analysis is shown in Figure 20. The uncertainties are collected into two matrices, $\boldsymbol{K}_{in}$ and $\boldsymbol{K}_{out}$. These are the input and output uncertain gain matrices and their nominal value is **I**. No uncertainty is assumed for the rotor. The only remarkable uncertainty, considering the rotor, is the unbalance. It can be interpreted as an external disturbance and therefore it has no effect on the stability. The finite element rotor model is very accurate and is used as a nominal model. The position stiffness, included in the rotor model, is not accurate but a well-designed system is not sensitive to its variations.

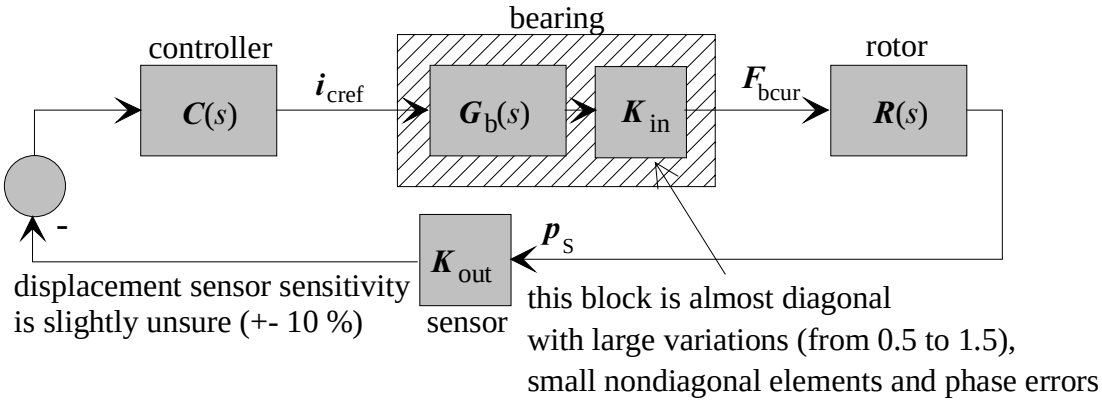

Figure 20. System layout for robustness analysis.

The displacement sensor most commonly used in our project is an inductive type sensor with excellent linearity and signal-to-noise ratio. The sensor sensitivity is practically the same in one-end X- and Y-directions, but may differ from its nominal value by 10 % because of manufacturing reasons. So, $\boldsymbol{K}_{out}$ is a diagonal uncertain gain matrix whose elements are real and in the range 0.9 .. 1.1 and $k_{1,1}=k_{3,3}$ and $k_{2,2}=k_{4,4}$.

As seen in Section 2.1, the bearing has a significant uncertainty that can be described by an almost diagonal uncertain gain matrix $\boldsymbol{K}_{in}$. Based on the FEM analysis, the diagonal elements have absolute values in the range 0.5 .. 1.5. The phase angle is about 5° at maximum (Antila 1998). The phase angle in the elements of $\boldsymbol{K}_{in}$ describes the effects of eddy currents and hysteresis in the magnetic circuit and the errors in the amplifier response due to dynamic inductance variations. Also, there are small nondiagonal elements in the locations (1,3), (3,1), (2,4) and (4,2) due to magnetic cross-connections. A deeper analysis (Antila 1998) shows that these elements remain less than 10 % of the diagonal elements in the case of NSNS pole

configuration. The other nondiagonal elements are zero, because there are no cross-connections between the bearings at the two ends of the rotor. The other blocks in Figure 20 are the following:

$$\boldsymbol{G}_{\mathrm{b}}(s) = \mathrm{diag}\{G_{\mathrm{b}}(s), G_{\mathrm{b}}(s), G_{\mathrm{b}}(s), G_{\mathrm{b}}(s)\},\ G_{\mathrm{b}}(s) = \frac{h_{\mathrm{f0}} k_{\mathrm{cf}}}{L_{\mathrm{dyn0}} s + k_{\mathrm{cf}}},$$

$$\boldsymbol{R}(s) = \begin{bmatrix} \boldsymbol{C}_{\mathrm{S}} & \boldsymbol{0} \\ \boldsymbol{0} & \boldsymbol{C}_{\mathrm{S}} \end{bmatrix} \begin{bmatrix} \boldsymbol{X}(s) & \boldsymbol{Y}(s) \\ -\boldsymbol{Y}(s) & \boldsymbol{X}(s) \end{bmatrix}^{-1} \begin{bmatrix} \boldsymbol{B}_{\mathrm{b}} & \boldsymbol{0} \\ \boldsymbol{0} & \boldsymbol{B}_{\mathrm{b}} \end{bmatrix}, \tag{22}$$

$$\boldsymbol{X}(s) = \boldsymbol{M}_{\mathrm{rot}} s^2 + \boldsymbol{D}_{\mathrm{rot}} s + \boldsymbol{K}_{\mathrm{rot}} - \boldsymbol{B}_{\mathrm{b}} c_0 \boldsymbol{B}_{\mathrm{b}}^{\mathrm{T}},\ \boldsymbol{Y}(s) = \Omega \boldsymbol{G}_{\mathrm{rot}} s + \Omega \boldsymbol{D}_{\mathrm{rot}}.$$

Methods for robustness analysis

For robustness analysis, the structured singular value (μ) is a powerful tool, originally introduced by Doyle (1982). The structured singular value is considered in many textbooks; see for example, Maciejowski (1989), Skogestad and Postlethwaite (1996) and Zhou *et al.* (1997). Using μ-analysis, very nonconservative statements can be made concerning the stability and performance robustness. In principle, there is no conservativeness and in practice the numerical upper bounds are close to the correct values. Unquestionably it is a very useful and powerful tool. Therefore, the question of why something else is needed arises.

The plot of the structured singular value as a function of frequency only tells the user whether the robust performance (or robust stability) is obtained or not. It does not give very much insight into what the problem is and how the design could be improved. Further, the singular value plot provides the robustness information only with respect to the defined modeling errors. For example, in the case of AMB there exist small phase errors and small nondiagonal elements. If these are taken into consideration in the correct way, the uncertainty model becomes complicated. For these reasons, the author has searched for a method which would be helpful in the synthesis and would provide intuitive feeling of when the design is good while remaining highly nonconservative in the stability margin predictions.

The open-loop frequency response methods have proven very useful in SISO controller design. Also for MIMO cases, similar analysis and design methods have been developed. These “classical” frequency domain methods are collected in the book of Maciejowski (1989).

Frequency domain stability analysis is based on the Generalized Nyquist criteria, see Appendix A.

The characteristic loci do not give very much information about the robustness. They only give the stability margins in the case of diagonal perturbation, with equal diagonal elements. It is difficult to predict how the characteristic loci deform when the parameters change in a more complicated way. An obvious improvement is to compute at every frequency a template for every eigenvalue by changing the unsure parameters over their ranges. In practice, it is tedious to compute these templates, especially as the borders of the templates are not generally achieved at bounding parameter values. However, in SISO systems, there is only one template at every frequency and computing this is relatively easy. In Quantitative Feedback Theory these templates are used in the synthesis of feedback systems, see Horowitz (1982) and the references there.

If the system is diagonally dominant and the perturbation is diagonal, a Nyquist array with Gerschgorin bands may be useful. There is also a method for finding a diagonal scaling matrix that gives optimally thin Gerschgorin bands (Mees 1981). Some AMB systems are diagonally dominant with very small nondiagonal elements. In this case, the Nyquist array with Gershgorin bands is useful, giving nonconservative results. However, generally the nondiagonal elements are not very small and they cannot be made small by diagonal scaling. It seems to be that in a well-designed AMB system the open loop is not generally diagonal near the cross-over frequency, but it is near normal (matrix $\boldsymbol{X}$ is called normal if $\boldsymbol{X}^{\mathrm{H}}\boldsymbol{X}=\boldsymbol{X}\boldsymbol{X}^{\mathrm{H}}$).

Postlethwaite *et al*. (1981) have introduced a “small-phase” condition to be used with the traditional small-gain condition to decrease conservativeness. This method is further improved by Kouvaritakis and Postlethwaite (1982). Unfortunately, in the case of AMB the uncertainty is so large in the plant input that often the small-phase condition becomes useless and the stability margin predictions reduce to the small-gain condition.

Applying the numerical range to further decrease the conservativeness of stability margin estimates has been proposed by Owens (1984,1986). He derives a robust stability condition and shows that it can be significantly less conservative than the combined small-phase small-gain condition. Later Palazoglu and Khambanonda (1989) have applied the method in the IMC (internal model control) framework. Collado and Rojas (1992) have derived robust stability condition, based on the numerical range, for state-space models with parametric uncertainty.

The numerical range approach has been adopted in this publication because in the case of AMB it gives highly nonconservative estimates. This is because the AMB system will be near normal at the gain and phase crossover frequencies. Also, the numerical range of the open loop frequency response matrix has certain relationships with the closed loop singular values. This makes it suitable for performance analysis as well.

The proposed generalized Nyquist diagram

Basically, the proposed method differs from that of Owens (1984) only so that a direct Nyquist diagram is used instead of an inverse Nyquist diagram. Thus, the derived robust stability condition is essentially the same. In the present publication the numerical range method is extended to include input and output uncertainties and a structured Nyquist diagram is introduced to minimize the conservativeness of this method. Also, the interesting relationships between the numerical range and the closed loop singular values are noted.

The stability of the closed loop, shown in Figure 20, is determined by the eigenvalues of the open-loop frequency response matrix. The open-loop eigenvalues are achieved from the following eigenvalue problem

$$\boldsymbol{K}_{\text{in}}\boldsymbol{L}_0\boldsymbol{v}_n = \lambda_n\boldsymbol{v}_n \ , \tag{23}$$

where λ_n is an eigenvalue,

$\boldsymbol{v}_n$ is the corresponding eigenvector and

$\boldsymbol{L}_0 = \boldsymbol{G}_{\text{b}}\boldsymbol{C}\boldsymbol{R}$ is the nominal open-loop frequency response matrix.

At this point the output uncertainty is not taken into consideration, i.e. $\boldsymbol{K}_{\text{out}}=\mathbf{I}$.

The problem is not to decide whether the nominal plant is stable. Actually, frequency response methods are not handy for such an analysis, but the nominal stability is easier to check using a state space realization. The more interesting question is, does the system remain stable when the matrix $\boldsymbol{K}_{\text{in}}$ achieves all allowed values. Or to reverse the question, how much can $\boldsymbol{K}_{\text{in}}$ deviate from the nominal value $\mathbf{I}$ without endangering stability. In SISO-systems these questions can be readily answered using frequency domain plots like the Nyquist diagram, the Bode diagram and the Nichols chart. The problem with multivariable plants is that the

behaviour of the open-loop eigenvalues is difficult to predict when the uncertain matrix $\boldsymbol{K}_{\text{in}}$ varies. Let us modify the eigenvalue equation as follows

$$\begin{aligned}
& \boldsymbol{K}_{\text{in}}\boldsymbol{L}_0\boldsymbol{v}_n = \lambda_n\boldsymbol{v}_n && \left|\text{multiply from left by } \boldsymbol{K}_{\text{in}}^{-1}\right. \\
\Leftrightarrow \quad & \boldsymbol{L}_0\boldsymbol{v}_n = \lambda_n\boldsymbol{K}_{\text{in}}^{-1}\boldsymbol{v}_n && \left|\text{multiply from left by } \boldsymbol{v}_n^{\text{H}}\right. \\
\Rightarrow \quad & \boldsymbol{v}_n^{\text{H}}\boldsymbol{L}_0\boldsymbol{v}_n = \lambda_n\boldsymbol{v}_n^{\text{H}}\boldsymbol{K}_{\text{in}}^{-1}\boldsymbol{v}_n && \left|\text{divide by } \boldsymbol{v}_n^{\text{H}}\boldsymbol{K}_{\text{in}}^{-1}\boldsymbol{v}_n\right. \\
\Leftrightarrow \quad & \lambda_n = \frac{\boldsymbol{v}_n^{\text{H}}\boldsymbol{L}_0\boldsymbol{v}_n}{\boldsymbol{v}_n^{\text{H}}\boldsymbol{K}_{\text{in}}^{-1}\boldsymbol{v}_n}, &&
\end{aligned} \tag{24}$$

where $\boldsymbol{K}_{\text{in}}$ is assumed invertible and $\boldsymbol{x}^{\text{H}}\boldsymbol{K}_{\text{in}}^{-1}\boldsymbol{x} \neq 0$ for all nonzero $\boldsymbol{x}$. So, when the eigenvector is known, the corresponding eigenvalue can be expressed as a product of two scalars. The problem is that the eigenvector also changes as the matrix $\boldsymbol{K}_{\text{in}}$ changes. Thus, Equation 24 does not provide accurate predictions of the eigenvalues of the disturbed open-loop frequency response matrix. The main idea is to allow vector $\boldsymbol{v}_{\text{n}}$ to be any nonzero vector, not only an eigenvector. Then we can say that

$$\begin{aligned}
\lambda_n &\in \left\{ \frac{a}{b} \;\middle|\; a \in \varphi(\boldsymbol{L}_0),\, b \in \phi(\boldsymbol{K}_{\text{in}}) \right\}, \\
\varphi(\boldsymbol{L}_0) &= \left\{ \boldsymbol{x}^{\text{H}}\boldsymbol{L}_0\boldsymbol{x} \;\middle|\; \boldsymbol{x} \in \boldsymbol{C}^{\text{N}\times 1}, \boldsymbol{x}^{\text{H}}\boldsymbol{x} = 1 \right\}, \\
\phi(\boldsymbol{K}_{\text{in}}) &= \cup\varphi\left(\boldsymbol{K}_{\text{in}}^{-1}\right),\ \boldsymbol{K}_{\text{in}} \in \{\text{"allowed variations"}\},
\end{aligned} \tag{25}$$

where $\varphi(\boldsymbol{L}_0)$ is a set in a complex plane, called the numerical range of $\boldsymbol{L}_0$ (also called the field of values in the literature) and $\phi(\boldsymbol{K}_{\text{in}})$ is called the uncertainty region of $\boldsymbol{K}_{\text{in}}$.

It can be shown that $\varphi(\boldsymbol{L}_0)$ is convex, i.e. if complex numbers *c* and *d* belong to $\varphi(\boldsymbol{L}_0)$, then all the complex numbers in the line segment [*c,d*] belong to $\varphi(\boldsymbol{L}_0)$. Another remarkable property is that in the case of normal $\boldsymbol{L}_0$ the numerical range is a polygon where the outermost eigenvalues of $\boldsymbol{L}_0$ are at the corners. Proofs of these properties, a method to compute $\varphi(\boldsymbol{L}_0)$ and many other properties are found in the book of Horn and Johnson (1991).

The generalized Nyquist diagram is simply a plot of $\varphi\left[\boldsymbol{L}_0(j\omega)\right]$ at a sufficient number of frequency points. Note that this generalization is computed for the nominal open-loop frequency response matrix, as in the case of SISO-Nyquist-diagram.

Because the matrix $\boldsymbol{L}_0$ is not necessarily normal, the question arises: is it possible to find a similarity transformation $\mathbf{D}$ that would make it more normal? It is easy to see that $\rho[\boldsymbol{K}\boldsymbol{L}_0] = \rho\left[\left(\mathbf{D}\,\boldsymbol{K}\,\mathbf{D}^{-1}\right)\left(\mathbf{D}\,\boldsymbol{L}_0\,\mathbf{D}^{-1}\right)\right]$ where $\rho[\boldsymbol{A}]$ means the set of the eigenvalues of $\boldsymbol{A}$. Let us introduce a "structured" numerical range as follows

$$\varphi_{\mathrm{S}}\left(\boldsymbol{L}_0\right) = \cap\varphi\left(\mathbf{D}\,\boldsymbol{L}_0\,\mathbf{D}^{-1}\right), \mathbf{D} \in \text{"allowed scalings"}, \tag{26}$$

where "allowed scalings" is a set of invertible matrices that commutes with all allowed $\boldsymbol{K}$:s, i.e. $\boldsymbol{K}\mathbf{D}=\mathbf{D}\boldsymbol{K}$, or $\boldsymbol{K} = \mathbf{D}\,\boldsymbol{K}\,\mathbf{D}^{-1}$. In the generalized Nyquist diagram the numerical range can be replaced by this structured numerical range if the conservativeness should be minimized.

For the postulated uncertainties, the uncertainty region $\phi\left(\boldsymbol{K}_{\mathrm{in}}\right)$ is a thin sector in the complex plane, shown in Figure 21.

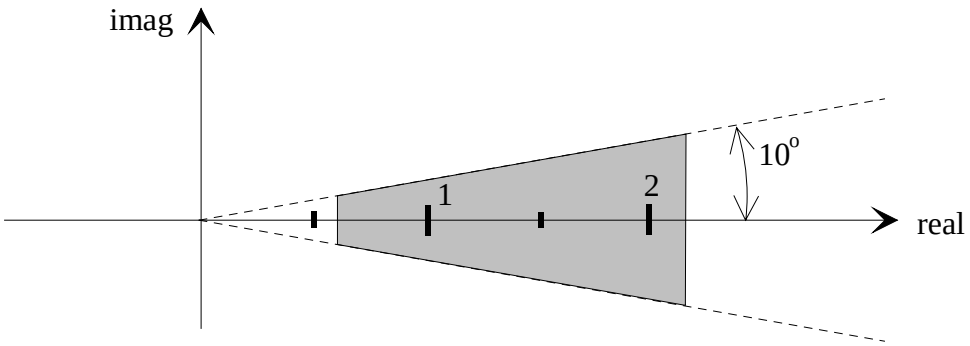

Figure 21. The approximate shape of the uncertainty region $\phi\left(\boldsymbol{K}_{\mathrm{in}}\right)$, see also Appendix A.

The shape of the uncertainty region is derived in Appendix A. However, let us mention here that the small nondiagonal elements in $\boldsymbol{K}_{\mathrm{in}}$ manifest themselves as a wider sector in the uncertainty region, i.e. they mean phase angle. In the case of AMB, this phase angle has a clear physical meaning. Certain kinds of cross-connections introduce spatial phase angle between the rotating reference current vector and the resulting rotating force vector.

Robust stability can be determined from the generalized Nyquist diagram by straightforward visual observation. If the numerical ranges do not penetrate inside the forbidden region $-\phi(\boldsymbol{K}_{\text{in}})$ then robust stability is achieved.

As in the SISO-case, the generalized diagram also offers information about how the design could be improved. In Appendix A, it is shown that the numerical range of the open loop frequency response matrix has certain relationships with the singular values of the sensitivity function and the complementary sensitivity function. This means that the generalized Nyquist diagram also provides information about the nominal performance. Furthermore, the robust performance in the middle point of the uncertain gain matrix can be determined in the case of real diagonal uncertainty. The structured numerical range does not have these interesting relationships and computing the structured version is considerably harder. For these reasons the unstructured version is preferred.

The small output uncertainty is taken into consideration by computing the union of the numerical ranges of $\boldsymbol{L}_0 = \boldsymbol{C}\boldsymbol{K}_{\text{out}}\boldsymbol{R}\boldsymbol{G}_{\text{b}}$ for all possible matrices $\boldsymbol{K}_{\text{out}}$. However, this is difficult to compute and is therefore approximated by the convex hull of it, i.e. the smallest convex set containing the mentioned union.

This method is especially useful when the nominal open loop is near normal, or can be made normal by scaling (Equation 26). As noted, for a normal matrix the numerical range is a polygon and the eigenvalues are at the polygon's corners. This means that some of the characteristic loci are likely to travel along, or very near, the boundary of the numerical range band (the union of the numerical ranges drawn for all frequencies). This does not hold generally, but in practice, at least in the case of AMB suspension, this is the case. This fact and the uncertainty structure defined for $\boldsymbol{K}_{\text{in}}$ leads to stability margin predictions with practically no conservativeness. In Section 3.4 a well-designed AMB system is shown to be near normal.

3.4 The MIMO case

In this section the true multivariable magnetic suspension is considered. The main emphasis is on the control of rigid-body dynamics. The bending modes are not, however, forgotten. First, the decentralized control scheme is briefly analyzed. Then, a controller that optimizes the

worst frequency behaviour with respect to the stated physical performance limits is constructed. The structure of this optimal controller is studied, and based on this study a synthesis method is proposed and applied to the test machine. At the end, the design is analyzed using the generalized Nyquist diagram.

Decentralized control

Let us first analyze the already-designed decentralized controller. Controller B, designed in Section 3.2, is used in every channel because the machine is very symmetric. The generalized Nyquist diagram for nonrotating machine is shown in Figure 22. In the analysis, a 10 % error is assumed in the position sensor sensitivity. The Nyquist diagram is drawn only for positive frequencies up to 500 Hz, and the unstructured version is used.

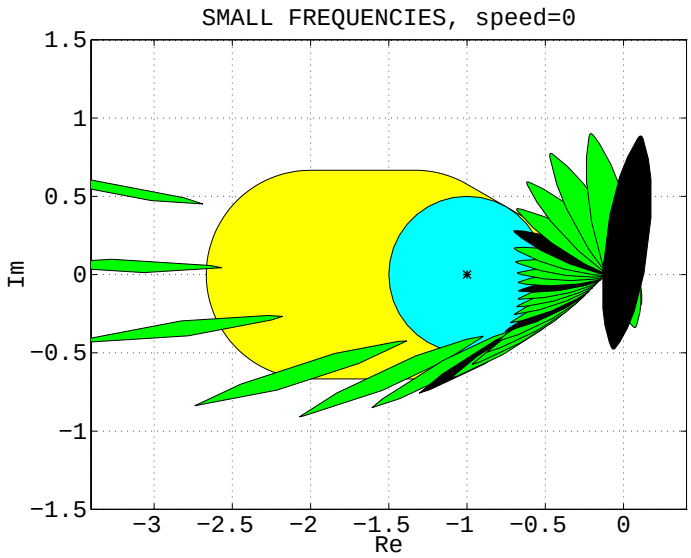

Figure 22. The generalized Nyquist diagram for decentralized control. The numerical ranges are drawn for frequencies 5, 10, 20, 40, 60, ..., 500 Hz. The even hundreds are filled with black.

The Nyquist diagram reveals that the design is useless. The system is stable but the numerical ranges go very close to the critical -1 point. It can be predicted that the system tolerates gain drop by a factor of 1/2.5 but increase only by a factor of 1/0.7. These are only the stability margins; the system behavior becomes unacceptably bad at smaller variations. The nominal

system is already quite poor. The problem arises because the plant is not diagonal and neglecting the cross-connections in the controller design does not lead to good results.

The previous design can be improved using the generalized Nyquist diagram. The phase-lead frequency range can be widened so that the numerical ranges go around the forbidden region. If only the rigid body modes were taken into consideration, an acceptable design could be obtained by decentralized controller. The biggest disadvantage would be unnecessarily high controller gain at high frequencies. However, the first bending mode makes the situation difficult. The phase lead frequency range will go to such a high frequency that the phase lag strategies (A and B in Section 3.2) cannot be used for bending mode damping. Therefore, phase lead strategy (C or D) must be used. These strategies further increase the high frequency gain, which leads to noisy bearing and problems with high frequency disturbances and damping of the higher bending modes. The main problem with decentralized control is that we have only one parameter, one controller, to modify the characteristic loci, i.e. to control the shape and location of the numerical range.

In the previous discussion, a similar controller was used at the two rotor ends, due to the symmetry of the machine. However, it is not so clear that an optimal decentralized controller has similar characteristics at both rotor ends even though the machine would be perfectly symmetric. This question is not analyzed further. Instead, let us relax the limitation of decentralized control and analyze the achievable performance with respect to the physical performance limits.

Worst-frequency optimal controller for rigid rotor

To find out what an acceptable control system looks like, H_∞-optimization is again used with the plant layout shown in Figure 13. Let us consider the suspension of a nonrotating rigid rotor in one plane. The rotor model is now

$$\boldsymbol{R}(s) = \boldsymbol{C}_{\mathrm{S2}}\left(\boldsymbol{M}_{\mathrm{rot2}}s^2 - \boldsymbol{B}_{\mathrm{b2}}^{\mathrm{T}}c_0\boldsymbol{B}_{\mathrm{b2}}\right)^{-1}\boldsymbol{B}_{\mathrm{b2}}\ , \tag{27}$$

where the matrices are the rotor dynamic matrices with only the rigid-body modes included (see Appendix C). The scalar weights and the amplifier block are replaced by diagonal 2×2 matrices where the diagonal elements are the scalar weights in Figure 13.

Let us study what the physical performance limits are in the rigid rotor case and why the proposed plant layout is still valid in the search for these limits. Assume that there are two disturbance forces acting on the rotor exactly at the bearing locations. This is no restriction because any force combination can be reduced to two forces acting on the bearing locations. These disturbance forces are collected into vector $\boldsymbol{F}_{\mathrm{d}}$. The controlled bearing forces are collected into vector $\boldsymbol{F}_{\mathrm{bcur}}$. The position measurements are collected into vector $\boldsymbol{p}_{\mathrm{S}}$. Again, we search for the maximum disturbance force combination that the suspension system tolerates without too high a vibration amplitude and actuator saturation. The disturbance force can be written as a function of the vibration and bearing force as follows

$$\boldsymbol{F}_{\mathrm{d}} = \boldsymbol{R}^{-1}(j\omega)\boldsymbol{p}_{\mathrm{S}} - \boldsymbol{F}_{\mathrm{bcur}}. \tag{28}$$

Physically, the suspension system might tolerate any disturbance force combination which is achieved from Equation 28, when the absolute values of the elements of $\boldsymbol{F}_{\mathrm{bcur}}$ remain below $\left|G_{\mathrm{flim}}(j\omega)\right|$ and the absolute values of the elements of $\boldsymbol{p}_{\mathrm{S}}$ remain below $p_{\max}$. All such disturbance force combinations are described by disturbance vectors $\boldsymbol{w}$ for which $\|\boldsymbol{w}\|_\infty \le 1$ (Figure 13). Again, $\boldsymbol{G}_{\mathrm{flim}}$ is replaced by $\boldsymbol{F}_{\max}$ in the weight $\boldsymbol{W}_{\mathrm{w2}}$, because this simplifies the achieved solution and has practically no effect on the result. The suspension system can be said to tolerate the disturbance combination if $\|\boldsymbol{z}\|_\infty \le 1$, i.e. all forces remain below the dynamic force limit and all displacement remain below $p_{\max}$. As in the SISO case, we should find a stabilizing controller $\boldsymbol{C}$ that minimizes the largest induced matrix infinity-norm of $F_l(\boldsymbol{P},\boldsymbol{C})$ over all frequencies. Again, the matrix infinity norm is replaced by the largest singular value (induced 2-norm) to make the problem suitable for H_∞-optimization. For 4×4 matrix $\boldsymbol{A}$ holds $\|\boldsymbol{A}\|_2 / 2 \le \|\boldsymbol{A}\|_\infty \le 2\|\boldsymbol{A}\|_2$. So, H_∞-optimization is still a reasonable approach.

In this analysis we require that the vibration amplitudes remain below a certain limit at the sensor locations. In some applications, these are not the most important locations, but the vibration amplitude should be limited rather in some other place of the rotor. However, in the high-speed machines, the retainer bearings are usually near the position sensors and the retainer bearings have the smallest clearances. Therefore, the position sensor locations can be considered as important locations. In the following, the position weight is p_{weight}=50 μm.

To get a more general view, let us compute the solution for two different rigid-body models. The first is the model of the test machine. The second is a fictitious machine that otherwise has the same parameters as the test machine, but the 1-end electromagnet is moved into the mass center of the rotor, i.e. the element (2,1) in the matrix $\boldsymbol{B}_{b2}$ is zero.

The solutions were computed using commercial software as in the case of point mass levitation. In Figure 23 the amplitude curves of the elements of the controllers are shown. The generalized Nyquist diagrams are also shown in Figure 23. The diagrams are unstructured versions and computed with zero position sensor error to find out the true nature of the solution. Even though the Nyquist diagrams are computed at the plant input, they look essentially the same at the plant output.

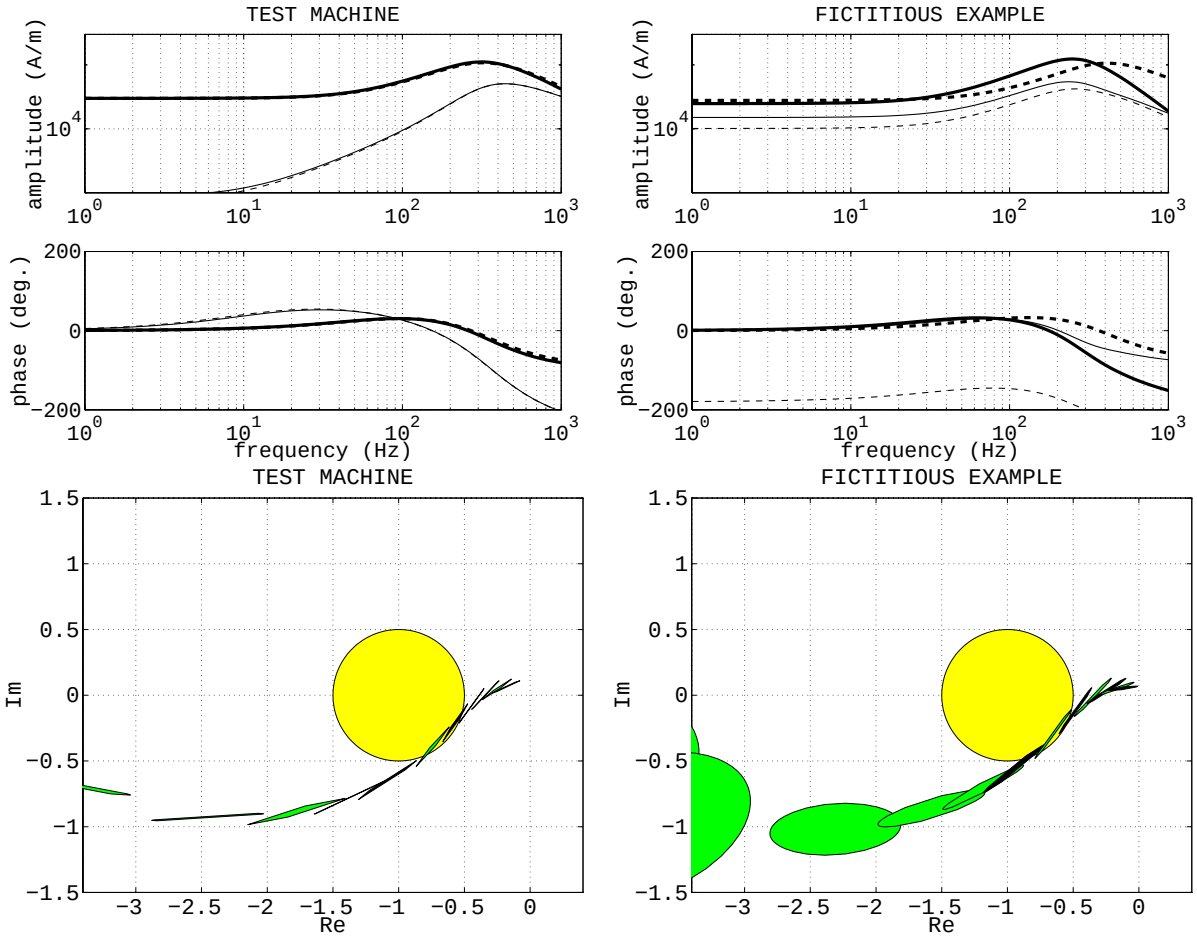

Figure 23. The Bode diagrams of the optimal controllers and the generalized Nyquist diagrams of the open loops at the plant input. The controller elements are (1,1) bold line, (1,2) thin line, (2,1) thin dashed line and (2,2) bold dashed line. The frequencies are 5, 10, 20, 40, 60, 80, 100, 150, 200, 250, 300, 350 and 400 Hz. Even hundreds are filled with black.

As can be seen, the controllers are not decentralized (the off-diagonal elements are not zero). Further, the open-loop frequency response matrix is not diagonal at either the plant input or at the plant output in neither case (this cannot be seen from Figure 23).

So, what general properties do the optimal solutions have? The first observation is that the numerical ranges do not point to the origin, but in the vicinity of -1 point they turn in order to keep away from the critical point. As a consequence, the generalized Nyquist diagram looks like the Nyquist diagram for a SISO system even though the open-loop eigenvalues are not at the same place. It seems to be that both the eigenvalues, which are located near the ends of the numerical range, travel approximately through the same path near the -1 point. Another observation is that the numerical ranges are practically line segments when they are close to -1 point. The thin numerical range implies that the open loop is normal at the plant output. The open loop is also normal at the plant output even though not shown in Figure 23. The test machine is already normal without the controller, so that is no big surprise. The second example is very skew and the controller has forced the open loop to be normal. The normality is not accidental, as can be seen by trying different rotordynamic parameters.

In the following a kind of intuitive explanation is given for normality. Later, more rigorous arguments will be given. For a normal matrix the largest and smallest singular values are the largest and smallest absolute values of its eigenvalues, and with a skew matrix they are bigger and smaller, respectively. As seen in the optimization layout, the sensitivity function at the plant output and the complementary sensitivity function at the plant input take part in the minimized frequency response matrix. Especially when the open-loop eigenvalues are near the -1 point, the largest singular values of these closed-loop functions are large. As the closed-loop frequency response functions are normal if, and only if, the open loop is normal at the corresponding location of the loop, the largest singular values are easiest to keep small when the open loop is normal. Because the open-loop eigenvalues suffer from the same phase-gain relationships as the gain and phase of a scalar plant (Doyle and Stein 1981), it is difficult to compensate the lost performance, due to skewness, by shaping the characteristic loci.

Let us pursue the analysis further to find the fundamental nature of the optimal solution. First, note that $\boldsymbol{R}$ can be approximated as $\boldsymbol{R}(s) \approx \boldsymbol{C}_{\mathrm{S2}}\left(\boldsymbol{M}_{\mathrm{rot2}} s^2\right)^{-1} \boldsymbol{B}_{\mathrm{b2}} = \boldsymbol{R}_{\mathrm{high}} / s^2$ at high frequencies. Actually, this approximation is valid already at the gain cross-over frequency range. Let us introduce two rotation matrices, $\mathbf{R}_{\mathrm{R1}}$ and $\mathbf{R}_{\mathrm{R2}}$, where the rotation angles are

chosen so that $\mathbf{R}_{R1}\,\boldsymbol{R}_{high}\,\mathbf{R}_{R2}$ is diagonal (see Equation 29). Next, the plant layout is modified as shown in Figure 24.

The problem of finding a controller ***C*** for rotor system ***R*** is changed to the problem of finding a controller ***C'*** for the system ***R'***. The original optimization problem has remained unchanged because the 2-norm of the vectors ***z'*** and ***w'*** are the same as the 2-norm of the vectors ***w*** and ***z***, respectively. All the weights and the amplifier block are diagonal and the rotor system ***R'*** approaches a diagonal matrix as the frequency increases. Thus, we have almost managed to separate the original MIMO optimization problem into two SISO problems. The only difficulty is that the rotor model ***R'*** is not necessarily diagonal at low frequencies. Despite this, let us solve the two SISO problems and compare the solutions to the original solution.

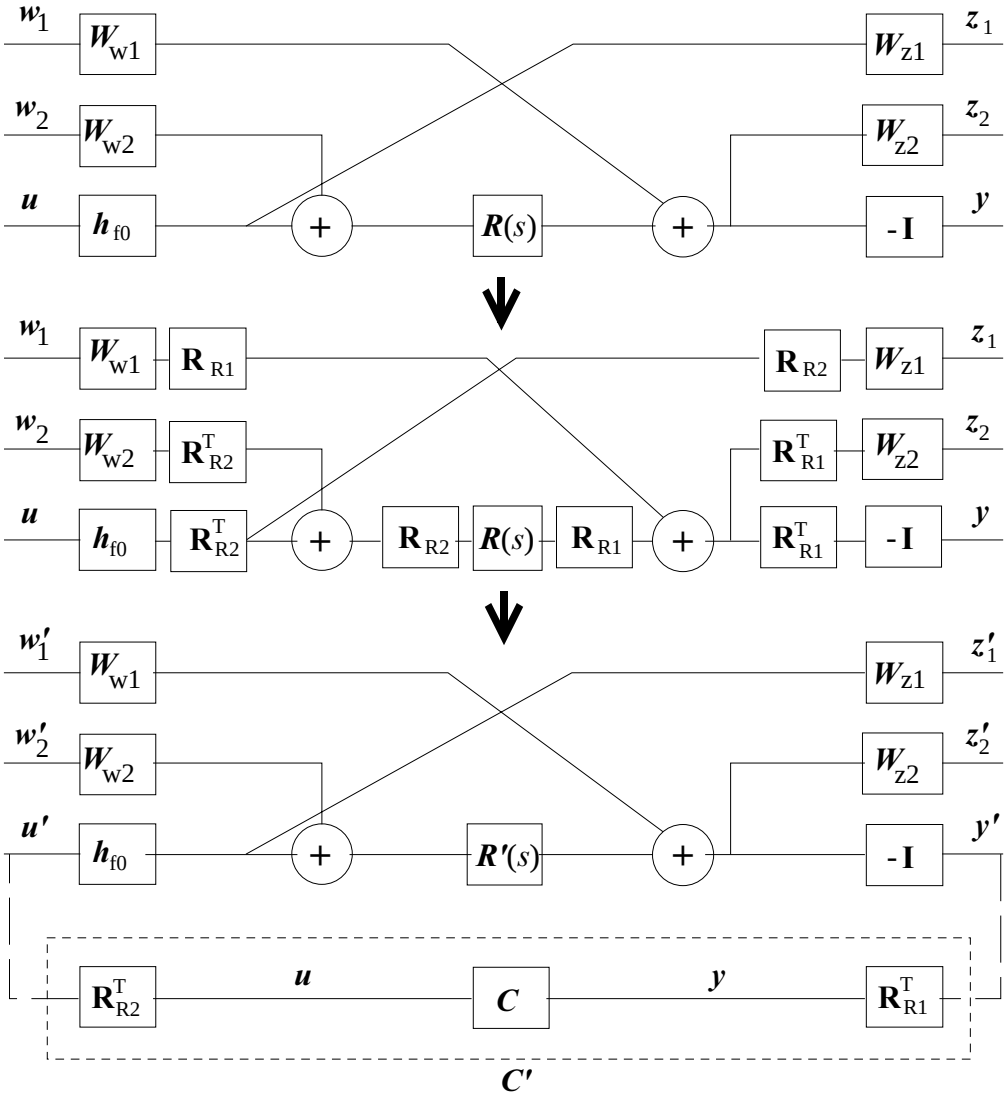

Figure 24. Approximate diagonalization of the rigid rotor suspension.

For the SISO optimization, the rotor model ***R'*** must be forced to be diagonal. How exactly this is done is explained in the following subsection. After diagonalization, the optimal SISO controllers are computed and the true controller is then realized as $\boldsymbol{C}(s) = \mathbf{R}_{\mathrm{R2}}\,\mathrm{diag}\{C_1(s), C_2(s)\}\,\mathbf{R}_{\mathrm{R1}}$. The elements of this controller and the original controller are plotted in Figure 25. The singular values of $F_l(\boldsymbol{P},\boldsymbol{C})$ for the two controllers are also shown.

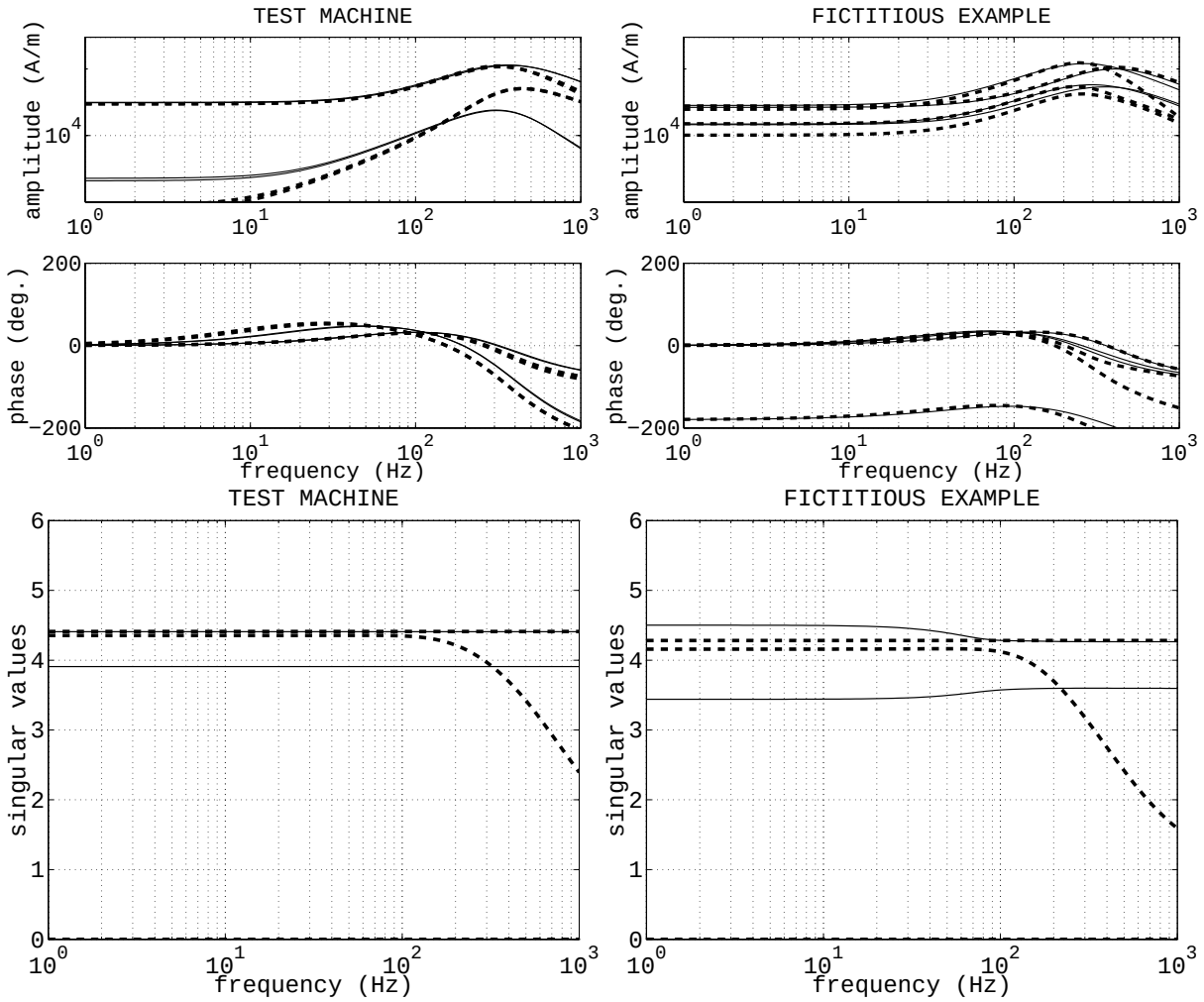

Figure 25. Comparison of the true optimal rigid body controller (bold dashed line) and the SISO design (thin line). At the top, the elements of the controller and at the bottom, the singular values of $F_l(\boldsymbol{P},\boldsymbol{C})$.

From Figure 25 we see that the frequency responses of both the controllers are practically the same at the critical frequency range from 50 Hz to 200 Hz. At lower and higher frequencies there are differences. However, the singular value plots reveal that both are equally good solutions to the stated problem, i.e. the largest singular values are practically the same at all

frequencies. Thus, an optimal controller for a rigid body can be obtained by the previous SISO design procedure.

The previous discussion also gives a mathematical reason for the normality of the optimal open loop. When ***P'*** and ***C'*** are diagonal then the open loop at the plant input, position ***u*** in Figure 25, is $\mathbf{R}_{\mathrm{R}2}\left(h_{\mathrm{f}0}\boldsymbol{C'R'}\right)\mathbf{R}_{\mathrm{R}2}^{\mathrm{T}}$ which is clearly normal. Similarly, the open loop is normal at the plant output, i.e. at the position ***y*** in Figure 25.

A normal matrix has some well-known good properties: its eigenvalues are insensitive to small perturbations and its largest and smallest singular values are the largest and smallest absolute values of the eigenvalues. These properties make normality an interesting property in the control system design. Actually, Hung and MacFarlane (1982) have proposed a design procedure called "reversed frame normalization" where the goal is to normalize the open loop at the plant input and output. However, in the present publication normality is based on the discussion of this subsection.

To conclude, the search for the worst-frequency optimal controller for a rigid body suspension can be separated into the search for the optimal controllers for two point mass systems. The optimal controller consists of frequency-independent input and output rotation matrices around a diagonal controller. A consequence of the problem statement is that the open loop becomes normal at the plant input and output. These observations are now generalized to a synthesis procedure.

The proposed synthesis procedure for subcritical slightly gyroscopic machines

In the previous subsection it was shown that an acceptable controller for a rigid body can be achieved by separating the system into two SISO systems and computing controllers for both separately. In the subcritical high speed machines the bending modes are usually clearly above the force bandwidth, and consequently AMB cannot effectively control these modes. Therefore, there is no need to optimize the control system with respect to the bending modes, so in the synthesis procedure we concentrate on rigid-body modes. Also, it is assumed that the rotor is not very gyroscopic so that the gyroscopic coupling need not be taken into consideration in the synthesis. This is usually the case in high-speed machines, except in flywheel energy storage systems. Of course, the gyroscopic effect is always taken into consideration in the analysis.

The proposed control system is shown in Figure 26. To make the approximate diagonalization, the rotation matrices should be chosen as

$$\begin{aligned}
&\mathbf{R}_{\mathrm{R1}} = \begin{bmatrix} \cos(\alpha_1) & -\sin(\alpha_1) \\ \sin(\alpha_1) & \cos(\alpha_1) \end{bmatrix}, \mathbf{R}_{\mathrm{R2}} = \begin{bmatrix} \cos(\alpha_2) & -\sin(\alpha_2) \\ \sin(\alpha_2) & \cos(\alpha_2) \end{bmatrix}, \\
&(r_{12} - r_{21})\cos(\alpha_1 + \alpha_2) = (r_{11} + r_{22})\sin(\alpha_1 + \alpha_2), \\
&(r_{12} + r_{21})\cos(\alpha_1 - \alpha_2) = (-r_{11} + r_{22})\sin(\alpha_1 - \alpha_2), \\
&\boldsymbol{R}_{\mathrm{high}} = \begin{bmatrix} r_{11} & r_{12} \\ r_{21} & r_{22} \end{bmatrix} = \boldsymbol{C}_{\mathrm{S2}} \boldsymbol{M}_{\mathrm{rot2}}^{-1} \boldsymbol{B}_{\mathrm{b2}},
\end{aligned} \tag{29}$$

where $\boldsymbol{R}_{\mathrm{high}}$ is the coefficient matrix of the high-frequency asymptote. The reduced model used in the SISO discussion in Section 3.2 was computed using rotation matrices with $\alpha_1 = \alpha_2 = 0$.

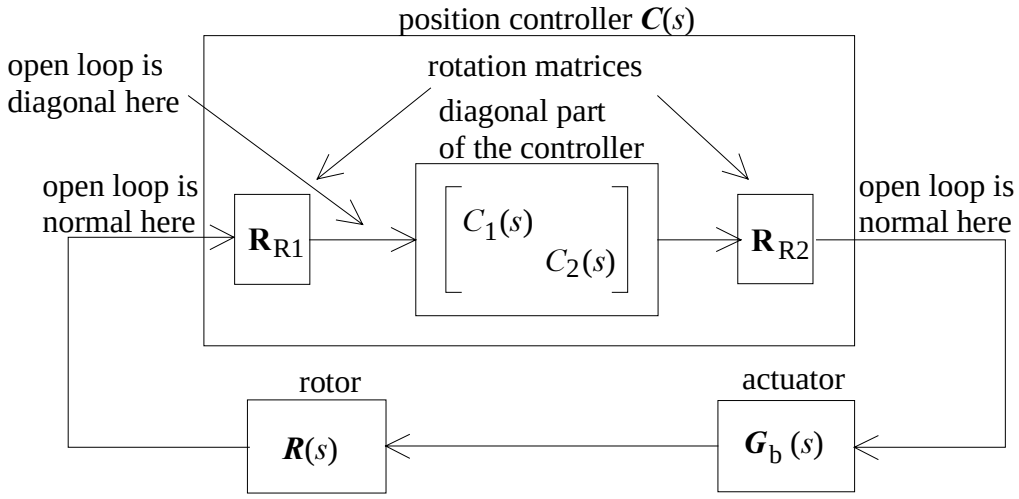

Figure 26. The proposed control system.

Now, the rotor systems seen by the controllers C_1 and C_2 are R_1 and R_2. At this point, there are a couple of complications. First of all, the system does not necessarily diagonalize at low frequencies. This is not so dangerous, because the system is nearly diagonal already at low frequencies. Basically, R_1 and R_2 are chosen as the diagonal elements of the nearly diagonal system. Another complication is that the diagonal elements are no longer second-order systems for a rigid rotor, rather they are fourth-order systems. However, without large errors they may be approximated by second-order systems. Thus, R_1 and R_2 are the following approximations of the true diagonal elements

$$R_1(s) = \frac{1}{m_{\mathrm{r}1}s^2 - c_{\mathrm{r}1}} + \sum_{n=3}^{N_{\mathrm{mode}}} \frac{v_{\mathrm{nr}1}}{m_n s^2 + d_n s + k_n},$$
$$R_2(s) = \frac{1}{m_{\mathrm{r}2}s^2 - c_{\mathrm{r}2}} + \sum_{n=3}^{N_{\mathrm{mode}}} \frac{v_{\mathrm{nr}2}}{m_n s^2 + d_n s + k_n}, \tag{30}$$

where m_{n}, d_{n} and k_{n} are the nth diagonal elements of the matrices $\boldsymbol{M}_{\mathrm{rot}}$, $\boldsymbol{D}_{\mathrm{rot}}$ and $\boldsymbol{K}_{\mathrm{rot}}$, respectively and

$$m_{\mathrm{r}1} = 1/\left[\mathbf{R}_{\mathrm{R}1}\,\boldsymbol{C}_{\mathrm{S}2}\boldsymbol{M}_{\mathrm{rot}2}^{-1}\boldsymbol{B}_{\mathrm{b}2}\,\mathbf{R}_{\mathrm{R}2}\right]_{1,1},\ m_{\mathrm{r}2} = 1/\left[\mathbf{R}_{\mathrm{R}1}\,\boldsymbol{C}_{\mathrm{S}2}\boldsymbol{M}_{\mathrm{rot}2}^{-1}\boldsymbol{B}_{\mathrm{b}2}\,\mathbf{R}_{\mathrm{R}2}\right]_{2,2},$$
$$c_{\mathrm{r}1} = \left[\left(\mathbf{R}_{\mathrm{R}1}\,\boldsymbol{C}_{\mathrm{S}2}\left(\boldsymbol{B}_{\mathrm{b}2}c_0\boldsymbol{B}_{\mathrm{b}2}^{\mathrm{T}}\right)^{-1}\boldsymbol{B}_{\mathrm{b}2}\,\mathbf{R}_{\mathrm{R}2}\right)^{-1}\right]_{1,1},\ c_{\mathrm{r}2} = \left[\left(\mathbf{R}_{\mathrm{R}1}\,\boldsymbol{C}_{\mathrm{S}2}\left(\boldsymbol{B}_{\mathrm{b}2}c_0\boldsymbol{B}_{\mathrm{b}2}^{\mathrm{T}}\right)^{-1}\boldsymbol{B}_{\mathrm{b}2}\,\mathbf{R}_{\mathrm{R}2}\right)^{-1}\right]_{2,2},$$
$$v_{m\mathrm{r}1} = \left[\mathbf{R}_{\mathrm{R}1}\,\boldsymbol{C}_{\mathrm{S}}\right]_{1,n} * \left[\boldsymbol{B}_{\mathrm{b}}\,\mathbf{R}_{\mathrm{R}2}\right]_{n,1},\ v_{m\mathrm{r}2} = \left[\mathbf{R}_{\mathrm{R}1}\,\boldsymbol{C}_{\mathrm{S}}\right]_{2,n} * \left[\boldsymbol{B}_{\mathrm{b}}\,\mathbf{R}_{\mathrm{R}2}\right]_{n,2}, \tag{31}$$

where $m_{\mathrm{r}1}$ and $m_{\mathrm{r}2}$ are the reduced masses,
$c_{\mathrm{r}1}$ and $c_{\mathrm{r}2}$ are the reduced positive stiffnesses and
$v_{\mathrm{nr}1}$ and $v_{\mathrm{nr}2}$ are the reduced influence factors.

The reduced masses are computed from the high-frequency asymptote assuming that the other controller has zero gain and the reduced position stiffnesses are computed from the low-frequency asymptote assuming that the other controller has infinite gain. For the reduced mass there is no difference whether the other controller gain is assumed zero or infinite because the high-frequency asymptote is diagonal. The position stiffness is computed assuming infinite gain in order to get accurate stability predictions already from SISO designs and thereby reduce unnecessary iteration. The stability margin against gain drop is determined by the point where the Nyquist curve first crosses the real axis (about -3.2 in Figure 16). This point is at low frequency and depends on the ratio between position stiffness and controller gain. At this frequency the other loop has a high gain and consequently the assumption of infinite gain is a better approximation than zero gain. In practice, however, the difference is usually small.

The proposed synthesis procedure is the following:

1. Obtain the two rotation matrices from Equation 29.
2. Compute the two SISO systems from Equations 30 and 31.
3. Design two controllers using the SISO design guides given in Section 3.2
4. Analyze the true MIMO plant using the generalized Nyquist diagram and make the necessary improvements to the controller
5. Make experimental testing and possible nonlinear simulations and return to step 3 or 4, if necessary.

There may be need to improve the SISO-design because the gyroscopic effect and the uncertain sensor sensitivity are not taken into consideration in the SISO-design stage.

Note that the physical basis, in the diagonalization with rotation matrices, relies on the fact that the bearings are similar, i.e. $F_{\max}$ is equal and the rotor displacement is equally important in both rotor ends. Even though it is relatively easy to relax these constraints, this more general case is not considered here in order to keep the treatment simple. Also, the above assumptions do hold in the case of high-speed machines almost without exception.

Controller design for the test machine

Now the design procedure is applied to the test machine. For the test machine,

$$\boldsymbol{R}_{\text{high}} = 0.0418\begin{bmatrix} 1 & -0.442 \\ -0.435 & 1.081 \end{bmatrix}. \tag{32}$$

Thus, the 1 and 2 ends are clearly interconnected. A solution to Equation 29 is $\alpha_1 = -42.4^\circ$ and $\alpha_2 = 42.3^\circ$. The angles are very close to ±45°, which means that the natural modes are approximately purely translatory and purely conical modes. Therefore, let us choose $\alpha_1 = -45^\circ, \alpha_2 = 45^\circ$ to keep the control system as clear as possible. Now the diagonalized rotor models are

$$\begin{aligned} R_1(s) &= \frac{1}{39.7s^2 - 2.3*10^6} + \frac{0.154}{3.84s^2 + 63s + 64.5*10^6}, \\ R_2(s) &= \frac{1}{16.2s^2 - 2.0*10^6} + \frac{0.003}{3.84s^2 + 63s + 64.5*10^6}. \end{aligned} \tag{33}$$

The first system corresponds to the rigid-body translatory mode and the second to the rigid-body conical mode. The position bandwidths for the two systems are 90 Hz and 140 Hz, computed for p_{max}=100 µm. Therefore, the gain cross-over frequency of the first system should be slightly below 100 Hz and for the second system slightly above 100 Hz. As seen from Equation 33, the first bending mode is essentially controlled by the first controller. As the position bandwidth of the first system is quite far away from the first bending eigenfrequency, strategy C (Section 3.2) is adopted for bending mode damping. For the second controller, the nominal influence factor is 0.003, but it achieves both positive and negative values as the output and input uncertainties vary. Therefore, the second controller should have a small amplitude and/or phase near 0° or -180° at the first bending eigenfrequency.

First, the current feedback coefficient is chosen so that it will not cause too high a phase drop at the higher of the two gain cross-over frequencies. In this case, k_{cf}=200 V/A is a suitable value. Then the controllers are designed using the ideas considered in Section 3.2. The results are

$$\begin{aligned} C_1(s) &= \frac{(2\pi 350)^2}{s^2 + 2*0.2*(2\pi 350)s + (2\pi 350)^2}\left(25000\left(1+\frac{1}{0.15s}\right)+\frac{55s}{0.00035s+1}\right)* \\ &\quad \frac{s^2 + 2*0.15*(2\pi 700)s + (2\pi 700)^2}{s^2 + 2*0.15*(2\pi 600)s + (2\pi 600)^2}\left(\frac{600}{700}\right)^2, \\ C_2(s) &= \frac{(2\pi 600)^2}{s^2 + 2*0.25*(2\pi 600)s + (2\pi 600)^2}\left(22000\left(1+\frac{1}{0.15s}\right)+\frac{37s}{0.0001s+1}\right)* \\ &\quad \frac{s^2 + 2*0.05*(2\pi 700)s + (2\pi 700)^2}{s^2 + 2*0.2*(2\pi 800)s + (2\pi 800)^2}\left(\frac{800}{700}\right)^2. \end{aligned} \tag{34}$$

Note that the amplifier time constant is no longer included in the position controller transfer functions. However, actuator dynamics (Equation 3) are included into the controller dynamics in the Bode plot in Figure 27. The open-loop Bode diagram is also shown in Figure 27.

The controller C_1 has a phase-drop filter near the bending mode to drop the phase clearly below -180°. The controller C_2 has a notch filter placed at the bending eigenfrequency. This is installed because the gain of C_2 would be quite high at this frequency, and the phase would be approximately -90°. So the controller C_2 would have quite a strong destabilizing effect on the

bending mode at some uncertainty combination. When a notch filter is used, this destabilizing effect is always clearly smaller than the stabilizing effect of C_1.

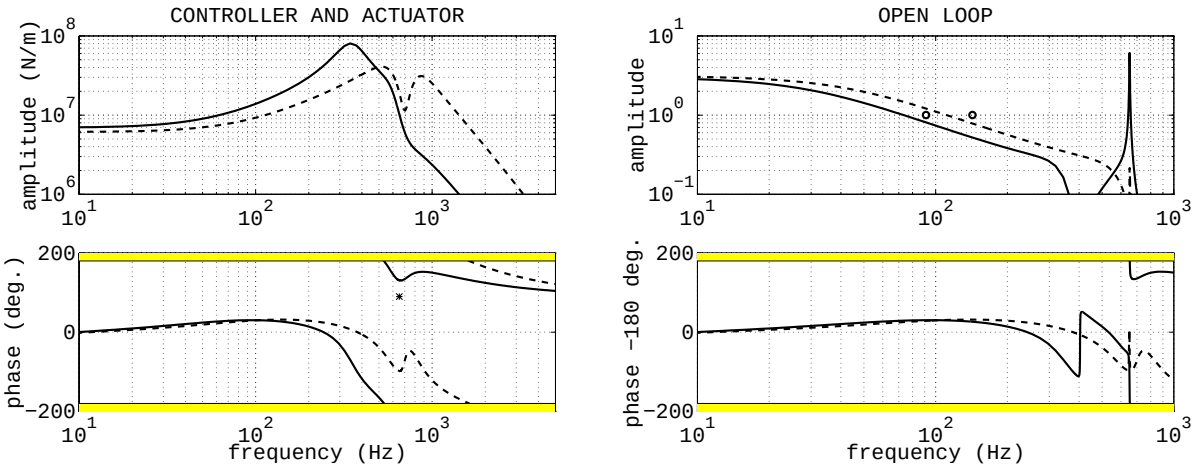

Figure 27. The Bode diagrams of the controller-actuator and open loop. The first channel is drawn with a solid line and the second channel with a dashed line. The position bandwidths are labeled with a circle and the first bending eigenfrequency (652 Hz) with an asterisk.

The Nyquist curves for the two SISO systems are shown in Figure 28.

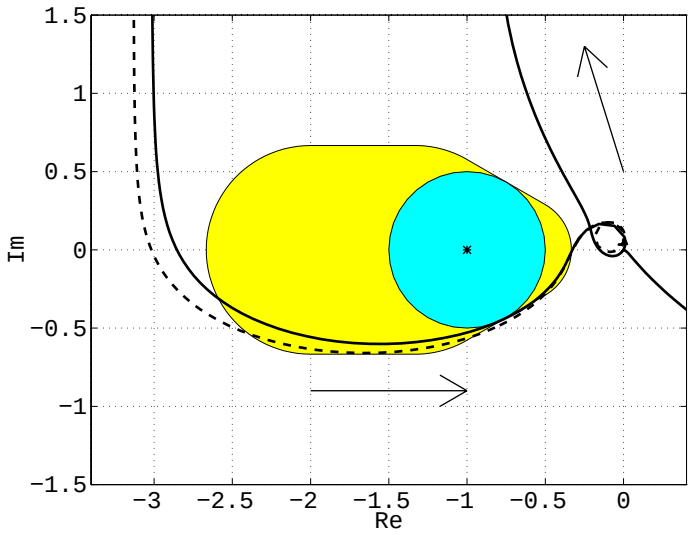

Figure 28. Nyquist diagram of the SISO design. The arrow shows the direction of increasing frequency. Loop 1 is drawn with a solid line and loop 2 with a dashed line.

From Figure 28 we see that the SISO systems are satisfactory.

Next, let us analyze the system using the generalized Nyquist diagram. The analysis is done at zero speed and a maximum speed of 540 Hz. Two diagrams are computed for both speeds; the low frequencies and the frequencies near the first bending eigenfrequency. At low

frequencies the unstructured version of the diagram is used because then we also obtain the performance information described in Appendix A. Near the bending eigenfrequency the structured version is used. Actually, the open loop becomes so skew near the bending mode that the predictions of the unstructured diagram would be too conservative. The position sensitivity error is assumed 10 %. The generalized Nyquist diagrams are shown in Figure 29.

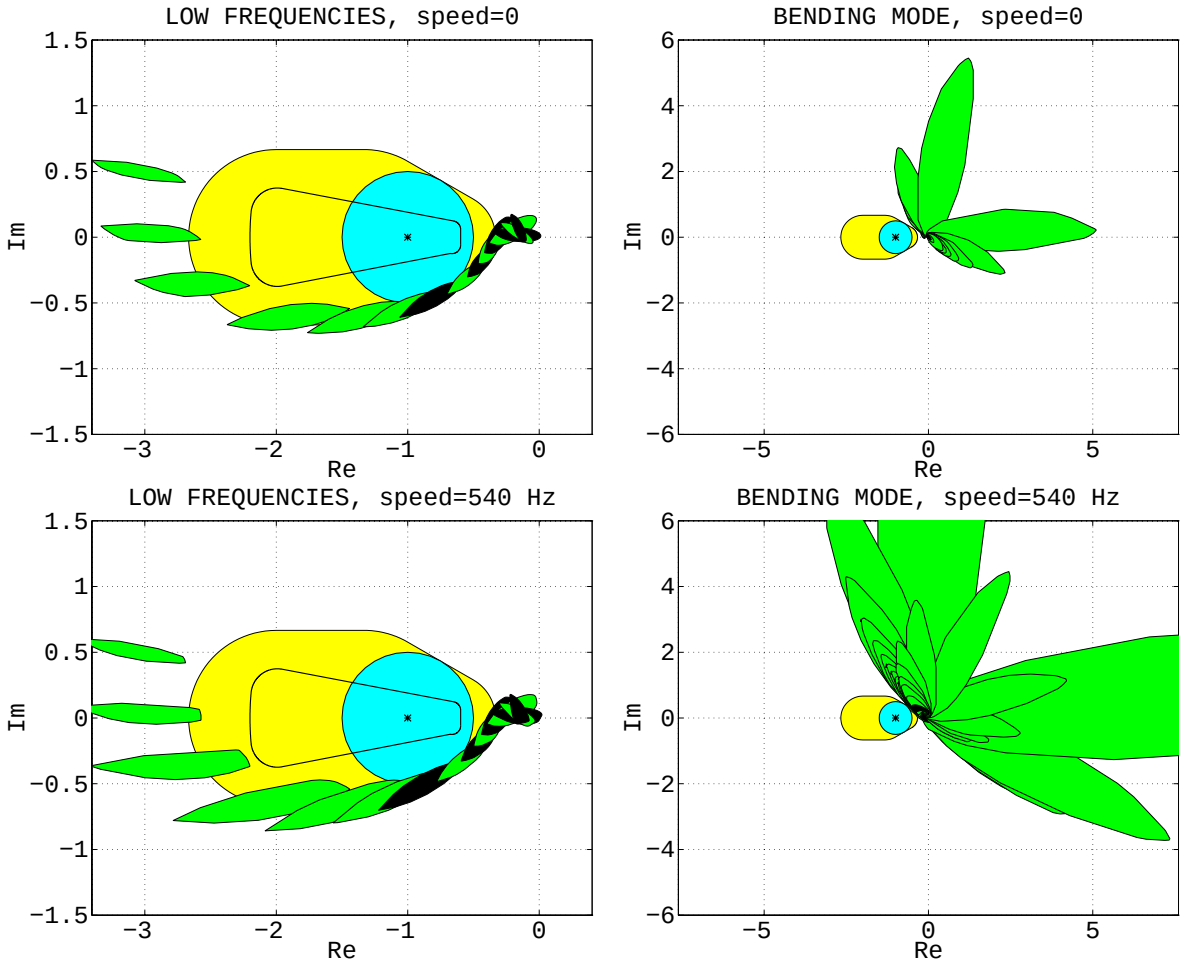

Figure 29. The generalized Nyquist diagram of the test machine. The low frequencies are 5, 10, 20, 40, 60, 80, 100, 150, 200, ..., 500 Hz and the diagram near the bending mode is computed starting from 500 Hz using very small frequency steps near the resonance. Near the bending mode at full speed, the numerical ranges are drawn in reversed order, because otherwise large numerical ranges corresponding to forward mode would cover all other numerical ranges.

The set of Nyquist diagrams reveals that the system is very good. Robust stability is obtained which is seen from the fact that the numerical ranges do not penetrate inside the forbidden region for robust stability (see Appendix A). Also, the numerical ranges penetrate only slightly inside the forbidden region for robust performance. This means that the system

behaviour remains acceptable with all parameter variations. The system tolerates a gain drop of about 0.38 and gain increase of about 2.6.

At full speed, the numerical ranges will be slightly larger at low frequencies due to gyroscopic coupling. This effect is relatively small, and consequently there is no considerable performance degradation. The bending mode also remains stable at zero speed and full speed. At full speed the numerical ranges will be very large near the forward bending mode eigenfrequency, due to diminishing effect of material damping.

3.5 Experimental analysis

The achieved control system was implemented using analog circuits. In this section some experimental tests and nonlinear analyses are presented.

Small signal behavior

First, the stability limits were experimentally checked. The rotor was levitating and the gains at the 1-end and 2-end position controller outputs were changed from their nominal values using potentiometers. The system was detuned to the stability limit and the values of the potentiometers were read. The true current stiffness was measured and it was 336 N/A. The potentiometer readings were therefore scaled by 336/280 to make them comparable with the stability margin predictions. The results are shown in Figure 30. The predicted stability limits are obtained from Figure 29. The Nyquist diagram predicts that the system should tolerate gain increase by a factor of 2.6 and decrease by a factor of 0.38. A more accurate stability border prediction was computed using state space realization with nominal parameters and neglecting motion voltage term and coil resistance.

As seen, the stability border achieved from the generalized Nyquist diagram is about 10 % smaller than that achieved from state space realization. This is natural because in the Nyquist diagram 10 % error was assumed for the position measurement sensitivity. So, in the present case the Nyquist diagram gives highly nonconservative stability margin predictions.

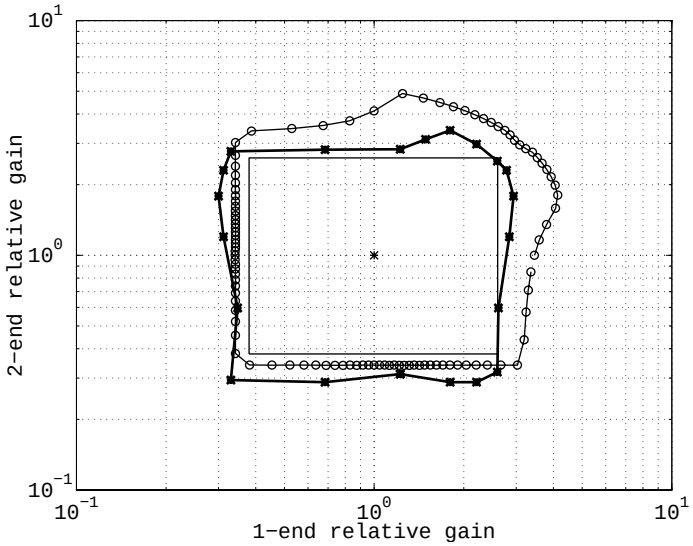

Figure 30. The measured and predicted stability borders. The measured points are labeled with asterisks (*) and connected by a bold line. The prediction from state space realization is labeled with circles (o) and the prediction achieved from the generalized Nyquist diagram is drawn with thin line.

The measured stability region is as wide as the predicted regions, but it is a little bit shifted. This shift is probably due to inaccurate current stiffness measurement. Also, the stability limit at high gain is difficult to determine. When the gain is increased, the system starts to oscillate at a small amplitude, which is heard as an audible noise. From this value the gain can be considerably increased before the vibration becomes intolerably high. The measured value is taken from the limit where the very small vibration starts. Anyway, the measured stability margins match very well with the predicted ones.

To analyze the system performance a force impulse was used. The rotor was hammered at the 1-end and the position responses and reference currents were measured at the 1-end bearing. This was repeated with three gain combinations and the results are shown in Figure 31. The impulse responses are very nice for all gain combinations. Also, it is seen that the control action is in good balance with the disturbance amplitude, i.e. when the displacement is near the maximum 200 μm, the reference current is also maximum.

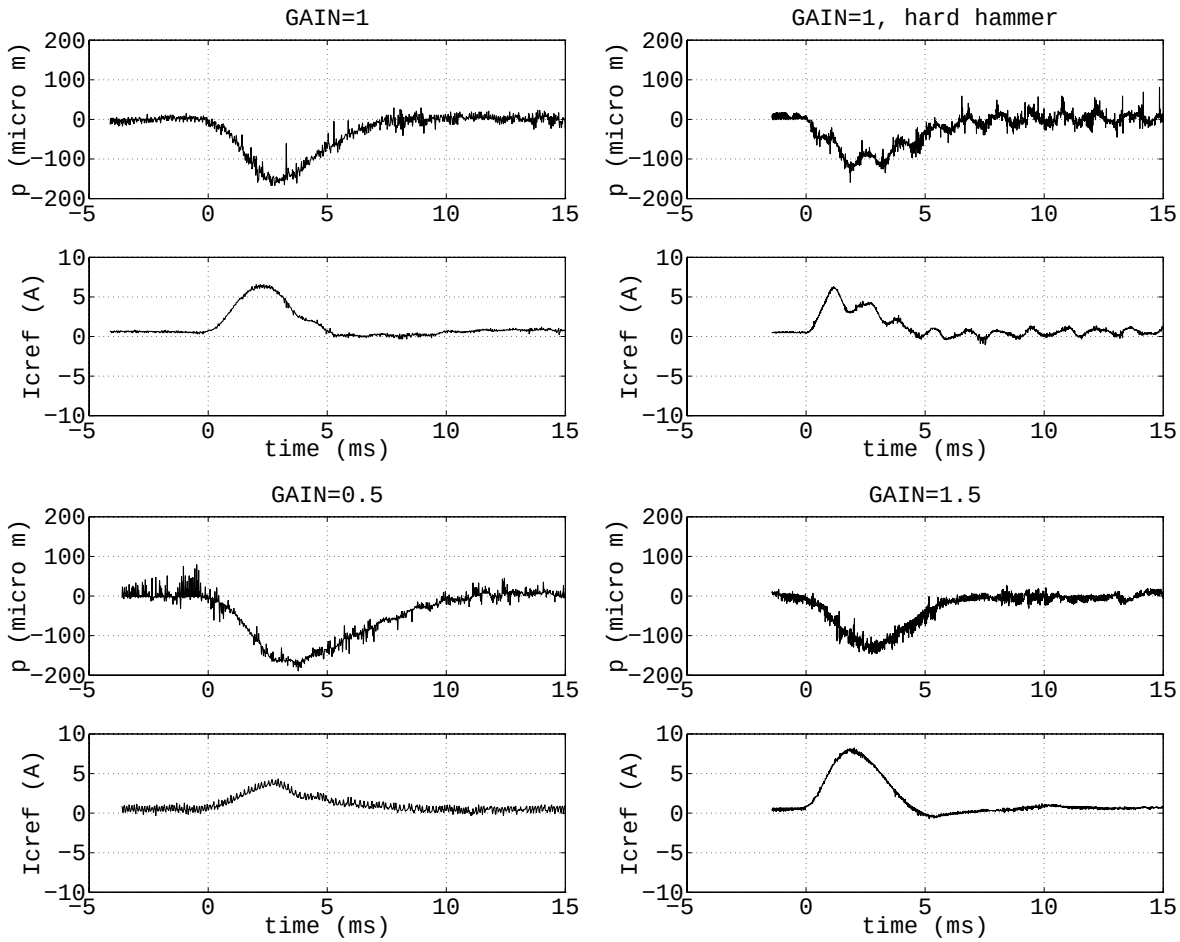

Figure 31. Impulse responses. The rotor is hammered, and the position and reference current are measured at the 1-end.

In three impulses the rotor was hammered with a soft hammer and in one test with a hard hammer. The hard hammer also excites the first rotor bending mode, which is clearly seen in the impulse response. In this test, the impeller was removed because it must not be hammered. Therefore, the first bending eigenfrequency was at a frequency 720 Hz, while it is 650 Hz with the impeller. The true damping of the first bending mode with impeller was measured using frequency sweep. A constant amplitude sinusoidal disturbance was fed into the controller output and the position signal was measured. First, the frequency f_0 where the position vibration was at maximum was found. Then, two frequencies f_1 and f_2, around f_0 where found, where the amplitude was half of the maximum. The bending damping was then computed as; $\text{damping} = \left(f_2 - f_1\right) / \left(\sqrt{12} f_0\right) = 29 / \left(\sqrt{12} * 640\right) = 0.013$. This agree very well with the prediction achieved from state space realization, which is 0.015. Even though the first bending mode is poorly damped, the situation is not dangerous because in the real machine there are no high forces at frequencies near the bending eigenfrequency.

Stability at high signal amplitudes

In the AMB system, it is easy to construct a situation where the suspension remains stable when not disturbed but starts oscillating when disturbed by a large impulse, like hammering. This kind of behavior is dangerous, as large disturbances may occur in practice and the resulting oscillation is a very violent phenomenon that may cause mechanical damage.

The test machine was experimentally tested by changing the gain between the small signal stability limits, shown in Figure 30. At the same time the rotor was firmly hammered with a rubber hammer. After extensive searching and hammering, the described behavior did not occur. If the test machine were stable in the small-signal sense, it could not be destabilized by large disturbances.

Let us next analyze how the high-signal stability could be predicted. Practical experience tells us that the most common and most dangerous high-signal instability causes vibration at a frequency near the gain cross-over frequency. Because the system gain drops relatively fast at this frequency, a kind of describing function method is used to analyze the stability. The nonlinear behavior is due to amplifier saturation, i.e. the response from current reference to controlled bearing force changes at high signal amplitudes. If 1 is the nominal response, $g_{\mathrm{rel}}(a,\omega)$ is the first harmonic response at reference current amplitude a and frequency ω. This function is computed in Section 2.2 using simulations with the nonlinear actuator model. When the higher harmonics are neglected, the following harmonic balance must be satisfied at limit cycle oscillation.

$$\begin{aligned} &\boldsymbol{K}\boldsymbol{L}_0\boldsymbol{x} = -\boldsymbol{x}\,, \\ &\boldsymbol{K} = \mathrm{diag}\left\{g_{\mathrm{rel}}(a_1,\omega), g_{\mathrm{rel}}(a_2,\omega), g_{\mathrm{rel}}(a_3,\omega), g_{\mathrm{rel}}(a_4,\omega)\right\}, \end{aligned} \tag{35}$$

where $\boldsymbol{L}_0$ is the nominal open-loop frequency response matrix at the plant input, $\boldsymbol{K}$ is the relative first harmonic response of the amplifier and $\boldsymbol{x}$ is an eigenvector. The behaviour of the diagonal elements $g_{\mathrm{rel}}(a,\omega)$ as a increases is shown in Figure 9. At a certain frequency, the amplitude decreases and there will be negative phase shift. If we allow every diagonal element in $\boldsymbol{K}$ to be on this curve, then the inverse of the uncertainty region $\phi(\boldsymbol{K})$ is the region of complex numbers left between the positive real axis and the curve $g_{\mathrm{rel}}(a,\omega)$, when a is increased to infinity. Thus, we could analyze the high-signal stability by scaling the nominal

numerical range $\varphi(\boldsymbol{L}_0)$ by all the numbers in $1/\phi(\boldsymbol{K})$. Clearly, it suffices to scale the numerical ranges only by the values on the border of $1/\phi(\boldsymbol{K})$. Further, due to the shape of the Nyquist curve at the interesting frequency range, it is sufficient to scale the numerical ranges by the values on the curve $g_{\mathrm{rel}}(a,\omega)$. It should be emphasized that this analysis makes sense only at frequencies starting approximately from the position bandwidth, because at low frequencies contact with the retainer bearings occurs at such a high signal amplitude where the amplifier gets saturated. Therefore, the frequencies in Figure 32 start just from 50 Hz. The Nyquist diagram scaled with $g_{\mathrm{rel}}(a,\omega)$ is shown in Figure 32 for maximum voltage $V_{\max}$=150 V and $V_{\max}$=75 V.

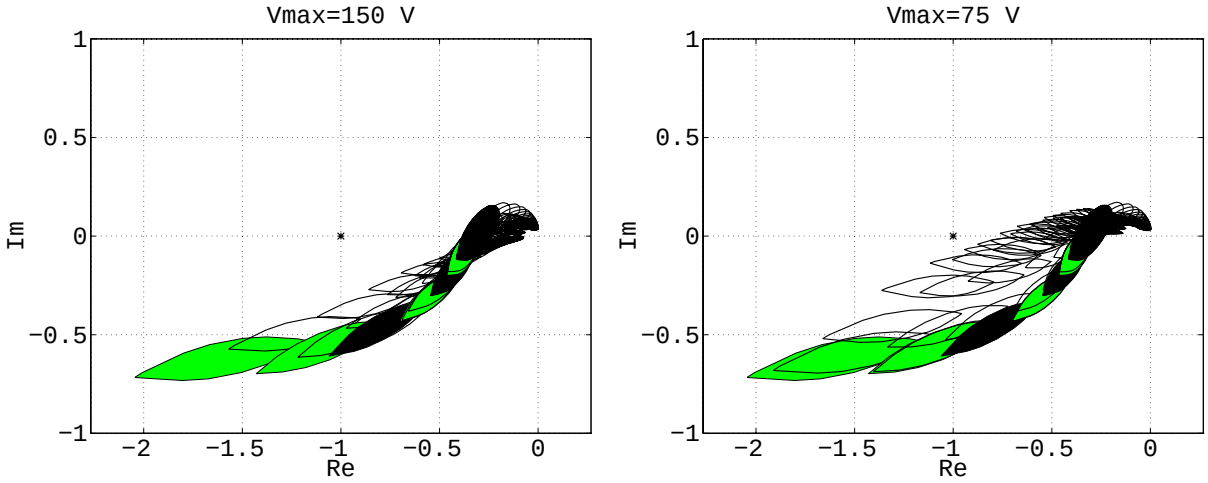

Figure 32. Analysis of the stability at high signal amplitudes. The frequencies are 50, 75, 100, 150, 200, 250 and 300 Hz.

When the maximum voltage is 150 V, the numerical ranges computed for $g_{\mathrm{rel}}(0,\omega)$ will cross the -1 point first when the system gain is increased. This means that there does not exist such a gain combination where the system could stay in limit cycle oscillation. So, the prediction is that if the system is stable in the small-signal sense then it can not be destabilized by large disturbances either. This prediction turned out to be correct. When the voltage is limited to 75 V, the situation is essentially different. When the gain is increased by 50 %, the scaled numerical ranges cross the -1 point and the small signal Nyquist plot does not. Now there is a risk of high-signal instability even if the system was stable in the small-signal sense.

The voltage of the test machine was dropped to 75 V and the gain was increased by 50 %. The system remained stable in the small-signal sense. Then the 1-end was radially hammered

by medium amplitude and then by large amplitude. The resulting position signal and the UP-coil current at the 1-end bearing are shown in Figure 33.

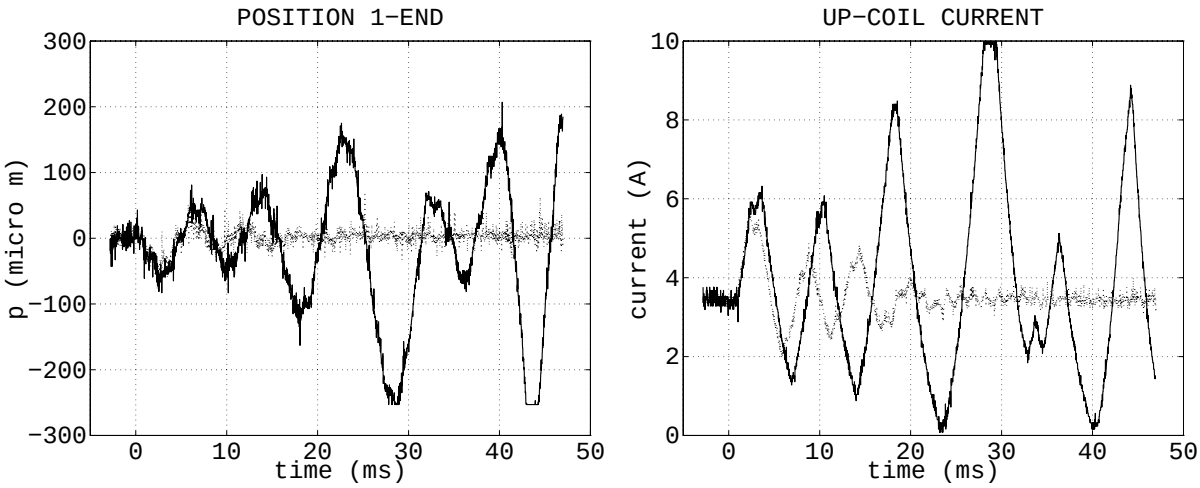

Figure 33. Experimental testing of the high amplitude response. Medium impulse is drawn with a dotted line and high impulse with a solid line.

At the smaller impulse the amplifier does not become too saturated and the controller is able to stabilize the suspension. When the impulse is large, the true bearing current will be considerably delayed from the small-signal behavior. If the impulse is high enough, this delay is so high that the bearing turns from damper into amplifier and instability occurs. In the present case, the vibration amplitude increases so much that the rotor will contact the retainer bearings (near 30 ms).

From the previous analysis we can conclude that the bearing voltage should be sufficient. To ensure good behavior at higher disturbance amplitudes, a good rule of thumb is that the force bandwidth should be somewhat higher than the position bandwidth, i.e. the gain cross-over frequency.

The effect of amplifier saturation

Let us next see how amplifier saturation, caused by unbalance vibration or some other high-frequency disturbance, like sensor noise, affects stability. First, let us compute the magnitude of the position vibration that drives the amplifier to the saturation border. Let $\boldsymbol{p}_{\mathrm{S}}$ be the position measurement vibration and $\boldsymbol{V}_{\mathrm{c}}$ be the control voltage. These are related as $\boldsymbol{V}_{\mathrm{c}}(s) = \boldsymbol{G}_{\mathrm{pV}}(s)\boldsymbol{p}_{\mathrm{S}}(s)$. At every frequency, let us compute the smallest position vibration

that produces control voltage vibration $V_{\max}$=150 V. Because of the multivariable plant, there are several ways to define this vibration. Here a kind of worst-case approach is adopted. Let us ask what the largest vibration p_{sat} is which exists at both the rotor ends at the same time and which does not saturate the amplifier. The answer is

$$\begin{aligned} p_{\text{sat}}(\omega) &= \frac{V_{\max}}{\left\| \boldsymbol{G}_{\text{pV}}(j\omega) \right\|_{\infty}}, \\ \boldsymbol{G}_{\text{pV}}(s) &= \text{diag}\left\{ G_{\text{rV}}(s), G_{\text{rV}}(s), G_{\text{rV}}(s), G_{\text{rV}}(s) \right\} \boldsymbol{C}(s), \\ G_{\text{rV}}(s) &= \frac{k_{\text{cf}} L_{\text{dyn}} s}{L_{\text{dyn}} s + k_{\text{cf}}}. \end{aligned} \tag{36}$$

This is plotted in Figure 34. As can be seen, only a couple of micrometers vibration amplitude at 350 Hz leads to amplifier saturation. This is much less than the clearance of the retainer bearing, which is 250 μm and it is easily caused by rotor unbalance. Fortunately, the suspension does not become unstable when some amplifier is only slightly saturated. In a practical AMB system the amplifier saturation levels must be monitored, and an alarm must be set when the saturation level is dangerously high. To avoid unnecessary alarms and still ensure safe operation, the dangerous level should be known. This important question is analyzed next.

The high-frequency high-amplitude disturbance causes an amplitude drop and a negative phase in the first harmonic response of the actuator at lower frequencies as seen in Section 2.2. The relative first harmonic response is a function of disturbance amplitude, i.e. saturation level, and the frequency and amplitude of the fundamental wave. This is $g(a_{\text{i}}, \omega, a_{\text{rel}})$, where a_{i} and ω are the amplitude and frequency of the fundamental signal and a_{rel} is the saturation level (see Section 2.2). By the same reasoning as in the analysis of high amplitude response, we draw the Nyquist diagram scaled by $g(a_{\text{i}}, \omega, a_{\text{rel}})$, where a_{i} is small. The result is shown in Figure 34.

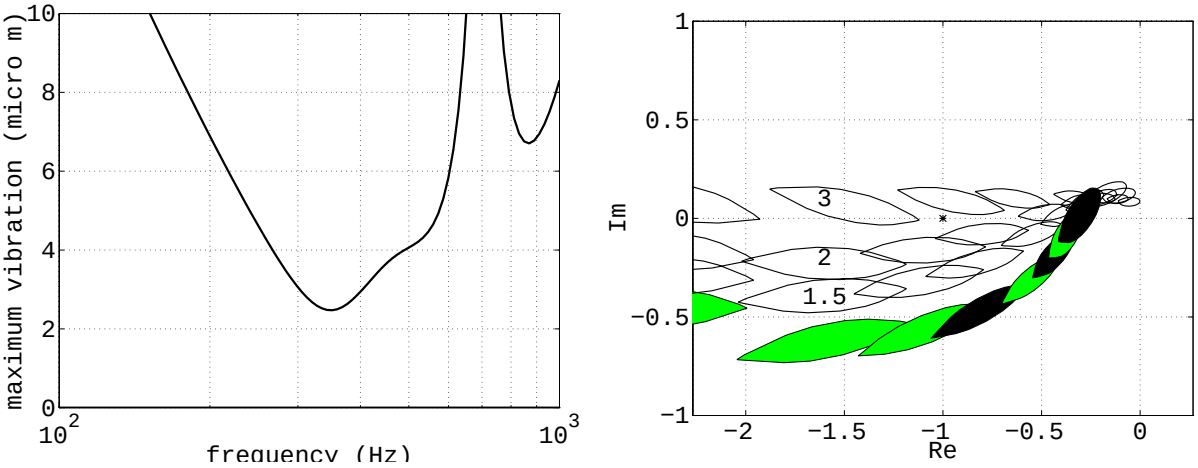

Figure 34. Theoretical analysis of the effect of the amplifier saturation. On the left-hand side the maximum tolerated vibration p_{sat}, and on the right-hand side the scaled Nyquist diagram. The saturation levels are 0, 1.5, 2 and 3. The amplitude a_i is small.

Thus, the system should tolerate a saturation level of more than 2 at every channel simultaneously. If the system goes into limit cycle oscillation, the frequency of such oscillation should be somewhere between 75 Hz and 100 Hz. The prediction of limit cycle oscillation is based on the behavior of $g(a_i,\omega,a_{rel})$, as the amplitude a_i of the fundamental wave is increased; see Figure 10.

These predictions were tested by inserting a 500 Hz sinusoidal disturbance into outputs of both the channels in an X-plane. The amplitude of this sine wave was increased until the suspension became unstable. Then, this was repeated by inserting the sinusoidal signal only at the 1-end bearing. In the first case, the instability occurred at a saturation level of 2.9 and in the second case when the saturation level was 3.8. So, these stability thresholds agree well with the predicted values. The position signals in the resulting limit cycle oscillations are shown in Figure 35. Also, the reference current and the true current in the UP-coil are shown.

Thus, we could say that the system tolerates well a saturation level of approximately 2. Still, the system tolerates only about 5 μm vibration at the speed 350 Hz, and the rotor unbalance can easily cause many times this amount of vibration. Therefore, in a practical AMB system the rotor unbalance needs special treatment. This is considered in Chapter 4. Larsonneur (1990) has observed the previously-described destabilizing effect in a high-speed test machine when passing a bending critical speed. He also made simulations with the nonlinear bearing model and managed to reconstruct the instability by simulation.

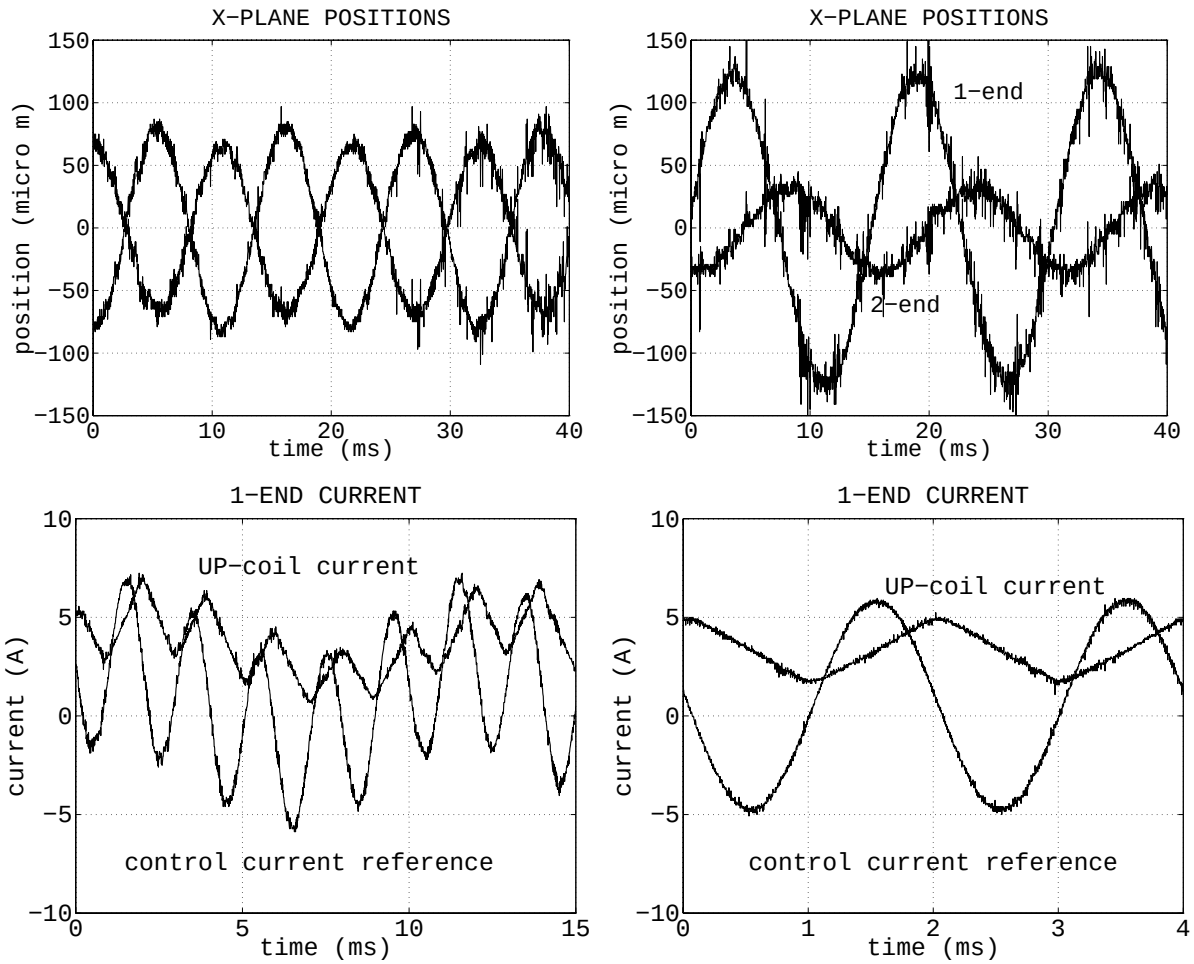

Figure 35. Limit-cycle oscillation caused by amplifier saturation. On the left-hand side the disturbance is fed into both channels and on the right-hand side into the 1-end only.

Other nonlinearities and unmodeled dynamics

In the AMB system there are several kinds of nonlinearities and unmodeled dynamics. So far we have studied the effect of magnetic circuit saturation by computing the parameters of the linearized model at different operational points. The effect of amplifier saturation is studied using simulations with the nonlinear model combined with the generalized Nyquist diagram. There are, however, other effects that have not been considered.

First, the position measurement noise is not directly taken into consideration in the design procedure. However, the measurement noise is indirectly handled by quickly dropping the controller gain at high frequencies. In the design procedure, we try to drop the controller gain as fast as possible at high frequencies. By following this very general design practice, the noise will not become a problem.

The biggest unmodeled effect is the stator-side mechanics. In the design, we have assumed that the electromagnets and position sensors are very tightly connected to a massive foundation, i.e. they do not move. In practice, the magnetic force produced by the electromagnets does not only move the rotor but also the electromagnets and sensors. At frequencies near the stator-side mechanical resonances, this effect may become very large, i.e. a small bearing force may cause large vibrations at the electromagnets and position sensors. Usually, the lowest stator-side resonances are at lower frequencies than the rotor resonances, and there are lots of stator resonances in the frequency range where the bearings can produce considerable force. Thus, the stator-side resonances may cause similar ringing problems to the ones caused by rotor bending modes.

Because there are lots of mechanical resonances in the stator, it may become very difficult to handle them with the control system. A further problem is that the stator-side resonances depend considerably on the mounting and assembly. For example, some parts of the turbomachine may be disconnected in maintenance and still the bearings should work well.

Fortunately, the damping in the stator-side mechanical resonances is usually of the order of ten times higher than in the rotor bending modes. Therefore, these resonances are not as dangerous as the rotor-side resonances. Also, it is relatively easy to modify the stator-side mechanics to increase the damping or otherwise modify the resonant modes. In the author’s experience, the stator-side resonances are often below the risk limit and if they are not, then the problems are easiest to handle with mechanical modifications.

The stator-side resonances are not taken into consideration in the controller synthesis. After the controller is achieved, certain limits are computed for the stator-side resonances and the stator is measured with an impulse hammer or a shaker to ensure that there are no problems. If the measurements reveal that there is the risk of ringing, then the mechanics are modified. The stator-side resonances are considered in detail by Lantto *et al.* (1996).

4 UNBALANCE COMPENSATION AND BALANCING

4.1 Literature review

Even though rotors are usually made rotary-symmetrical, they have small unidealities in the mass distribution, called unbalance. The effect of unbalance can be interpreted as a generalized force acting on the rotor and rotating at the same speed, and in the same direction, as the rotor.

In rotating machines, even small unbalance may cause serious problems. The unbalance causes high bearing forces that are transmitted to the foundations and surrounding structures. The unbalance also causes high vibration amplitudes, and stresses, in the rotor. High vibration amplitudes are not allowed due to small clearances between the stator and the rotor. In the case of magnetic bearings, high force demand at high frequency causes power amplifier saturation, which leads to the deteriorating of the bearing characteristics and finally to instability; see Section 3.5.

The traditional way of solving the unbalance problem is mechanical balancing. This means installing balancing masses on the rotor or removing mass from the rotor. In the case of AMB, it is possible to handle the unbalance up to a certain limit with electronics. The synchronous bearing forces can be considerably reduced by the control system design, and consequently the rotor can be rotated practically around its axis of inertia. Actually, in subcritical applications AMB tolerates very high levels of unbalance. However, small clearances and the dynamic load capacity determine physical limits for the tolerated unbalance. If the unbalance goes beyond these limits, the rotor must be mechanically balanced. The use of AMB in mechanical balancing is discussed in Section 4.4.

Many kinds of methods have been developed for unbalance treatment in the AMB controller. The first idea is to use such a low controller gain at the frequencies belonging to the rotational speed range that the power amplifier would not become saturated. Unfortunately, this approach inevitably leads to soft bearings at low frequencies, as shown in Section 3.2. This is not acceptable in high-speed machines, because there exist considerable forces acting on the rotor at low frequencies.

The controller gain can also be dropped on a narrow frequency band near the rotational speed with a notch filter. This approach does not lead to the softening of the bearings at low frequencies. Because the notch filter is part of the position controller, it may deteriorate the bearing dynamics, or even lead to instability, as noted by Knospe (1991). However, a properly designed notch filter is known to behave well. To achieve good performance, and ensure stability, it is possible to use modern synthesis methods to achieve an effective controller with the demand of force cancellation, or rotor vibration cancellation. This has been successfully tested by Matsumura *et al.* (1996) and Mohamed and Busch-Vischniac (1995). To get rid of the rotational synchronous vibrations, it is also possible to build a special unbalance observer into the position controller. This approach has been tested by Matsumura *et al*. (1990) and Mizuno and Higuchi (1992).

All the previous methods are called closed-loop unbalance compensation methods, because the position controller is modified to achieve the preferred vibration cancellation effect. When properly used, all these methods work. However, there are some drawbacks. First, the controller parameters must be continuously updated when the rotational speed is changing. Furthermore, the design of a robust position-control loop with the requirement of force cancellation is more difficult than the design without this requirement. So, the synthesis and analysis of the position control loop becomes difficult. Also, as the vibration cancellation is an inherent part of the position control loop, the unbalance compensation is working all the time. In certain situations, the freezing of the compensation algorithm might be necessary.

For these reasons, the most popular way of unbalance treatment is the adaptive open-loop method, also called feedforward compensation. Such rotational synchronous signals are inserted into the controller that will eliminate the rotational synchronous control action. If the system is linear, these signals do not affect the stability. In practice, these compensation signals must be updated based on the measured synchronous vibrations. That is why the method is called adaptive. Because of this updating, the stability is no longer guaranteed. The problem of stability is further complicated by the fact that the influence of the compensation signals on the signals to be affected changes as a function of rotational speed and parameter variations. Thus, it may be difficult to find an algorithm that will work satisfactorily in all operational conditions.

A big advantage of the open loop-method is that the adapting process can be frozen, for example, when running in a risky speed range, and the compensation signals are working

purely as external disturbance and have no effect on the stability. A further advantage is that the difficult problem of building a good position-control loop with effective force cancellation is separated into two simpler problems.

Haberman and Brunet (1978) realized a simple and effective way of unbalance treatment. In their method, the position error signals are transformed into rotating coordinates. These error signals in rotating coordinates are integrated, and correction signals in opposite phase are inserted into the position signals until the vibration in the position error signal vanishes.

More commonly, no transformation to the rotating coordinates is done: Larsonneur (1990), Herzog *et al*. (1996), Beale *et al*. (1995), Knospe *et al.* (1995), Higuchi *et al*. (1992). The synchronous components of the error signals are measured and synchronous compensation signals are added to the electronics. The effect of the compensation signals on the error signals can be described with an influence coefficient matrix. The new compensation signals are related to previous measurements by a feedback matrix. The problem is that the influence coefficient matrix varies with rotational speed and machine parameters.

To make the system free of tuning, the influence coefficients could be estimated on-line: Burrows *et al.* (1989), Kanemitsu *et al*. (1990), Chen and Ku (1991), Knospe *et al*. (1995). This is very attractive because very little information of the system dynamics would be needed. Actually, an on-line estimation algorithm is not free of tuning. Rather, the user should define some parameters to adjust the excitation level and the confidence to new measurements, possible cautiousness, etc. In the author's experience, with high speed machines, the on-line estimation has turned out to be too slow to follow the rapid changes caused by fast accelerations and decelerations.

If no on-line estimation is used, the designer should compute a feedback matrix, or a small number of matrices, that will operate in a sufficient wide speed range and tolerate the parameter variations. Knospe *et al*. (1996,1997a,1997b) have studied this problem using the methods of modern system theory. They have created and tested a very general framework of analyzing and synthesizing the unbalance compensation system in the presence of structured uncertainties and certain performance demands. Using these methods, the unbalance compensation problem can be generally solved.

Higuchi *et al*. (1992) have proposed that the inverse of the influence coefficient matrix could be used as a feedback matrix. This would lead to fast convergence of the error signal. Unfortunately, the influence coefficient matrix is a function of rotational speed and other

parameters. Even though the algorithm tolerates a slightly incorrect estimate of the influence coefficient, the feedback coefficient must be stored for quite many speeds to maintain the advantage of fast convergence. Also, the robustness with respect to parameter variations other than the rotational speed is not guaranteed.

Herzog *et al*. (1996) have argued that in a properly designed subcritical AMB system, a diagonal feedback matrix with equal diagonal elements would work well. A simple method for obtaining this coefficient was proposed. Actually, the author has come to the same conclusion and the method presented in Section 4.3 differs only in that it is a discrete-time version of their method.

Even though there are potential sources of higher harmonic vibrations, the main problem is usually the first harmonic. Basically, there are no difficulties in constructing unbalance compensation for higher harmonics too, as shown by Kim and Lee (1997). An adaptive waveform memory (Bichler 1990) is also a possible solution to handle the higher harmonics. In this publication the system is assumed square, i.e. as many inputs as outputs. There are, however, no considerable difficulties in dealing with non square systems, usually with more measurements than compensation signals. This is studied by Burrows *et al*. (1989) and Knospe *et al.* (1995, 1996,1997a).

The preceding literature review reveals that the problem of unbalance compensation is already widely studied. The method proposed in this publication is a simple version of the adaptive open-loop method, also proposed by Herzog *et al*. (1996). However, it has been shown that this method generally works in the case of subcritical AMBs. With a couple of different feedback coefficients the method works in the whole speed range where the unbalance compensation might be necessary. A complex feedback coefficient can be used at the rigid-body resonance speeds and a real coefficient works well after the rigid-body resonances. The properties of this method are analyzed using the generalized Nyquist diagram introduced in Section 3.3. It is shown that this method maintains stability with all the postulated parameter variations.

4.2 The synchronous signals

The unbalance can be interpreted as a generalized force rotating at the same speed as rotor Ω. Consequently, as the system is assumed to be linear, the unbalance gives rise to sinusoidal vibrations in the signals of the AMB system. In Figure 36 the measurement of the synchronous components and the construction of the synchronous compensation signals are shown. At this point we do not care what the measured signals are and where the compensation signals are inserted.

Some signals $\mathbf{y}(t)$ are measured from the AMB system. To influence the synchronous vibrations in $\mathbf{y}$, we have controls $\boldsymbol{u}(t) = \mathrm{Re}\left(\boldsymbol{u}_S e^{i\gamma}\right)$, where $\boldsymbol{u}_S$ is a complex valued vector and γ is the phase angle. Actually, the cosine and sine of the phase angle are needed, and they are generated by a special sine-cosine-generator. This circuit measures the time distance of two previous phasor pulses, which are generated by a hall sensor detecting a hole in the rotor. Based on this period measure and the elapsed time from previous pulse, the sine-cosine-generator produces the sine and cosine waves. Note that the phase angle γ is not necessarily the rotor rotation angle β because the sine-cosine generator does not know the rotational direction. So, we only know that $\dot{\gamma} = |\Omega|$.

The linear system between $\boldsymbol{u}$ and $\boldsymbol{y}$ is expressed as a transfer function matrix $\boldsymbol{G}_\Omega(s)$, $\boldsymbol{y}(s)=\boldsymbol{G}_\Omega(s)\boldsymbol{u}(s)$. The subscript Ω emphasizes the fact that the system dynamics is a function of the rotational speed, as well as of the rotation direction. The synchronous components $\boldsymbol{y}_S$ are measured by multiplying the measured time domain signals $\boldsymbol{y}(t)$ by $e^{-i\gamma}$ and pushing the result through a low-pass filter $\boldsymbol{G}_L(s)$ and finally multiplying the signals by 2.

In the block diagram of the synchronous system, shown in Figure 36, there exist a number of complex valued signals. In the analysis of the synchronous signals, the complex signals are more convenient than pairs of real signals due to their clear physical meaning. A complex variable carries the amplitude and phase information in one packet. Further, the size of the influence coefficient matrix will be half of that with real variables, and it is simply the frequency response matrix of the system between compensations and measured variables. This simplifies the robustness analysis, as noted by Knospe *et al*. (1997a). The use of complex variables in dealing with unbalance compensation is a common practice; see also Kanemitsu *et al*. (1990) and Beale *et al*. (1995).

At this point it should be noted that the unbalance compensation can be realized without the phasor pulse. Beale *et al*. (1995) have proposed a special frequency tracking system which provides the speed information. Another idea is to use the position signals as a phasor pulse. This will work at high speeds, where the bearing force has no significant effect on the rotor orbit. However, if the external phasor pulse is not available, it is very difficult to draw conclusions about the stability, rate of convergence and the robustness. Also, an external phasor pulse provides the absolute rotation angle information, which is necessary when AMB is used for mechanical balancing. So, in this publication the phasor pulse is assumed to be available.

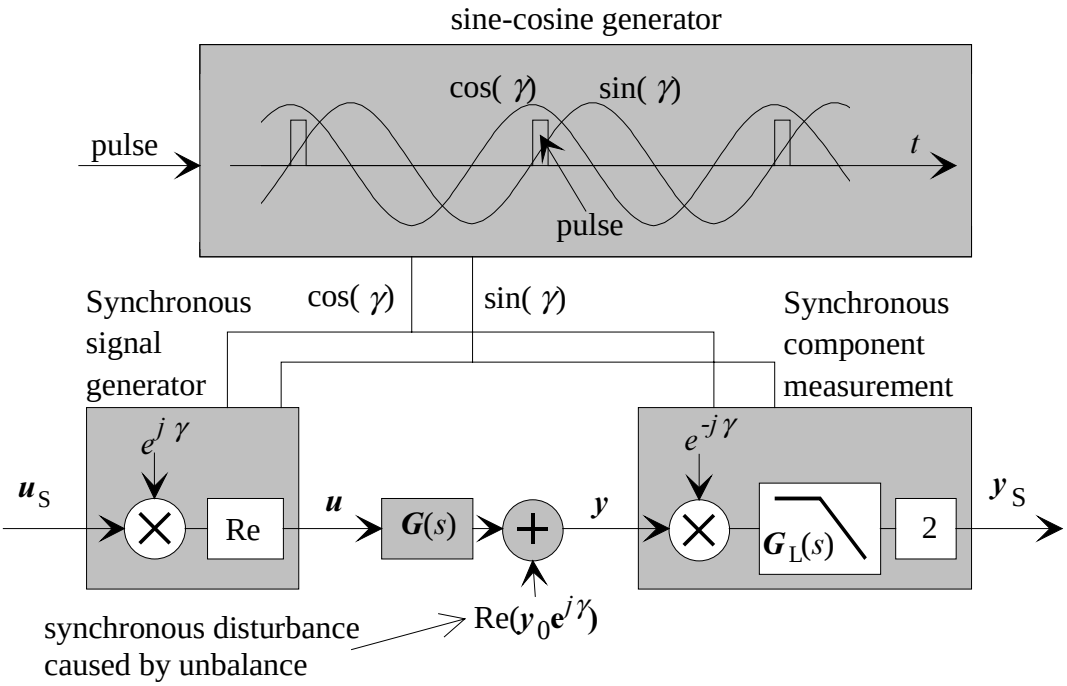

Figure 36. The synchronous system. Synchronous signal generation and synchronous component measurement.

Starting from zero initial conditions, the output $\boldsymbol{y}_S$ is obtained in the Laplace domain

$$\begin{aligned}\boldsymbol{y}_S(s) = \mathrm{L}\left[\boldsymbol{y}_S(t)\right] = \boldsymbol{G}_L(s)\boldsymbol{G}_\Omega\left(s+j|\Omega|\right)\left[\boldsymbol{u}_S(s)+\boldsymbol{u}_S^*\left(s+j2|\Omega|\right)\right]+ \\ \boldsymbol{G}_L(s)\left[\boldsymbol{y}_0(s)+\boldsymbol{y}_0^*\left(s+j2|\Omega|\right)\right],\end{aligned} \tag{37}$$

where * means taking the complex conjugate of the elements. The second harmonic, i.e. the signals vibrating at frequency $2|\Omega|$, is due to the fact that only real parts of the signals can be fed into the system. This is also the physical explanation for multiplying the synchronous

component measurements by 2. To get rid of this vibration, the damping of the low pass filter must be high enough at two times the rotational speed. In the author's test apparatus, the low pass filter is a diagonal transfer function matrix with diagonal elements

$$G_{\mathrm{L}}(s) = \frac{(2\pi 5)^2}{s^2 + 1.41(2\pi 5)s + (2\pi 5)^2} \,. \tag{38}$$

This filter has 50 dB damping at 100 Hz. When a step is inserted to the low pass filter, the output will settle within 5 % of the final value in 0.1 s.

When the disturbance and the compensation signals are held constant, the second harmonic vibrations are neglected and a "sufficiently long" time has elapsed, then the output will settle to a constant value

$$\boldsymbol{y}_{\mathrm{S}} = \lim_{s\to 0}\left[s\boldsymbol{y}_{\mathrm{S}}(s)\right] = \boldsymbol{G}_{\Omega}\left(j|\Omega|\right)\boldsymbol{u}_{\mathrm{S}} + \boldsymbol{y}_0 \,, \tag{39}$$

where $\boldsymbol{G}_{\Omega}\left(j|\Omega|\right)$ is called the influence coefficient matrix. The question arises of what is a sufficiently long time for Equation 39 to hold. Obviously, the minimum (0.1 s) is defined by the low-pass filter. If the system $\boldsymbol{G}_{\Omega}$ has poles near $j|\Omega|$ then the settling time can be longer. In this case the synchronous system is no longer static, but becomes dynamic. This might be the case near the structural modes of the rotor or the stator.

Let us analyze what the settling time of the synchronous measurements is, if the system $\boldsymbol{G}_{\Omega}\left(s + j|\Omega|\right)$ has one pole near the origin, i.e. system $\boldsymbol{G}_{\Omega}(s)$ has a pole near $-j|\Omega|$. Let us assume that the synchronous measurement is originally 1, and the step in the compensation signal is such that the final value of the synchronous signal is 0. The step response of this third-order system is simulated in the time domain for different pole locations. After 0.1 s the response remains inside a circle with a certain radius, called the settling radius. The settling radius is computed for many pole locations. In Figure 37, the pole locations where the radius after 0.1 s is 0.1, 0.2 and 0.3 are shown. The same is done for 0.2 s.

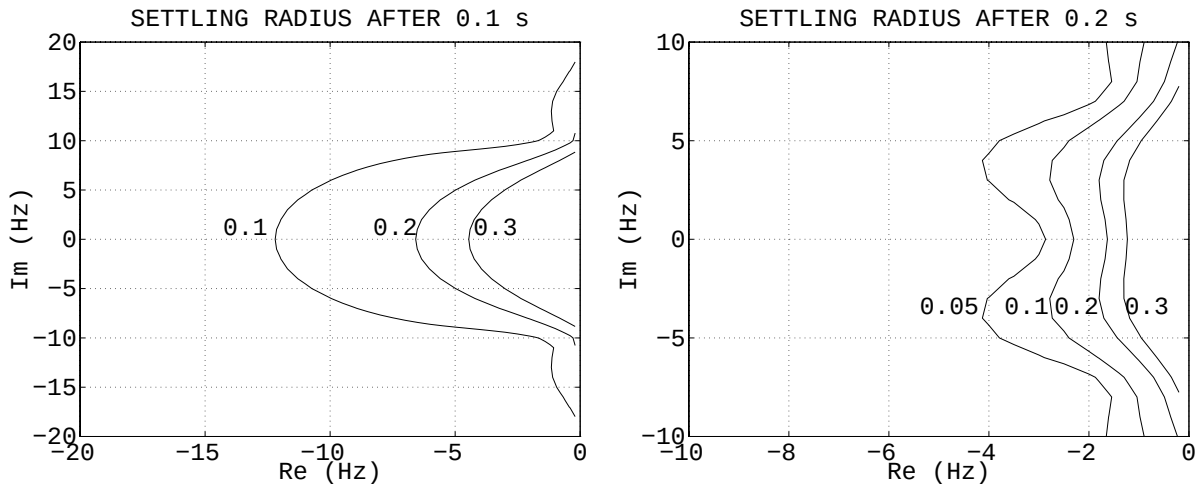

Figure 37. The settling radius after 0.1 s and 0.2 s, when the system has a pole near the rotational frequency.

As can be seen, the synchronous measurement does not actually settle within 0.1 s when the system has a pole near the rotational frequency. However, the pole must be very near the imaginary axis to cause problems. Later, in Section 4.3, it is shown that even though the system does not actually settle in 0.1 s, it has no big effect on the stability of the proposed unbalance compensation method. Therefore, 0.1 s is used as an update interval and Equation 39 is supposed to hold after one update interval.

The unbalance compensation tries to eliminate the synchronous vibration in $\boldsymbol{y}$. Assume that the new compensation is computed as follows

$$\boldsymbol{u}_{\mathrm{S}}(n+1) = \boldsymbol{u}_{\mathrm{S}}(n) - \boldsymbol{K}_{\mathrm{unb}}\boldsymbol{y}_{\mathrm{S}}(n)\,, \tag{40}$$

where $\boldsymbol{K}_{\mathrm{unb}}$ is called unbalance the compensator feedback matrix. Then

$$\boldsymbol{y}_{\mathrm{S}}(n+1) = \left[\mathbf{I} - \boldsymbol{G}_{\Omega}\left(j|\Omega|\right)\boldsymbol{K}_{\mathrm{unb}}\right]\boldsymbol{y}_{\mathrm{S}}(n)\,. \tag{41}$$

So, the synchronous vibration vanishes if the eigenvalues of $\left[\mathbf{I} - \boldsymbol{G}_{\Omega}\left(i|\Omega|\right)\boldsymbol{K}_{\mathrm{unb}}\right]$ are inside a unit circle. Actually, it is not good enough that the system is stable, but it should also converge fast enough. The error signals at least should steadily diminish (measured by largest singular value, for example). Otherwise, it is dangerous to start the compensation. Thus, a further demand is that the largest singular value of the matrix $\left[\mathbf{I} - \boldsymbol{G}_{\Omega}\left(i|\Omega|\right)\boldsymbol{K}_{\mathrm{unb}}\right]$ should

remain below a certain limit, at least below 1. This largest singular value is called the decrement.

The effect of different compensation strategies

Before stating the compensation algorithm, let us study the effect of different compensation strategies on the AMB forces, vibration amplitudes, control currents and voltages. The five different cases are listed in Table 1.

Table 1. Different compensation strategies.

Number and reference in Figure 38	Synchronous vibration canceled in
1	bearing force
2	control voltage
3	control current reference
4 (--)	position signal
5 (bold line)	no compensation

Strategies 1-3 aim to cancel the bearing force, strategy 4 eliminates the vibration in the position signals, i.e. rotation around the geometrical axis, and the case without compensation is computed for reference. In Figure 38 the bearing force, vibration in displacement sensor locations, control voltage and control current are computed for the 2-end bearing. Assumed unbalance is 800 gmm in planes 1 and 3 and they have 90° phase shift. In this simulation the motion voltage term and coil resistance are taken into consideration. The parameters are obtained with nominal air gap and zero force (h_{f00}=340 N/A, c_{00}=1.8*106 N/m, L_{dyn00}=42 mH, h_v=170 N/A, r=1 Ω).

First of all, a complete force cancellation is difficult to achieve because there is no direct bearing force measurement in a conventional AMB system. The force cancellation strategy “1” is therefore considered as a reference curve only. Best force cancellation is achieved by voltage compensation “2”. This is physically obvious because the control voltage is closely related to the air gap flux time derivative, which is proportional to the bearing force time derivative. Due to coil resistance and leakage fluxes, the force is not completely eliminated. When the control current vibration is eliminated, strategy “3”, the position stiffness effect remains and the bearing force is clearly higher than in the voltage compensation “2”.

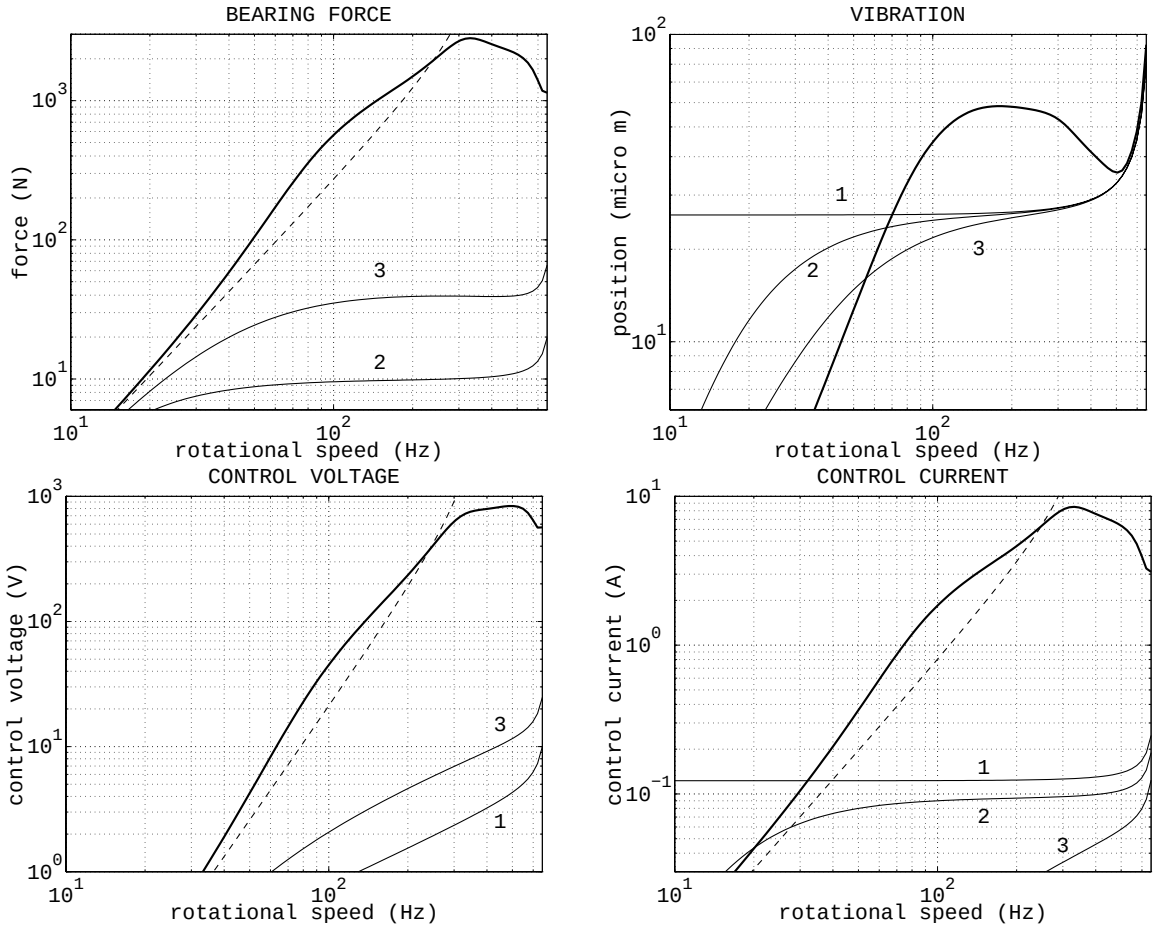

Figure 38. The effect of different compensation strategies on the AMB signals. The curves represent the amplitude of the rotational synchronous vibration of the 2-end X direction.

An interesting observation is that at low frequencies, below 220 Hz in this case, the position compensation, strategy "4", leads to a smaller bearing force than the uncompensated situation. If the controlled bearing force needed to eliminate position vibration is $\boldsymbol{F}_{\text{Sbcur4}}$, then the controlled bearing force without compensation is $\boldsymbol{F}_{\text{Sbcur}} = \boldsymbol{T}_{\Omega\text{F}}\left(j|\Omega|\right)\boldsymbol{F}_{\text{Sbcur4}}$ where $\boldsymbol{T}_{\Omega\text{F}}\left(j|\Omega|\right) = \left[\mathbf{I} + \boldsymbol{L}_{\Omega\text{F}}\left(j|\Omega|\right)\right]^{-1}\boldsymbol{L}_{\Omega\text{F}}\left(j|\Omega|\right)$ is the complementary sensitivity function at the plant input, i.e. at the bearing force. Whether the bearing force in the uncompensated case is smaller or bigger than in the position compensation depends on the singular values of this complementary sensitivity function. In Appendix A, it is shown that when some part of the numerical range of $\boldsymbol{L}_{\Omega\text{F}}$ is to the left of the line Re(z)=-1/2, then the largest singular value of $\boldsymbol{T}_{\Omega\text{F}}$ is larger than 1. As the system is open-loop unstable, some of the eigenloci of $\boldsymbol{L}_{\Omega\text{F}}$ must encircle point -1. What follows is that at some frequencies, the numerical range may not be to the right of the line Re(z)=-1/2, and the bearing force must be higher than the position

compensated bearing force at least for some signal directions. In practice, the numerical range will be clearly to the left of the line Re(z)=-1/2 at low frequencies and consequently the bearing force increases in all signal directions. Thus, at low speeds it is safe to switch to position compensation because the bearing forces, voltages and currents will decrease. At higher frequencies there is a risk of power amplifier saturation if the position compensation is started.

Another nontrivial observation is that at a certain speed range, 70 Hz -> 500 Hz in the present case, the force elimination, strategies 1-3, decreases the vibration amplitude. Let $\boldsymbol{p}_{\mathrm{SS3}}$ be the vibration amplitude when strategy "3" is used and $\boldsymbol{p}_{\mathrm{SS}}$ is the vibration amplitude without compensation. These are related as $\boldsymbol{p}_{\mathrm{SS3}} = \left(\mathbf{I} + \boldsymbol{L}_{\Omega\mathrm{p}}\right)\boldsymbol{p}_{\mathrm{SS}}$. Thus, even if the unbalance compensation is not necessary for reducing the bearing forces, it can be used to decrease the vibration amplitudes. This could be necessary when the minimum singular value of $\left(\mathbf{I} + \boldsymbol{L}_{\Omega\mathrm{p}}\right)$ is less than 1, i.e. the numerical ranges of $\boldsymbol{L}_{\Omega\mathrm{p}}$ penetrate inside a unit circle centered at -1.

For the test machine, the vibration amplitude with strategy "3" increases steadily from zero to a value corresponding to force-free rotation, strategy "1", as the rotational speed increases. Ahrens *et al*. (1996) have noticed that the situation is essentially different in the case of a highly gyroscopic rotor. If the synchronous component at the position controller output vanishes, then there will appear an undamped resonance caused by a rigid-body nutation mode and position stiffness. At the resonance speed the vibration amplitudes increase above all limits, so the compensation strategies "2" and "3" cannot be used near the resonance speed. Fortunately, for this situation to occur, the ratio between the axial mass moment of inertia and the radial mass moment of inertia must be higher than 1. In the high-speed machines considered in this publication, the ratio is typically less than 1/10 and this effect does not exist.

4.3 The proposed compensation method

The voltage compensation, strategy "2" in the previous section, would lead to the best force cancellation. Also, the main problem, i.e. amplifier saturation, would be perfectly solved. The problem with voltage compensation is that these signals are not necessarily available in an AMB system. Also, practical aspects, like the pulsating electric motor disturbance force,

decrease the theoretical advantage achieved from the voltage compensation. Furthermore, the behavior of the control voltage depends heavily on the dynamic inductance, which has large variation. Therefore, it would be difficult to make a robust voltage compensation algorithm. For these reasons, the compensation in the reference current , strategy “3”, was chosen.

A very simple version of the adaptive open-loop method is shown in Figure 39. The feedback matrix $\boldsymbol{K}_{\mathrm{unb}}$ in Equation 40 is reduced to a scalar k_{unb}. In this section, this algorithm is studied.

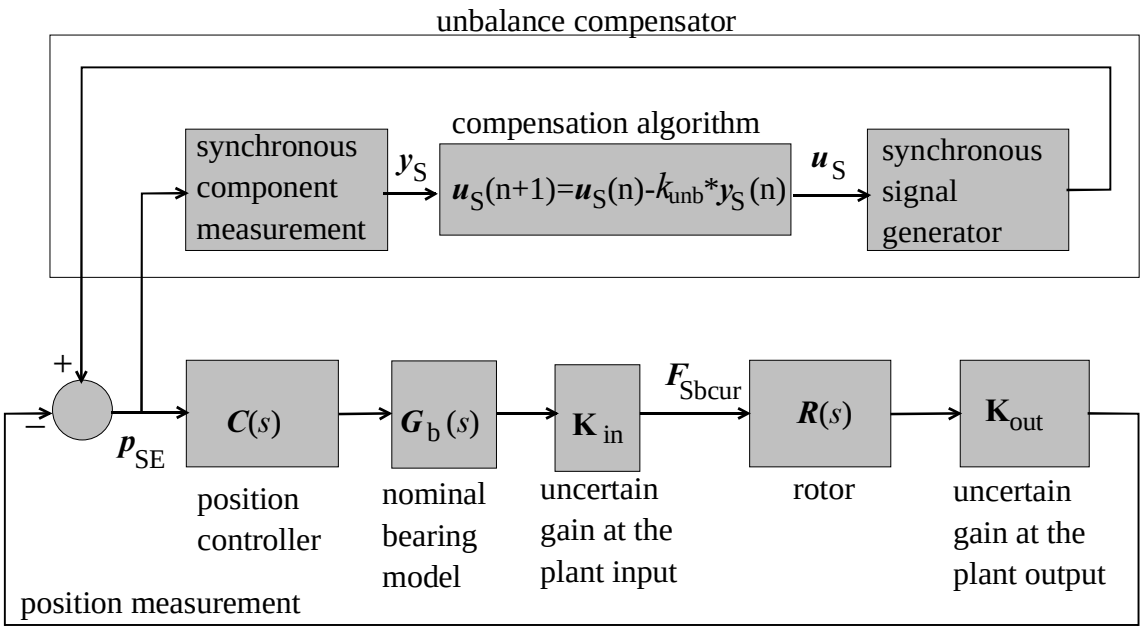

Figure 39. Simple unbalance compensation.

The unbalance compensator eliminates the rotational synchronous vibration in the position controller input and output. Thus, it realizes strategy “3” of the previous section. The synchronous component in the controlled bearing force $\boldsymbol{F}_{\mathrm{Sbcur}}$ behaves as

$$\begin{aligned} \boldsymbol{F}_{\mathrm{Sbcur}}(n+1) &= \left[\mathbf{I} - k_{\mathrm{unb}}\left(\mathbf{I} + \boldsymbol{L}_{\Omega\mathrm{F}}\right)^{-1}\right]\boldsymbol{F}_{\mathrm{Sbcur}}(n)\,, \\ \boldsymbol{L}_{\Omega\mathrm{F}} &= \boldsymbol{K}_{\mathrm{in}}\boldsymbol{L}_{\Omega\mathrm{F0}}\,,\ \boldsymbol{L}_{\Omega\mathrm{F0}} = \boldsymbol{G}_{\mathrm{b}}\left(j|\Omega|\right)\boldsymbol{C}\left(j|\Omega|\right)\boldsymbol{K}_{\mathrm{out}}\boldsymbol{R}\left(j|\Omega|\right). \end{aligned} \tag{42}$$

The reason for studying the system behavior at the controlled bearing force rather than at some other place of the feedback loop is explained later. The controlled bearing force

converges to zero if the eigenvalues of matrix $\mathbf{I}-k_{\text{unb}}\left(\mathbf{I}+\boldsymbol{L}_{\Omega\text{F}}\right)^{-1}$ are inside the unit circle. Eigenvalues of this matrix depend on the open-loop eigenvalues $\lambda_n\left[\boldsymbol{L}_{\Omega\text{F}}\right]$ as

$$\lambda_n\left[\mathbf{I}-k_{\text{unb}}\left(\mathbf{I}+\boldsymbol{L}_{\Omega\text{F}}\right)^{-1}\right]=\frac{\left(1-k_{\text{unb}}\right)+\lambda_n\left[\boldsymbol{L}_{\Omega\text{F}}\right]}{1+\lambda_n\left[\boldsymbol{L}_{\Omega\text{F}}\right]}=\frac{\lambda_n\left[\boldsymbol{L}_{\Omega\text{F}}\right]-\left(-1+k_{\text{unb}}\right)}{\lambda_n\left[\boldsymbol{L}_{\Omega\text{F}}\right]-(-1)} \tag{43}$$

Thus, all the eigenvalues of the open loop $\boldsymbol{L}_{\Omega\text{F}}$ must be closer to point -1+k_{unb} than to point -1 in the complex plane. Accordingly, the unbalance compensation is stable if the open-loop eigenvalues are on the dark half-space shown in Figure 40. This is the necessary and sufficient condition for nominal stability. However, we are more interested in the robust stability and performance. Thus, in the analysis, we draw the numerical range of $\boldsymbol{L}_{\Omega\text{F0}}$ and require that the whole numerical range is on the correct half-space.

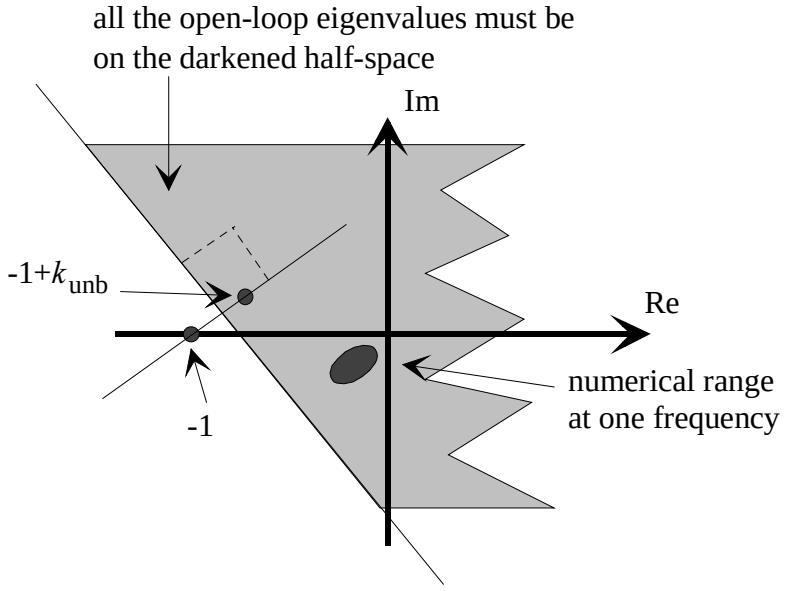

Figure 40. Unbalance compensation stability analysis with open-loop eigenvalues.

The requirement that the whole numerical range is on the correct half-space is, of course, a slightly conservative condition concerning stability. However, it can be shown (see Appendix A) that this is actually the necessary and sufficient condition for the largest singular value of $\left[\mathbf{I}-k_{\text{unb}}\left(\mathbf{I}+\boldsymbol{L}_{\Omega\text{F0}}\right)^{-1}\right]$, i.e. decrement, to be less than 1. In other words, if the whole numerical

range is not on the correct half-space, then the biggest singular value is greater than 1, and the error vector will momentarily rise, measured by 2-norm when the unbalance compensation is started with some initial conditions. This is undesirable, because the power amplifier may become saturated during the overshoot. So, the demand that the whole numerical range is on the right side is a kind of necessary and sufficient minimum nominal performance requirement. This is also the reason why we study the compensator behavior in the control force rather than at the position error signal.

Robust stability can be determined by checking whether the numerical ranges divided by the members of the uncertainty region $\phi(\boldsymbol{K}_{\text{in}})$ go into the forbidden half-space or not. For that purpose the following curve is constructed: For every point z in the boundary line a region $z\phi(\boldsymbol{K}_{\text{in}})$ is drawn into the generalized Nyquist diagram. The envelope on the allowed half space is the boundary curve for robust stability. Robust stability is obtained if the whole numerical range is on the correct side of this curve.

The robust stability condition does not guarantee that the decrement is less than 1. However, if the matrix $\boldsymbol{K}_{\text{in}}$ is diagonal with real diagonal elements then we can determine the robust performance at the midpoint of $\boldsymbol{K}_{\text{in}}$, as shown in Appendix A. Because the assumed uncertainty is “almost diagonal” and “almost real” we can expect that the decrement will not be much higher than 1 if the robust stability condition is fulfilled.

Let us draw the numerical ranges for $\boldsymbol{L}_{\Omega\text{F0}}$ at several speeds. Assume 10 % sensor sensitivity error. This uncertainty is taken into consideration in a similar manner as in Section 3.4. The simple bearing model, Equation 22, is used, i.e. the motion voltage and coil resistance are neglected. The unstructured version of the generalized Nyquist diagram is drawn in Figure 41 with the bounding line and constant decrement curves for $k_{\text{unb}} = 0.2e^{-j90^\circ}$ and k_{unb}=0.2. As noted earlier in Section 4.2, the unbalance might be necessary when the numerical ranges penetrate inside a unit circle centered at -1. That happens at approximately 50 Hz as shown on the left-hand side of Figure 41. As can be seen, the complex parameter $k_{\text{unb}} = 0.2e^{-j90^\circ}$ should maintain robust stability from 50 Hz up to 100 Hz. From about 225 Hz up to maximum speed, the real parameter k_{unb}=0.2 guarantees robust stability. A third parameter $k_{\text{unb}} = 0.2e^{-j60^\circ}$ is used in the speed range from 100 Hz to 225 Hz to maintain robust stability.

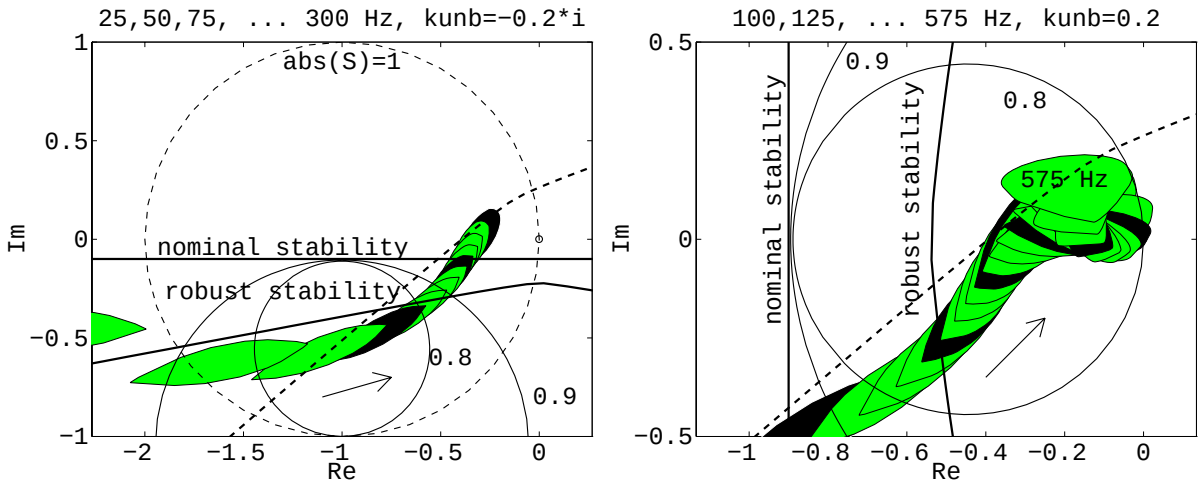

Figure 41. Unbalance compensation robustness analysis. At low speeds the complex feedback coefficient $k_{\text{unb}} = 0.2e^{-j90^\circ}$ works well and at the higher frequencies k_{unb}=0.2 is good. The dashed curves represent the robust stability border for $k_{\text{unb}} = 0.2e^{-j60^\circ}$. The solid circles show the constant decrement curves.

In Section 3.4, it was seen that the shape of the generalized Nyquist curve is very generally that seen in Figure 41. Therefore, the previously described parameters should generally work very well. The speeds where the parameter value is changed depend on the application. These speeds can be easily determined from the Generalized Nyquist diagram.

About the backward whirling

As noted in Section 2.3, near the unsupported bending critical speeds, bearing force is needed to limit the vibration amplitudes. Consequently, compensation signals must be frozen when passing these speeds. There are, however, speeds called backward critical speeds where the rotational speed equals the eigenfrequency of a backward-rotating bending mode. When the rotor starts rotating, the bending mode vibrating on a plane splits into forward- and backward-rotating modes. The eigenfrequency of the forward mode increases and the eigenfrequency of the backward mode decreases as the rotational speed increases. In the subcritical high-speed machines the maximum rotational speed is sometimes near the first backward critical speed.

The unbalance force rotates in the same direction as the rotor and does not excite the backward mode. Thus, it should be possible to rotate the rotor at the backward critical speed even though the passing of the first bending critical speed would be clearly impossible. So, it is worth studying how the proposed unbalance compensation behaves near this backward critical speed. The maximum speed of the test machine is 540 Hz, i.e. clearly below the first

backward critical speed, which is 620 Hz. However, let us use this machine as an example. The numerical ranges of $\boldsymbol{L}_{\Omega F0}$ near the speed of 620 Hz are shown in Figure 42.

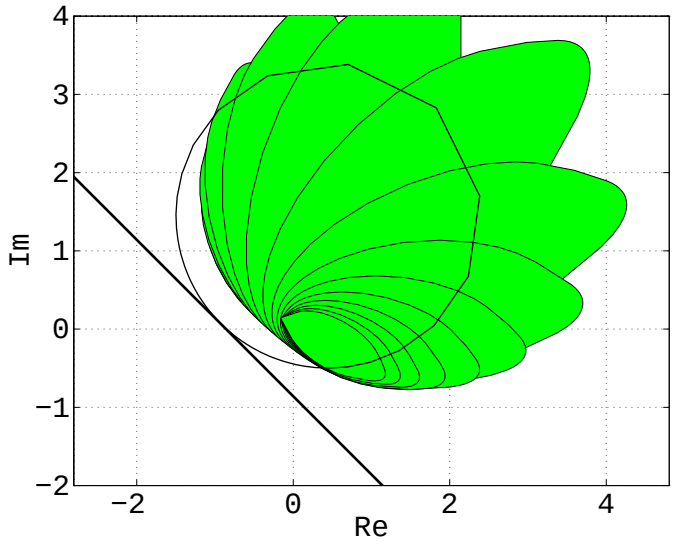

Figure 42. Behavior of the unbalance compensation near the backward critical speed. The speeds are near 620 Hz. The stability border is computed for $k_{\text{unb}} = 0.2e^{j45^\circ}$, and the decrement in the circle is 0.95.

Even if the system remains stable with a properly chosen k_{unb}, the decrement is poor in certain signal direction, corresponding to the backward-rotating bending mode. If the machine should be driven near the backward critical speed, special attention has to be paid to this speed range.

The solution to this situation is to modify the proposed algorithm so that the compensator is only able to generate a forward-rotating compensation signal. This means that the compensation signals in X and Y directions have equal magnitude and a phase shift of 90°. In this algorithm, the rotation direction should be known. Also, the analysis of this system will be more difficult than the previous analysis and such elegant and powerful robustness results are not easy to achieve. It is relatively easy to make statements of the system when it is totally symmetric, i.e. the X and Y directions have the same bearing properties. The asymmetries, however, make this analysis quite elaborate and it is not considered here further. This algorithm would be close to that proposed by Haberman and Brunet (1978).

The effect of the poles near the rotational frequency

So far, it has been assumed that the Equation 39 is valid, i.e. when the compensation signals are changed, the synchronous measurements have settled to the final value at the next sampling instant. As seen in Figure 37, this is not actually the case even if there was no poles near the rotational frequency. Let us now analyze the effect of the settling error on the stability of this algorithm.

Assume that the synchronous measurements settle to the final value in two sampling periods. Then the synchronous system can be described by the following difference equations

$$\begin{aligned} \boldsymbol{p}_{\mathrm{SE}}(n+1) &= \boldsymbol{p}_{\mathrm{SE0}} + [\mathbf{I}-\boldsymbol{X}]\left[\mathbf{I}+\boldsymbol{L}_{\Omega\mathrm{p}}\right]^{-1}\boldsymbol{u}_{\mathrm{S}}(n) + \boldsymbol{X}\left[\mathbf{I}+\boldsymbol{L}_{\Omega\mathrm{p}}\right]^{-1}\boldsymbol{u}_{\mathrm{S}}(n-1)\,, \\ \boldsymbol{u}_{\mathrm{S}}(n) &= \boldsymbol{u}_{\mathrm{S}}(n-1) - k_{\mathrm{unb}}\boldsymbol{p}_{\mathrm{SE}}(n)\,, \end{aligned} \tag{44}$$

where $\boldsymbol{p}_{\mathrm{SE}}$ is the measured synchronous component in the position error,
$\boldsymbol{p}_{\mathrm{SE0}}$ is the synchronous component in the position error without compensation,
$\boldsymbol{X}$ is the error matrix,
$\boldsymbol{L}_{\Omega\mathrm{p}}$ is the frequency response matrix of the open-loop cut at the plant output.

This corresponds to the block diagram shown in Figure 43.

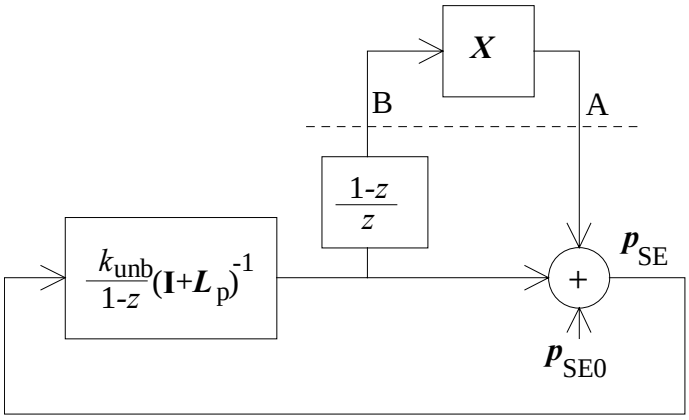

Figure 43. A block diagram illustrating the effect of a settling error. The z in the diagram is the Z-transform variable.

Let $\boldsymbol{G}_{\mathrm{AB}}(z)$ be the pulse transfer function from point A to point B in Figure 43 when the system is cut in the shown line. Assume that there is only one pole near the rotational frequency. Then, $\boldsymbol{X}$ can be assumed scalar, x. If the phase of x can be anything but the absolute

value is limited below x_{max}, then the necessary and sufficient condition for robust stability is that the spectral radius of $\boldsymbol{G}_{AB}(z)$ remains below $1/x_{max}$ when z encircles the unit circle. If λ_L is an eigenvalue of $\boldsymbol{L}_{\Omega p}$ then the corresponding eigenvalue of $\mathbf{G}_{AB}(z)$ and its largest absolute value are

$$\lambda\left[\boldsymbol{G}_{AB}(z)\right] = \frac{k_{unb}(1-z)}{z\left[(z-1)\left(\lambda_L+1\right)-k_{unb}\right]},$$
$$\max_{|z|=1}\left|\lambda\left[\boldsymbol{G}_{AB}(z)\right]\right| = \left|\mathrm{Re}\left[\frac{\lambda_L-\left(-1+k_{unb}/2\right)}{k_{unb}}\right]^{-1}\right|. \quad (45)$$

Thus, the robust stability condition can be written as

$$\mathrm{Re}\left[\frac{\lambda_L-\left(-1+k_{unb}/2\right)}{k_{unb}}\right] > x_{max}\text{, for all } \lambda_L \in \rho\left(\boldsymbol{L}_{\Omega p}\right), \quad (46)$$

where $\rho\left(\mathbf{L}_{\Omega p}\right)$ is the set of eigenvalues of $\boldsymbol{L}_{\Omega p}$.

As the eigenvalues of $\boldsymbol{L}_{\Omega p}$ are equal to the eigenvalues of matrix $\boldsymbol{L}_{\Omega F}$, we may consider the eigenvalues of $\boldsymbol{L}_{\Omega F}$ instead in the following discussion. The robust stability condition, Equation 46, means that all the eigenvalues of the open-loop frequency response matrix $\boldsymbol{L}_{\Omega F}$ must be at the correct half space, shown in Figures 40 and 41, and the smallest distance to the border line must be at least $\left|k_{unb}x_{max}\right|$. When $\left|k_{unb}\right| = 0.2$ and $x_{max} = 0.2$, this distance is only 0.04. A more conservative condition is that the whole numerical range of $\boldsymbol{L}_{\Omega F}$ must be at least at this distance from the stability line. As shown in Figure 41, this condition is easily fulfilled with a reasonable design.

Even though lots of simplifying assumptions were made in the previous discussion, we can conclude that even a relatively large settling error is not dangerous considering the stability of the unbalance compensation algorithm. This is due to the small absolute value of the feedback coefficient k_{unb}.

Experimental testing

The unbalance compensation was applied to the test machine described in Appendix C. The used position controller is shown in Equation 34. In this subsection, some results from the experimental tests are presented. Unfortunately, the measured machine individual happened to have very small unbalance and therefore the results are not so impressive as they could be.

In Figure 44, the synchronous vibration in the control current and position signals are plotted with and without compensation. They are the synchronous components from the 2-end X direction. The unbalance compensation was started at 40 Hz. The feedback coefficient was $k_{\text{unb}} = 0.2\,e^{-j90^\circ}$ from 40 Hz to 100 Hz, $k_{\text{unb}} = 0.2\,e^{-j60^\circ}$ from 100 Hz to 200 Hz and 0.2 after that.

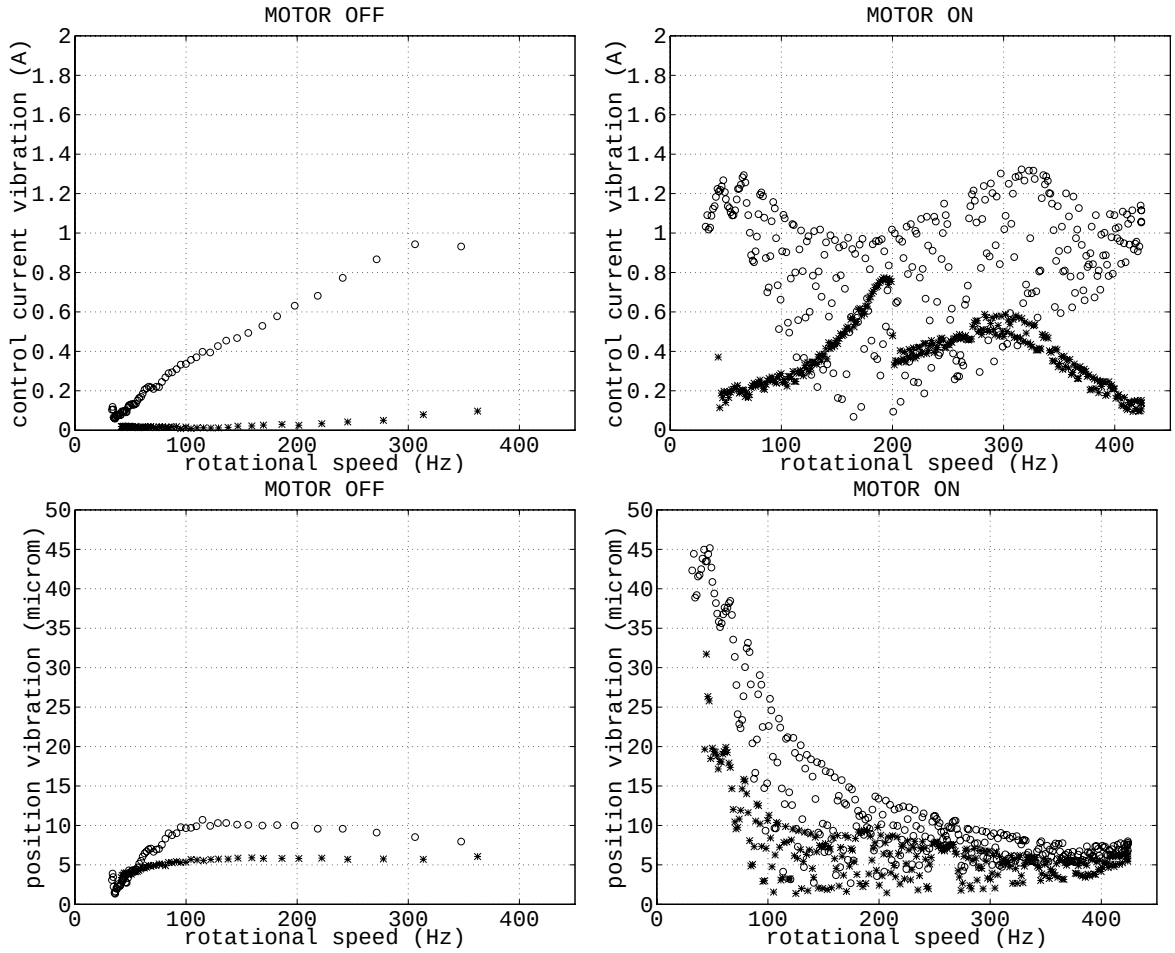

Figure 44. The absolute value of the synchronous vibration in the control current and position signal in 2-end X direction. The vibrations with compensation are labeled with asterisks (*) and without compensation with circles (o). On the left-hand side plots are the amplitudes when the motor is turned off and the machine is decelerating. On the right-hand side plots, the motor is on and the machine is slowly accelerating.

The curves on the left-hand side are measured during the deceleration when the motor was turned off. There are only a few samples at high speeds, because of the fast deceleration. The curves on the right-hand side are measured during the acceleration with the motor on. As seen, the electric motor causes a considerable increase in the vibrations, especially at low speeds. Let us first consider the left-hand side plots, where the electric motor is turned off, i.e. it causes practically no radial forces. Without compensation, the control current vibration increases steadily as the speed increases. With compensation, the control current vibration is practically zero. This measurement confirms that the unbalance compensation really also decreases the position vibration amplitudes from about 50 Hz. So, the effect of the unbalance compensation fits very well with the predictions in Section 4.2.

On the right-hand side plots the motor is on. As can be seen, the electric motor causes considerable radial forces, which increase the vibrations. The electric motor forces are rotating at the same speed as the magnetic field, i.e. slightly faster than the rotor, and the unbalance force. Thus, the unbalance force and electric motor force together produce a pulsating rotating radial force. As seen, the unbalance compensator is not able to totally eliminate the synchronous control current vibration. So, even though we have the unbalance compensator, there must not be peaks which are too high in the gain of the position controller in the rotational speed range. The importance of the decrement is clearly seen at the speed 200 Hz, where the feedback coefficient changes value to a better one. The current vibration decreases immediately because the compensation better follows the pulsating. At higher speeds, the pulsating frequency becomes so high that the algorithm can not follow it anyway. Even though the compensator does not totally eliminate the control current vibration, the vibration amplitude is clearly smaller than without compensation. The position vibration is also smaller throughout the whole speed range.

In Figure 45 the effect of unbalance compensation is measured at 380 Hz. The feedback coefficient is k_{unb}=0.2. The reference current at the 2-end X direction is shown. The pulsating caused by electric motor is clearly visible in the plot without compensation. The compensator decreases the vibration amplitude rapidly. However, a constant amplitude is left in the reference current, with negligible pulsating. This can be explained as follows: Under the pulsating force, the optimum compensation signal encircles a circle in the complex plane. The center of this circle is defined by the unbalance, and the radius of this circle is determined by the electric motor force. The speed of rotation is determined by the frequency difference

between the electric motor force and the unbalance force. Now, the compensation signals are not able to follow this optimum value, but track it somewhere inside the circle. After short time a steady-state situation is achieved where the distance between the optimum compensation signal and the tracking actual signal remains approximately constant. This means constant amplitude reference current vibration. When the electric motor is turned off, the vibration decreases to a low level, determined by the offsets, measurement noise, measurement resolution and compensation signal resolution.

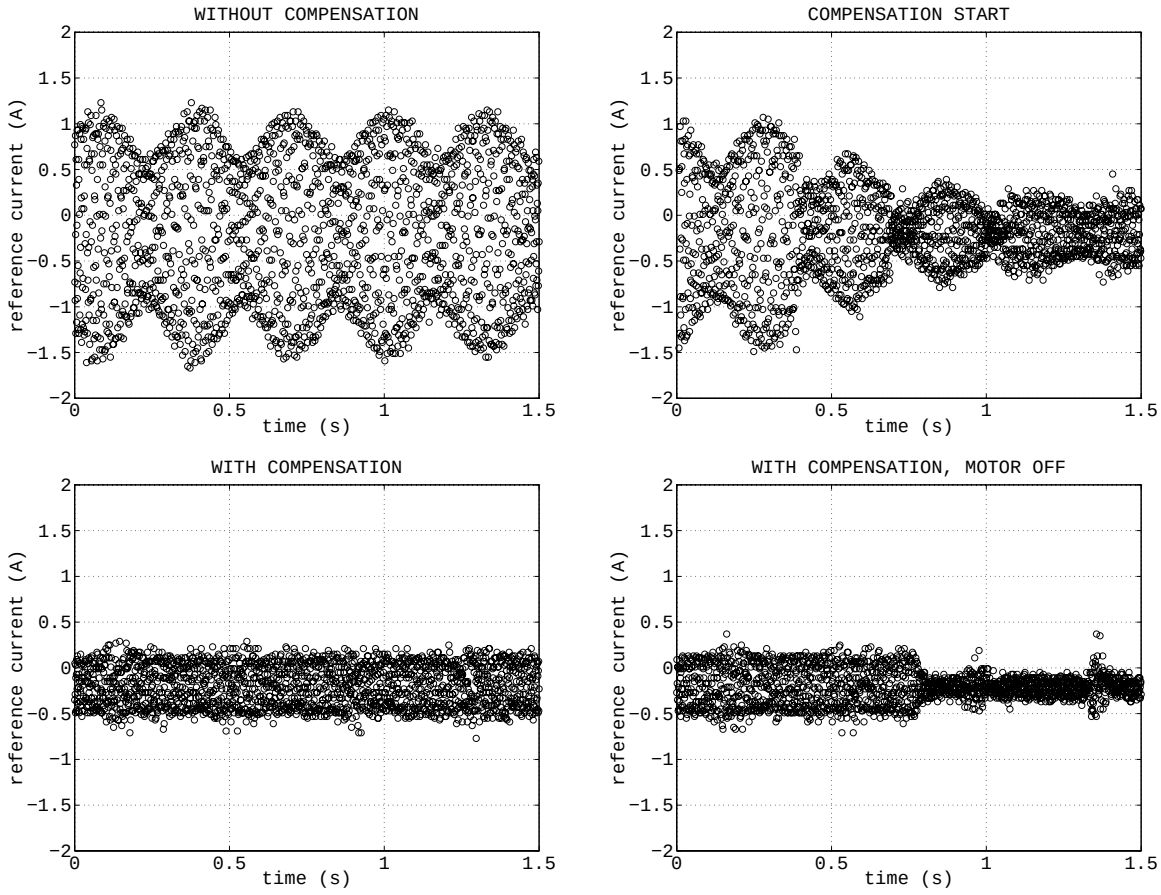

Figure 45. The behavior of the compensator at a speed of 380 Hz.

4.4 Mechanical balancing

In some cases the unbalance compensation alone does not solve the unbalance problem. If some bending critical speeds should be passed, the corresponding modal unbalances must be below certain limit, as noted in Section 2.3. Even in subcritical applications the rotor bending or rigid-body vibration may become intolerably high. In these cases the rotor must be

mechanically balanced, i.e. balancing masses must be installed into the rotor or mass must be removed. In the case of high-speed machines removing mass is more practical.

There are a number of balancing methods and different kinds of balancing machines presented in the literature (Schneider 1991). With these conventional balancing techniques, the rotor can be balanced to a sufficient level if only rigid body modes are important. Actually, when the unbalance compensation is available, the balancing requirements for a rigid rotor are very easy and often mechanical balancing is not needed at all.

If the rotor should be balanced with respect to bending modes, the situation is harder. To find the modal unbalance, the rotor must be rotated at such a high speed that the corresponding bending mode starts to deform. It may be difficult to find a balancing machine where a high-speed rotor could be rotated at that high speed. In such a case, the high-speed machine and the magnetic bearings can be used as a balancing machine. The data collected from magnetic bearings is used to compute the balancing masses.

The idea of using AMB as a balancing machine is not new. Higuchi (1988) has tested rigid rotor balancing based on the AMB force measurement. Ahrens *et al*. (1996) have used the AMB position signals to compute balancing masses for a flywheel energy storage system. In this machine as well, only the rigid-body modes were of interest. In their method, an unbalance compensation was used to eliminate the synchronous vibration in the bearing current. However, as they noted, the bearing force is not totally eliminated by the current vibration elimination. This fact, in addition to the unmodeled housing dynamics and highly gyroscopic rotor, led to errors in the unbalance estimation, and the iterative approach had to be employed. Mazzochetti *et al*. (1994) have also reported the use of AMB for balancing. They used a conventional “three run” method for balancing the rotor of a turbomolecular pump with respect to rigid body modes.

The rotors of the test machine were balanced at a low speed by a conventional balancing machine. Consequently, the unbalance associated with the rigid-body modes is negligible. The problem is the unbalance associated with the first bending mode. In some individual machines the bending was too high at the maximum rotational speed. So, three-plane balancing became necessary and AMB had to be used for balancing.

The balancing method

The estimation of the unbalance is based on the displacement measurements, not the bearing forces. That is because the position sensor sensitivity is known accurately but the bearing force is not. The measurement of the synchronous components of the position signals is shown in Figure 46.

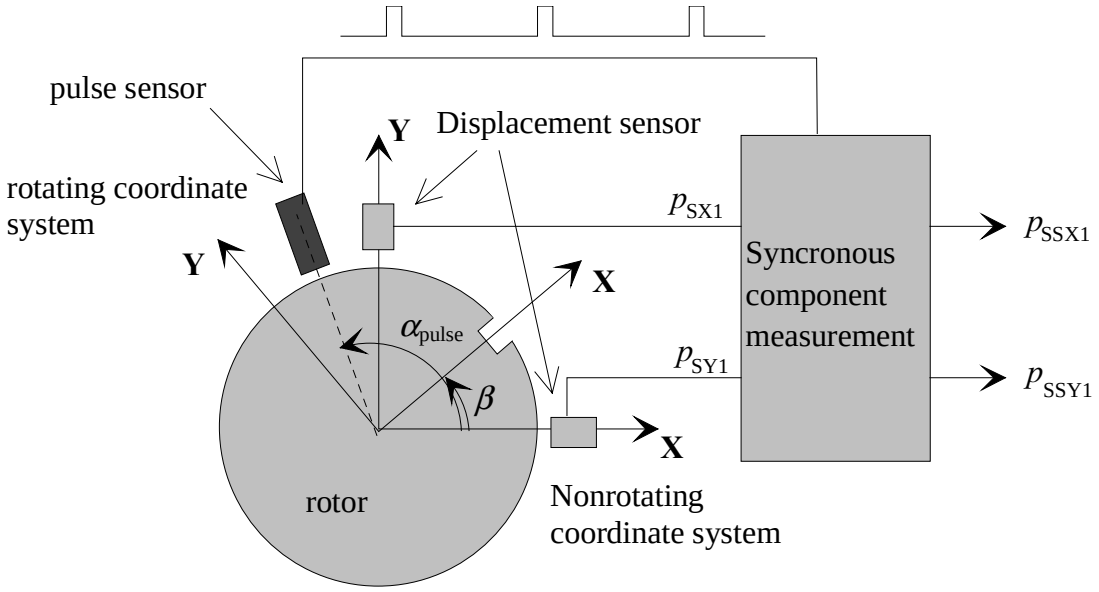

Figure 46. Synchronous component measurement for balancing. The details of the block "synchronous component measurement" are found in Figure 36.

Unbalance compensation (strategy "3" in Section 4.2) is active in the balancing procedure. This decreases the rotation synchronous bearing force to a sufficiently low level so that it can be neglected in the analysis. Thus, the rotor orbit in the displacement sensor locations should be circular, and the center of the rotor remains stationary in the coordinate system rotating with the rotor. The position of the rotor in this rotating coordinate system is

$$\boldsymbol{p}'_{\mathrm{S}} = e^{-j\alpha_{\mathrm{pulse}}} \begin{bmatrix} \mathrm{Re}\left(p_{\mathrm{SSX1}}\right) + j\mathrm{Re}\left(p_{\mathrm{SSY1}}\right) \\ \mathrm{Re}\left(p_{\mathrm{SSX2}}\right) + j\mathrm{Re}\left(p_{\mathrm{SSY2}}\right) \end{bmatrix}. \tag{47}$$

The rotor position in the rotating reference frame could be computed using only one of the synchronous components, but then the rotation direction would be needed. It turns out that the rotation direction is not needed at all in the balancing procedure. When the rotational

synchronous force component is negligible, the rotor position in the rotating reference frame is obtained according to Equation 48.

$$\begin{aligned} \boldsymbol{p}'_{\mathrm{S}} &= \boldsymbol{C}_{\mathrm{S}}\left[\boldsymbol{K}_{\mathrm{rot}} - \Omega^2\left(\boldsymbol{M}_{\mathrm{rot}} - \boldsymbol{G}_{\mathrm{rot}}\right)\right]^{-1}\Omega^2\boldsymbol{U}_{\mathrm{C}} \\ \boldsymbol{U}_{\mathrm{C}} &= \boldsymbol{B}_{\mathrm{bal}}\boldsymbol{U}_{\mathrm{bp}}\ , \end{aligned} \tag{48}$$

where $\boldsymbol{C}_{\mathrm{S}}$, $\boldsymbol{K}_{\mathrm{rot}}$, $\boldsymbol{M}_{\mathrm{rot}}$ and $\boldsymbol{G}_{\mathrm{rot}}$ are the matrices of the rotordynamic model,
$\boldsymbol{B}_{\mathrm{bal}}$ is the transformation matrix from balancing plane forces to generalized forces,
$\boldsymbol{U}_{\mathrm{C}}$ is the complex modal unbalance vector and
$\boldsymbol{U}_{\mathrm{bp}}$ are the complex unbalances reduced to the balancing planes.

In the balancing procedure the rotor is slowly accelerated to the maximum speed and the computer collects the measured synchronous components. The unbalance compensation is active. Assume that there are N measurements. The results are collected into vector $\boldsymbol{y}$ and matrix $\boldsymbol{T}$ as follows

$$\boldsymbol{y} = \begin{bmatrix} \boldsymbol{p}'_{\mathrm{S}}(1) \\ \boldsymbol{p}'_{\mathrm{S}}(2) \\ \vdots \\ \boldsymbol{p}'_{\mathrm{S}}(N) \end{bmatrix}, \quad \boldsymbol{T} = \begin{bmatrix} \boldsymbol{C}_{\mathrm{S}}\left[\boldsymbol{K}_{\mathrm{rot}} - \Omega^2(1)\left(\boldsymbol{M}_{\mathrm{rot}} - \boldsymbol{G}_{\mathrm{rot}}\right)\right]^{-1}\Omega^2(1)\boldsymbol{B}_{\mathrm{bal}} \\ \boldsymbol{C}_{\mathrm{S}}\left[\boldsymbol{K}_{\mathrm{rot}} - \Omega^2(2)\left(\boldsymbol{M}_{\mathrm{rot}} - \boldsymbol{G}_{\mathrm{rot}}\right)\right]^{-1}\Omega^2(2)\boldsymbol{B}_{\mathrm{bal}} \\ \vdots \\ \boldsymbol{C}_{\mathrm{S}}\left[\boldsymbol{K}_{\mathrm{rot}} - \Omega^2(N)\left(\boldsymbol{M}_{\mathrm{rot}} - \boldsymbol{G}_{\mathrm{rot}}\right)\right]^{-1}\Omega^2(N)\boldsymbol{B}_{\mathrm{bal}} \end{bmatrix}. \tag{49}$$

If the model was correct and there is no measurement noise, then $\boldsymbol{y} = \boldsymbol{T}\boldsymbol{U}_{\mathrm{bp}}$. The unbalance that explains the measurements best in the least squares sense is obtained as

$$\hat{\boldsymbol{U}}_{\mathrm{bp}} = \left(\boldsymbol{T}^{\mathrm{T}}\boldsymbol{T}\right)^{-1}\boldsymbol{T}^{\mathrm{T}}\boldsymbol{y}\ . \tag{50}$$

Note that, even though the matrix $\boldsymbol{T}$ is here obtained from finite element modeling, it can also be measured using test weights or test holes.

Theoretical analysis

Let us next analyze theoretically how the different error sources affect the results. First of all, a good question is how many bending modes should be included in Equation 49. In principle, the full order FEM model could be used to form the matrix $\boldsymbol{T}$. However, with this rotor and at the speed range of interest a reduced model with only one bending mode included gives practically the same results. This can be deduced by comparing the responses from the balancing plane forces to the displacement signals achieved from the full-order model and the reduced model.

To analyze the effect of the errors on different modal unbalance estimates, let us construct a transformation matrix $\boldsymbol{T}_{\mathrm{m}}$ without the $\boldsymbol{B}_{\mathrm{bal}}$ matrices. Let us use 200 equally distributed frequency points between 200 Hz and 540 Hz to form $\boldsymbol{T}_{\mathrm{m}}$. Now, let us take the position stiffness into consideration. So, compute "true" $\boldsymbol{T}_{\mathrm{mtrue}}$ including the position stiffness effect:

$$\boldsymbol{T}_{\mathrm{m}} = \begin{bmatrix} \boldsymbol{C}_{\mathrm{S}}\left[\boldsymbol{K}_{\mathrm{rot}} - \Omega^2(1)\left(\boldsymbol{M}_{\mathrm{rot}} - \boldsymbol{G}_{\mathrm{rot}}\right)\right]^{-1}\Omega^2(1) \\ \vdots \\ \boldsymbol{C}_{\mathrm{S}}\left[\boldsymbol{K}_{\mathrm{rot}} - \Omega^2(N)\left(\boldsymbol{M}_{\mathrm{rot}} - \boldsymbol{G}_{\mathrm{rot}}\right)\right]^{-1}\Omega^2(N) \end{bmatrix},$$

$$\boldsymbol{T}_{\mathrm{mtrue}} = \begin{bmatrix} \boldsymbol{C}_{\mathrm{S}}\left[\boldsymbol{K}_{\mathrm{rot}} - \boldsymbol{B}_{\mathrm{b}}c_0\boldsymbol{B}_{\mathrm{b}}^{\mathrm{H}} - \Omega^2(1)\left(\boldsymbol{M}_{\mathrm{rot}} - \boldsymbol{G}_{\mathrm{rot}}\right)\right]^{-1}\Omega^2(1) \\ \vdots \\ \boldsymbol{C}_{\mathrm{S}}\left[\boldsymbol{K}_{\mathrm{rot}} - \boldsymbol{B}_{\mathrm{b}}c_0\boldsymbol{B}_{\mathrm{b}}^{\mathrm{H}} - \Omega^2(N)\left(\boldsymbol{M}_{\mathrm{rot}} - \boldsymbol{G}_{\mathrm{rot}}\right)\right]^{-1}\Omega^2(N) \end{bmatrix}, \tag{51}$$

$$\hat{\boldsymbol{U}}_{\mathrm{C}} = \left(\hat{\boldsymbol{T}}^{\mathrm{H}}\hat{\boldsymbol{T}}\right)^{-1}\hat{\boldsymbol{T}}^{\mathrm{H}}\boldsymbol{T}_{\mathrm{true}}\boldsymbol{U}_{\mathrm{C}} = \begin{bmatrix} 0.98 & 0.01 & 0.02 \\ 0.00 & 0.97 & 0.00 \\ 0.00 & 0.00 & 1.01 \end{bmatrix}\boldsymbol{U}_{\mathrm{C}},$$

where $\boldsymbol{U}_{\mathrm{C}}$ is the true modal unbalance vector and $\hat{\boldsymbol{U}}_{\mathrm{C}}$ is the estimate. Thus, the effect of the remainder force due to position stiffness has practically no effect on the unbalance estimates. Let us next assume that the prediction of the first bending eigenfrequency is slightly optimistic. Let the true third modal stiffness be 10 % smaller than the estimated one. Let us also analyze the effect of asymmetric position sensor sensitivity. In the first case the true displacement sensor sensitivity is 10 % smaller than nominal at the 1-end and 10 % bigger than nominal at the 2-end, and in the second case vice versa. The effect of these three types of errors are:

$$\hat{\boldsymbol{U}}_{\mathrm{C}} = \begin{bmatrix} 1 & 0 & 0.45 \\ 0 & 1 & 0 \\ 0 & 0 & 1.33 \end{bmatrix} \boldsymbol{U}_{\mathrm{C}} \text{ , first bending mode stiffness 10 \% smaller ,}$$

$$\hat{\boldsymbol{U}}_{\mathrm{C}} = \begin{bmatrix} 1.01 & 0.72 & -0.13 \\ 0.01 & 1.01 & -0.07 \\ 0 & 0 & 0.98 \end{bmatrix} \boldsymbol{U}_{\mathrm{C}} \text{ , sensor sensitivity 1 - end } +10\ \%,\ 2 \text{ - end } -10\ \%, \qquad (52)$$

$$\hat{\boldsymbol{U}}_{\mathrm{C}} = \begin{bmatrix} 1.01 & -0.72 & -0.05 \\ -0.01 & 1.01 & 0.07 \\ 0 & 0 & 1.00 \end{bmatrix} \boldsymbol{U}_{\mathrm{C}} \text{ , sensor sensitivity 1 - end } -10\ \%,\ 2 \text{ - end } +10\ \%.$$

As one can see, the balancing result is sensitive to the error in the bending eigenfrequency. This is due to the fact that the actual rotor is bending more rapidly with the same unbalance, so the estimated third modal unbalance will be too high. Note that the unbalance estimate of rigid-body translatory mode will also be erroneous if there is unbalance at the bending mode. Therefore, the bending eigenfrequency should be known accurately. The asymmetry in the sensor sensitivity deteriorates the rigid-body unbalance estimates, as expected. However, the effect on the bending mode unbalance estimate is small, because the bending mode amplitude is about the same at both the sensor locations.

Next, assume that there is an external constant rotating force F acting on the rotor on the second balancing plane, i.e. in the middle of the rotor. This could be caused by dynamic eccentricity in the motor. This leads to $\hat{\boldsymbol{U}}_{\mathrm{C}} - \boldsymbol{U}_{\mathrm{C}} = \begin{bmatrix} 474 & -4.7 & 20 \end{bmatrix}^{\mathrm{T}} (g\,mm / 1000\,N) * F$. To get an idea what large modal unbalance is, we note that 1 μm vibration at the 2-end sensor location at 540 Hz is caused by 80 gmm unbalance at the first mode, 10 gmm in the second mode or 5.2 gmm in the third mode, i.e. the first bending mode. Thus, even a 1000 N rotating force will not deteriorate the results too much.

Finally, let us assume that there is measurement noise. Let us assume that the measurement noise has Gaussian distribution with a 5 μm mean deviation $\mathrm{E}\left[\tilde{y}^*(n)\tilde{y}(n)\right] = (5\mu m)^2$. The diagonal elements of the unbalance estimate covariance matrix are then $\mathrm{diag}\left\{\mathrm{E}\left[\left(\hat{\boldsymbol{U}}_{\mathrm{C}} - \boldsymbol{U}_{\mathrm{C}}\right)\left(\hat{\boldsymbol{U}}_{\mathrm{C}} - \boldsymbol{U}_{\mathrm{C}}\right)^{\mathrm{H}}\right]\right\} = \left\{(33\,\mathrm{gmm})^2, (2.8\,\mathrm{gmm})^2, (5.6\,\mathrm{gmm})^2\right\}$. So, the error caused by measurement noise is very small, i.e. the large number of measurement points effectively cancels the effect of uncorrelated measurement noise.

Experimental test

The balancing procedure was tested with an individual machine which happened to have very high third modal unbalance. On the left-hand side of Figure 47 the vibration amplitudes of the test machine are shown before balancing. There is no significant rigid-body unbalance, the high vibrations at low speeds are due to electric motor forces. The bending is, however, too high. The vibration amplitude of 50 μm at the position sensor location means 130 μm vibration in the compressor wheel. The modal unbalance of the first bending mode was 265 gmm before balancing.

First, over a period of three minutes, the rotor was accelerated from zero to maximum speed. The unbalance compensation started at 200 Hz. The vibration information was collected from 200 Hz to 540 Hz, about 200 samples. After that, the balancing masses were computed for the three planes and drilling was performed. Then the machine was again slowly accelerated to maximum speed. These results are on the right-hand side of Figure 47.

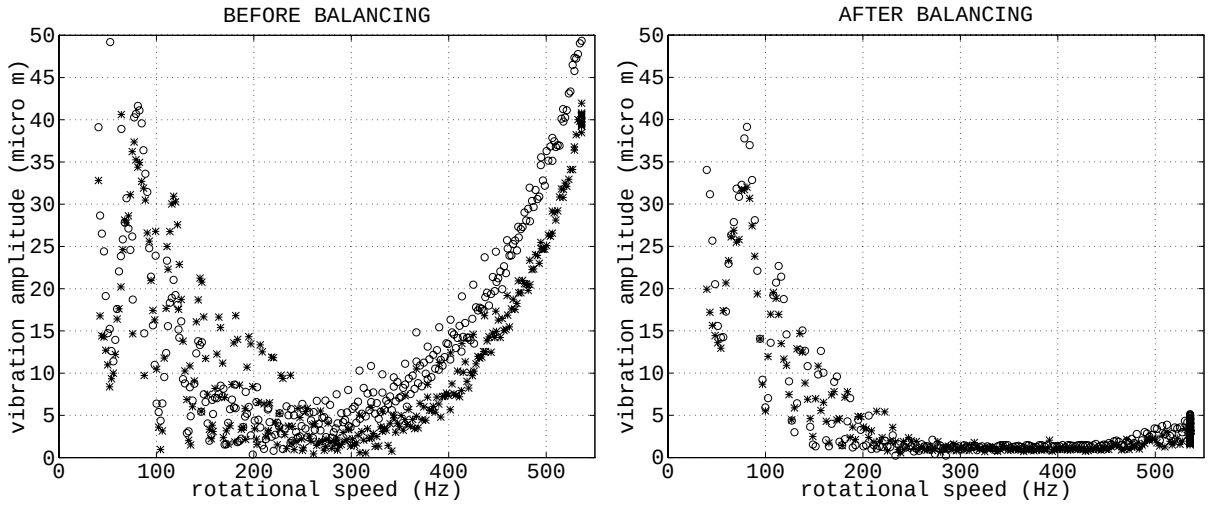

Figure 47. Experimental balancing result. Vibrations in the 1-end sensor are labeled with asterisks (*) and vibrations in the 2-end sensor with circles (o).

As one can see, the result is excellent. The modal unbalance of the first bending mode was reduced to 22 gmm. Naturally, the balancing had no effect on the vibrations caused by the electric motor forces. It should be pointed out that no iteration was needed. This result was obtained with only one run-up and one drilling. This is important, because the balancing planes are in the electric motor section, and having too many holes deteriorates the motor performance.

5 SUMMARY

The purpose of this work was to develop methods for building robust control systems for magnetic bearings in subcritical machines. The problem treatment was basically separated into three parts. First, the different parts of the suspension system were analyzed. Then, the position control system was synthesized and, finally, the unbalance problem was considered.

The different parts of the suspension system were analyzed in Chapter 2. The linearized bearing model was presented and the parameter variations were found. It was seen that the uncertainty of the current stiffness is the most important effect. Then the actuator response was simulated at higher signal amplitudes. Simulation showed that after certain frequency, there will be a phase lag between the reference current and the bearing force at large signal amplitude. Also the deteriorating effect of a high-frequency high-amplitude disturbance was clearly shown. Then, it was explained that the subcritical operation is preferred because the bearing forces will be high in the passing of the bending critical speeds. An interesting result is that the minimum bearing force needed to pass an unsupported bending critical speed depends only on the rotor geometry, bearing locations and the unbalance distribution.

In Chapter 3, the position control loop was considered. First, the SISO case was carefully analyzed. The physical performance limit was found at every frequency separately. Then, it was shown by H_∞-optimization that one controller cannot achieve this limit at every frequency, but there is an inherent tradeoff between low and high frequencies. It was suggested that the low frequencies should be preferred. Then, it was shown that a good practical controller can be obtained by manual tuning. Then, the damping of the bending mode was analyzed. Five different damping strategies were proposed. An interesting nontrivial strategy is the all-pass filter achieved from H_∞-optimization.

A generalization of the Nyquist diagram, based on the numerical range, was successfully used in the analysis of both the position control loop and the unbalance compensator. This method gives highly nonconservative stability margin predictions at least in the case of near normal open loops. In addition, this Nyquist diagram has certain interesting relationships with the closed-loop singular values of the sensitivity function and the complementary sensitivity function. Thus, it also gives information about nominal performance. In the case of diagonal real uncertainties robust performance statements can be drawn. This method is particularly suitable for analyzing AMB because of the normality and shape of the open loop. However, it

is easy to construct systems where this method is useless. Therefore, generally in the control system design, this method can be considered as an additional tool to be used with other methods. A similar conclusion was also made by Owens (1984).

The true multivariable rigid-body suspension was then analyzed. It was shown that the decentralized control strategy may lead to problems. Then, the H_∞-optimal controller was obtained to get close to the physical performance limits. It was shown that the structure of the optimal controller is essentially so where the plant is diagonalized by input and output rotational matrices, and two controllers are then designed by SISO methods. The optimal solution leads to a normal open loop at the plant input and output. This observation was then generalized to a synthesis procedure for subcritical machines. The proposed method is very straightforward when the first bending mode is at very high frequency and the rotor is not too gyroscopic. If the bending mode comes closer to the gain crossover frequency, some insight and experience is needed. For critical speed passing or highly gyroscopic rotors the proposed controller structure is not generally suitable. However, the generalized Nyquist diagram is still worth trying.

In experimental testing, the stability limits were experimentally determined and impulse responses were measured. Then, the power amplifier saturation effects were analyzed both experimentally and using the describing function technique combined with the generalized Nyquist diagram. It was shown how the potential high amplitude instabilities could be predicted. The predictions were experimentally verified and they proved to be accurate.

From the position control loop analysis, some well-established design suggestions can be made. First, the open-loop gain cross-over frequency should be chosen near the position bandwidth, i.e. the frequency where the bearings are able to vibrate the rotor at the maximum allowed amplitude. Secondly, the force bandwidth, i.e. the frequency where the bearing is able to produce the maximum force should be somewhat higher than the gain cross-over frequency.

It was shown that an inevitable consequence of a well-designed position control loop is that the bearing does not tolerate so much unbalance as would be possible. For this reason, the unbalance problem was thoroughly studied. A simple compensation method was proposed where one parameter should be chosen. This parameter is determined from a generalized Nyquist diagram by visual observation. Due to the shape of a good open loop, it is obvious that the simple unbalance compensation works very generally and is robust. It should be noted that there are no difficulties running the compensation algorithm at the rigid-body resonance speeds. In some cases, the unbalance compensation alone does not solve the unbalance

problem and the rotor must be mechanically balanced. Use of AMB for balancing a high speed rotor with respect to two rigid-body modes and the first bending mode was tested. The results were excellent and no iteration was needed.

In this publication, large uncertainty was assumed for the actuator and the sensor. This is because we wanted to operate the bearing up to very high static load and allowed large variations in the air gap. Large uncertainty makes it difficult to obtain robust performance and also the nominal performance suffers. To get better results in the AMB control, uncertainties should be decreased somehow. For example flux control, nonlinear compensation, gain scheduling and on-line parameter estimation are possible techniques for that purpose.

REFERENCES

Antila M. 1998. Electromagnetic Properties of Radial Active Magnetic Bearings. Ph.D. thesis. *Acta Polytechnica Scandinavica Electrical Engineering series* 92. Espoo, Finland, 96 p.

Antila M., Lantto E., Arkkio A. 1998. Determination of Forces and Linearized Parameters of Radial Active Magnetic Bearings by Finite Element Technique. *IEEE Transactions on Magnetics.* **3**, No. 3, pp. 684-694.

Antila M., Lantto E., Saari J., Esa H., Lindgren O., Säily K. 1996. Design of Water Treatment Compressors Equipped with Active Magnetic Bearings. *Proceedings of the 5th International Symposium on Magnetic Bearings*, Kanazawa, Japan, pp. 389-394.

Agahi R.R., Ershaghi B.B. 1994. Side Load Effect on Turbomachines with AMB. *Proceedings of the 4th International Symposium on Magnetic Bearings,* Zurich, Switzerland, pp. 485-497.

Ahrens M., Kucera L., Larsonneur R. 1996. Performance of a Magnetically Suspended Flywheel Energy Storage Device. *IEEE Transactions on Control Systems Technology*, **4**, No. 5, pp. 494-502.

Ahrens M., Kucera L., Larsonneur R. 1996. Field Experiences with a Highly Unbalanced Magnetically Suspended Flywheel Rotor. *Proceedings of the 5th International Conference on Magnetic Bearings,* Kanazawa, Japan, pp. 125-130.

Ahrens, M., Kucera L. 1995. Cross Feedback Control of a Magnetic Bearing System. *Proceeedings of the 3rd International Symposium on Magnetic Suspension Technology.* Tallahassee, USA.

Arkkio A., Lindgren O. 1994. Finite Element Analysis of the Magnetic Forces Acting on an Eccentric Rotor of a High-Speed Induction Motor. *Proceedings of the 4th International Symposium on Magnetic Bearings*, Zurich, Switzerland, pp. 225-230.

Arkkio A. 1995. Unbalanced Magnetic Pull in a Four-Pole Induction Motor with an Odd Number of Rotor Slots. *Proceedings of the Second Chinese International Conference on Electric Machines,* CICIM'95, Hangzhou, China, pp.343-348.

Arkkio A. 1996. Unbalanced Magnetic Pull in Cage Induction Motors-Dynamic and Static Eccentricity. *Proceedings of the International Conference on Electric Machines*, **1**, Vigo, Spain, pp. 192-197.

Arkkio A. 1997. Unbalanced Magnetic Pull in Cage Induction Motors with Asymmetry in Rotor Structures. Eight International Conference on Electric Machines and Drives, Cambridge, UK.

Balas G., Doyle J., Glover K., Packard A., Smith R. 1993. *μ-Analysis and Synthesis Toolbox*, The MathWorks Inc.

Beale S., Shafai B., LaRocca P. and Cusson E. 1995. *Adaptive Forced Balancing for Multivariable Systems*. *ASME Journal of Dynamic Systems, Measurement and Control*, **117**, pp. 496-502.

Beams J.W., Young J.L., Moore J.W. 1946. The Production of High Centrifugal Fields. *Journal of Applied Physics*. **17**. pp. 886-890.

Bichler U.J. 1990. A Low Noise Magnetic Bearing Wheel for Space Application. *Proceedings of the 2nd International Symposium on Magnetic Bearings,* Tokyo, Japan, pp. 1-8.

Bleurer H. 1984. Decentralized Control of Magnetic Bearing Systems. Ph.D. thesis ETH, Zurich No. 7573. 93 p.

Bleurer H. 1992. A Survey of Magnetic Levitation and Magnetic Bearing Types. *JSME International Journal*, Series III, **35**, No. 3, p. 335-342.

Bode H.W. 1945. *Network Analysis and Feedback Amplifier Design*. D. Van Nostrand Company Inc. USA, 551 p.

Boehm J., Gerber R., Kiley N. 1993. Sensors for Magnetic Bearings. *IEEE Transactions on Magnetics*, **29** (6), pp. 2962-2964.

Bornstein K.R. 1991. Dynamic Load Capabilities of Active Electromagnetic Bearings. *Transactions of the ASME, Journal of Tribology*, **113**, pp. 598-603.

Brunet M. 1988. Practical Applications of the Active Magnetic Bearings to the Industrial World. *Proceedings of the 1st International Symposium on Magnetic Bearings*. Zurich. pp. 225-244.

Brunet M., Wagner B. 1994. Analysis of the Performance of an AMB Spindle in Creep Feed Grinding. *Proceedings of the 4th International Symposium on Magnetic Bearings*, ETH, Zurich, pp. 519-524.

Buhler P., Siegwart R., Herzog R. 1996. Digital Control for Low Cost Industrial AMB Applications. *Proceedings of the 5th International Symposium on Magnetic Bearings.* Kanazawa, Japan, pp. 83-88.

Burrows C., Sahinkaya M., Clements S. 1989. Active Vibration Control of Flexible Rotors: an Experimental and Theoretical Study. *Proceedings of the Royal Society of London*, **422**, pp. 123-146.

Canders W.R., Ueffing N., Schrader-Hausman U., Larsonneur R. 1994. MTG400: A Magnetically Levitated 400 kW Turbo Generator System for Natural Gas Expansion. *Proceedings of the 4th International Symposium on Magnetic Bearings*, ETH, Zurich, pp. 435-440.

Carrere F., Font S., Duc G. 1994. H_∞ Control Design of Flexible Rotor Magnetic Bearing System. *Proceedings of the 4th International Symposium on Magnetic Bearings*. Zurich, Switzerland, pp. 65-71.

Chan H. 1990. Vibration Control of a Large Turbogenerator by Electromagnetic Dampers. *Proceedings of the 2nd International Symposium on Magnetic Bearings*, July 12-14, Tokyo, Japan, pp. 161-167.

Charara A., De Miras J., Caron B. 1996. Nonlinear Control of a Magnetic Levitation System Without Premagnetization. *IEEE Transactions on Control Systems Technology*, **4**, No. 5, pp. 513-523.

Chen H., Ku C. 1991. Vibration Control of Submerged Rotors Using Magnetic Bearings. *Proceedings of the Conference on Recent Advances in Active Control of Sound and Vibration*. Virginia, USA, pp. 391-407.

Collado J.M., Rojas J.A. 1992. New Technique for Robust Stability. *Proceedings of the 31st Conference on Decision and Control*. Tuscon, Arizona, pp. 231-236.

Delprete C., Genta G., Carabelli S. 1994. Control Strategies for Decentralized Control of Active Magnetic Bearings. *Proceedings of the 4th International Symposium on Magnetic Bearings.* Zurich, Switzerland, pp. 29-34.

Desoer C., Wang Y. 1980. On the Generalized Nqyuist Stability Criterion. *IEEE Transactions on Automatic Control*, AC-25, No. 2, pp. 187-196.

Doyle J., Francis B., Tannenbaum A. 1992. *Feedback Control Theory*. Macmillan Publishing Company, NY. USA, 226 p.

Doyle J.C. 1982. Analysis of Feedback Systems with Structured Uncertainties. *IEE Proceedings*, Part D, 129(6), pp. 242-250.

Doyle J., Glover K., Khargonekar P., Francis B. 1989. State-Space Solutions to Standard H_2 and H_∞ Control Problems. *IEEE Transactions on Automatic Control*, **34**, No. 8, pp. 831-847.

Doyle J., Stein G. 1981. Multivariable Feedback Design: Concepts for a Classical/Modern Synthesis. *IEEE Transactions on Automatic Control,* AC-26, no. 1, pp. 4-16.

Dussaux M. 1990. The Industrial Applications of the Active Magnetic Bearing Technology. *Proceedings of the 2nd International Symposium on Magnetic Bearings*, July 12-14, Tokyo, Japan, pp. 33-38.

Earnshaw S. 1842. On the Nature of the Molecular Forces which Regulate the Constitution of the Luminiferous Ether. *Trans. Camb. Phil. Soc*. **7**, p. 97-112.

Fittro R., Knospe C., Stephens L. 1996. Experimental Results of μ-Synthesis Applied to Point Compliance Minimization. *Proceedings of the 5th International Symposium on Magnetic Bearings.* Kanazawa, Japan, pp. 203-208.

Fujita M., Matsumura F., Namerikawa T. 1992. μ-Analysis and Synthesis of a Flexible Beam Magnetic Suspension System. *Proceedings of the 3rd International Symposium on Magnetic Bearings*, Virginia, USA, pp. 495-504.

Fujita M., Hatake K., Matsumura F. 1993. Loop Shaping Based Robust Control of a Magnetic Bearing. *IEEE Control Systems*, August, pp. 57-65.

Förch P., Gähler C., Nordman R. 1996. AMB System for Rotordynamic Experiments: Calibration Results and Control. *Proceedings of the 5th International Symposium on Magnetic Bearings.* Kanazawa, Japan, pp. 171-178.

Genta G., Delprete C. 1995. Acceleration Through Critical Speeds of an Anisotropic, Non-Linear, Torsionally Stiff Rotor with Many Degrees of Freedom. *Journal of Sound and Vibration*, **180** (3), pp. 369-386.

Girault J.P. 1988. Implementation of Active Magnetic Bearings on Advanced Rocket Engine Turbopumps. *Proceedings of the 1st International Symposium on Magnetic Bearings*. Zurich, Switzerland, pp. 199-210.

Haberman H., Brunet M. 1978. Device for Compensating Synchronous Disturbances in the Magnetic Suspension of a Rotor. US Patent 4,121,143.

Haberman H., Brunet M. 1986. The Active Magnetic Bearing Enables Optimum Damping of Flexible Rotors. *International Journal of Turbo and Jet Engines*, **3**, pp. 63-77.

Hampel J. 1995. Basic Turbocompressor Control and Protection. *Turbomachinery International*, July/August 1995. pp. 36-41.

Hara S., Namerikawa T., Matsumura F. 1996. Improvement of Dynamic Response by Flux Feedback on Active Magnetic Bearings. *Proceedings of the 5th International Symposium on Magnetic Bearings.* Kanazawa, Japan, pp. 49-54.

Herzog R., B①hler P., Gähler C., Larsonneur R. 1996. Unbalance Compensation Using Generalized Notch Filters in the Multivariable Feedback of Magnetic Bearings. *IEEE Transactions on Control Systems Technology*, **4**, No. 5, pp. 580-586.

Herzog R., Bleurer H.1992. On Achievable H^{∞} Disturbance Attenuation in AMB Control. *Proceedings of the 3rd International Symposium on Magnetic Bearings*, Virginia, USA, pp. 485-494.

Higuchi T., Mizuno T. 1988. Balancing Measurement System Using Magnetic Bearings. *Proceedings of the 1st International Symposium on Magnetic Bearings,* Zurich, Switzerland, pp. 327-334.

Higuchi T., Otsuka M., Mizuno T. 1992. Identification of Rotor Unbalance and Reduction of Housing Vibration by Periodic Learning Control in Magnetic Bearings. *Proceedings of the 3rd International Symposium on Magnetic Bearings*, Virginia, USA, pp. 571-579.

Horn R., Johnson C. 1991. *Topics in Matrix Analysis*. Cambridge University Press. USA. 607 p.

Horowitz I. 1982. Quantitative Feedback Theory. *IEE Proceedings,* **129**, D, No. 6. pp. 215-226.

Hung Y., MacFarlane A. 1982. Multivariable Feedback: A Quasi-Classical Approach. *Lecture Notes in Control and Information Sciences.* Springer-Verlag Berlin Heidelberg, 182 p.

Kanemitsu Y., Ohsawa M., Watanabe K. 1990. Real Time Balancing of a Flexible Rotor Supported by Magnetic Bearing. *Proceedings of the 2nd International Symposium on Magnetic Bearings,* Tokyo, Japan, pp. 265-272.

Kim C., Lee C. 1997. In Situ Runout Identification in Active Magnetic Bearing System by Extended Influence Coefficient Method. *IEEE/ASME Transactions on Mechatronics*, **2**, No. 1, pp. 51-57.

Kirk J.A., Anand D.K., Pang D. 1994. Performance of a Magnetically Suspended Flywheel Energy Storage System. *Proceedings of the 4th International Symposium on Magnetic Bearings*, ETH, Zurich, pp. 547-552.

Knospe C.R. 1991. Stability and Performance of Notch Filter Controllers for Unbalance Response. Proceedings of the International Symposium on Magnetic Suspension Technology, NASA Langley, Pub. 3152, pp. 183-205.

Knospe C.R., Hope R.W., Fedigan S.J., Williams R.D. 1995. Experiments in the Control of Unbalance Response Using Magnetic Bearings. *Mechatronics*, **5**, pp. 385-400.

Knospe C.R., Tamer S.M. 1996. Experiments in Robust Unbalance Response Control. *Proceedings of the 5th International Symposium on Magnetic Bearings*, Kanazawa, Japan, pp. 131-136.

Knospe C.R., Tamer S.M., Fedigan S.J. 1997a. Robustness of Adaptive Rotor Vibration Control to Structured Uncertainty. *Transactions of the ASME, Journal of Dynamic Systems, Measurement, and Control*, **119**, pp. 243-250.

Knospe C.R., Tamer S.M., Fedigan S.J. 1997b. Synthesis of Robust Gain Matrices for Adaptive Rotor Vibration Control. *Transactions of the ASME, Journal of Dynamic Systems, Measurement, and Control*, **119**, pp. 298-300.

Konuma M., Czech E., Hafendörfer M., Silier I., Bauser E., Traxler A., Schweitzer G. 1994. Centrifuge for Solution Growth of Semiconductor Layers: An Application of Magnetic Bearings. *Proceedings of the 4th International Symposium on Magnetic Bearings*, ETH, Zurich, pp. 171-176.

Kouvaritakis B., Postlethwaite I. 1982. Principal gains and phases: insensitive robustness measures for assessing the closed-loop stability property. *IEE Proceedings*, **129**, part D, No. 6, pp. 233-241.

Lantto E. Väänänen J., Antila M. 1996. Effect of Foundation Stiffness on Active Magnetic Bearing Suspension. *Proceedings of the 5th International Symposium on Magnetic Bearings*, Kanazawa, Japan, pp. 37-42.

Lantto E. 1997. Finite Element Model for Elastic Rotating Shaft. *Acta Polytechnica Scandinavica, Electrical Engineering Series.* 88. Espoo, Finland, 73 p.

Lantto E., Antila M. 1995. Active Magnetic Bearings for High-Speed Machines. *Proceedings of the Stockholm Power Tech*, June 18-22 1995. Volume of the Invited Speakers Sessions. p. 69-74.

Lantto E., Antila M., Tommila V., Saari J., Lindgren O. 1997. Experiences on 250 kW High-Speed Turbocompressors Installed in a Pulp and Paper Mill. *Proceedings of the MAG97*, Virginia, USA.

Larsonneur R. 1990. Design and Control of Active Magnetic Bearing System for High Speed Rotation. Ph.D. thesis ETH No. 9140, Offsetdruckerei AG, Zurich, Switzerland.

Lindgren O., Säily K., Lantto E., Saari J., Antila M. 1995. Electromechanical Design of Motors and Active Magnetic Bearings for High-Speed Compressors. *Proceedings of the MAG'95*. pp. 47-55.

Maciejowski, J.M. 1989. *Multivariable Feedback Design*. Addison-Wesley. 424 p.

Maslen E., Hermann P., Scott M., Humphris R.R. 1989. Practical Limits to the Performance of Magnetic Bearings: Peak Force, Slew Rate and Displacement Sensitivity. *Journal of Tribology,* **111**, pp. 331-336.

Maslen E.H., Allaire P.E. 1992. Magnetic Bearing Sizing for Flexible Rotors. *Journal of Tribology,* **114**, pp. 223-229.

Maslen E. 1991. Magnetic Bearing Synthesis for Rotating Machinery. Ph.D. thesis. University of Virginia, USA, 205 p.

Matsumura F., Fujita M., Okawa K. 1990. Modeling and Control of Magnetic Bearing Systems Achieving a Rotation Around the Axis of Inertia. *Proceedings of the 2nd International Symposium on Magnetic Bearings,* Tokyo, Japan, pp. 273-280.

Matsumura, F., Namerikawa, T., Hagiwara, K. and Fujita M. 1996. Application of Gain Scheduled H_∞ Robust Controllers to a Magnetic Bearing. *IEEE Transactions on Control Systems Technology,* **4**, No. 5, pp. 484-493.

Matsushita O., Takanashi N, Takagi M. 1992. Third Order LPF Type Compensator for Flexible Rotor Suspension. *Proceedings of the 3rd International Symposium on Magnetic Bearings,* Virginia, USA, pp. 3-12.

Mazzochetti L., Rava E., Delprete C., Genta G., Carabelli S. 1994. Design, Construction and Testing of a Turbomolecular Pump With Five Axis Magnetic Suspension. *Proceedings of the 4th International Symposium on Magnetic Bearings,* Zurich, Switzerland, pp. 505-510.

Meeks C., McMullen P., Hibner D., Rosado L. 1994. Lightweight Magnetic Bearing System for Aircraft Gas Turbine Engines. *Proceedings of the 4th International Symposium on Magnetic Bearings,* ETH, Zurich, pp. 429-434.

Mees A.I. 1981. Achieving Diagonal Dominance. *System and Control Letters,* 1, 155-158.

Mizuno T., Higuchi T. 1992. Control of Magnetic Bearing Using the Observer for Unbalance. *Electrical Engineering in Japan,* **112**, No. 3, pp. 95-104.

Mohamed A., Busch-Vishniac I. 1995. Imbalance Compensation and Automatic Balancing in Magnetic Bearing Systems Using the Q-Parametrization Theory. *IEEE Transactions on Control Systems Technology*, **3**, No. 2, pp. 202-211.

Moulton D.H., Eakins P.S. 1992. Application of Magnetic Bearings to Solar C304 Natural Gas Pipeline Compressor. *Proceedings of the MAG'92*. Technomic publishing company. pp. 203-217.

Nakajima A. 1988. Research and Development of Magnetic Bearing Flywheels for Attitude Control of Spacecraft. *Proceedings of the 1st International Symposium on Magnetic Bearings,* ETH Zurich, Switzerland, June 6-8 1988, Springer-Verlag, pp. 3-12.

Nonami K., Ito T. 1996. μ Synthesis of Flexible Rotor-Magnetic Bearing System. *IEEE Transactions on Control Systems Technology*, **4**, No. 5, pp. 503-512.

Owens D.H. 1984. The Numerical Range: A tool for robust stability studies? *System & Control Letters*, **5**, No. 3. pp. 153-158.

Owens D.H. 1986. Robust Stability Theory Using Both Singular Value and Numerical Range Data. *IEEE Transactions on Automatic Control*, **AC-31**, No. 4. pp.348-349.

Palazoglu A., Khambanonda T. 1989. On the Use of the Numerical Range for the Robust Stability Problem. *Chemical Engineering Science*. **44**, No. 11, pp.2843-2492.

Penfield S.R., McCloskey T., Jones G. 1995. How to Avoid Pitfalls in Using Magnetic Bearings in Turbomachinery. *Proceedings of the MAG'95,* Virginia USA, pp. 87-97.

Postlethwaite I., Edmunds J. M., McFarlane A. 1981. Principal Gains and Principal Phases in the Analysis of Linear Multivariable Feedback Systems. *IEEE Transactions on Automatic Control*, 26, No.1, pp. 32-46.

Satoh, I., Murakami C., Nakajima A., Kanemitsu Y. 1990. A Self-Excited Vibration of Magnetic Bearing System with Flexible Structure. *Proceedings of the 2nd International Symposium on Magnetic Bearings*. Tokyo, Japan, pp. 329-335.

Schmied J. 1990. Experience with Magnetic Bearings Supporting a Pipeline Compressor. *Proceedings of the 2nd International Symposium on Magnetic Bearings.* Japan, pp. 47-56.

Schneider H. 1991. *Balancing Technology*. Carl Schenck AG. 223 p.

Schweitzer G. 1990. Magnetic Bearings -Applications, Concepts and Theory. *JSME International Journal,* Series III, Vol. 33, No. 1, p. 13-18.

Schweitzer G., Bleurer H., Traxler A. 1994. *Active Magnetic Bearings*. Hochschulverlag AG an der ETH Zürich. 243 p.

Siegwart R., Larsonneur R., Traxler A. 1990. Design and Performance of a High Speed Milling Spindle in Digitally Controlled Active Magnetic Bearings. *Proceedings of the 2nd International Symposium on Magnetic Bearings*, July 12-14, Tokyo, Japan, pp. 197-204.

Skogestad S., Postlethwaite I. 1996. *Multivariable Feedback Control*. John Wiley & Sons Ltd., England. 559 p.

Stephens L., Knospe C. 1996. μ-Synthesis Based, Robust Controller Design for AMB Machine Spindles. *Proceedings of the 5th International Symposium on Magnetic Bearings,* Kanazawa, Japan, pp. 153-158.

Studer P. 1978. Magnetic Bearings for Instruments in the Space Environment. NASA report no. 78048. 15 p.

Tian H., Nonami K. 1994. Robust Control of Flexible Rotor-Magnetic Bearing System Using Discrete Time Sliding Mode Control. *JSME International Journal*. Series C, **37**, No. 3. pp. 504-512.

Vance J.M. 1988. *Rotordynamics of Turbomachinery*. John Wiley & Sons Inc. USA. 388 p.

Yamashita K., Allaire P., Knospe C. 1996. Rotor Disturbance Attenuation Using An H∞ Controller for Active Magnetic Bearings. *Proceedings of the 5th International Symposium on Magnetic Bearings,* Kanazawa, Japan, pp. 227-232.

Zhou K., Doyle J.C., Glover K. 1997. *Robust and Optimal Control.* Prentice-Hall Inc. 596 p.

Zhuravlyov Y. 1992. Active Magnetic Bearings. Helsinki University of Technology*, Report series of the Laboratory of Electromechanics*, No. 37. 92 p.

Zhuravlyov Y., Afanasiev M., Lantto E. 1994. Inverse Problems of Magnetic Bearing Dynamics. *Proceedings of the 4th International Symposium on Magnetic Bearings,* ETH, Zurich, pp. 79-84.

Zmood R, Pang D., Anand D., Kirk J. 1990. Robust Magnetic Bearings for Flywheel Energy Storage Systems. *Proceedings of the 2nd International Symposium on Magnetic Bearings,* Tokyo, Japan, pp. 123-129.

APPENDIX A: The numerical range and the generalized Nyquist diagram

In this appendix the details of the generalized Nyquist diagram are given. First, some basic properties of the numerical range are listed. Next, the generalized Nyquist diagram is defined and the shape of the uncertainty region for AMB suspension is constructed. Then, the use of the generalized Nyquist diagram for analyzing nominal performance and robust performance is discussed. Finally, a structured Nyquist diagram is introduced to minimize the conservativeness of this method.

Some properties of the numerical range

The proofs of the following properties of the numerical range (also called the field of values in the literature) are found in the book of Horn and Johnson (1991). Let $\boldsymbol{L}$ be a $N\times N$ complex valued matrix. The numerical range of $\boldsymbol{L}$ is a set in complex plane

$$\varphi(\boldsymbol{L}) = \left\{ \boldsymbol{x}^{\mathrm{H}} \boldsymbol{L} \boldsymbol{x} \;\middle|\; \boldsymbol{x} \in \mathbf{C}^{N\times 1}, \boldsymbol{x}^{\mathrm{H}} \boldsymbol{x} = 1 \right\}, \tag{A1}$$

where $^{\mathrm{H}}$ means complex conjugate transpose.

The numerical range $\varphi(\boldsymbol{L})$ is convex, i.e. if complex numbers a and b belong to the set, then all the points in the line segment between a and b belong to it. All the eigenvalues of $\boldsymbol{L}$ belong to $\varphi(\boldsymbol{L})$. If the matrix $\boldsymbol{L}$ is normal (i.e. $\boldsymbol{L}\boldsymbol{L}^{\mathrm{H}} = \boldsymbol{L}^{\mathrm{H}}\boldsymbol{L}$), then the numerical range is a polygon, whose corners are eigenvalues. If the matrix is skew (not normal) then the numerical range is larger. This is illustrated in Figure A1. The spectral radius, the largest singular value and the numerical radius (maximum modulus of the numerical range) are related as follows

$$\begin{aligned} \frac{1}{2}\overline{\sigma}(\boldsymbol{L}) \le \max\left|\varphi(\boldsymbol{L})\right| \le \overline{\sigma}(\boldsymbol{L}), \\ \max\left|\rho(\boldsymbol{L})\right| \le \max\left|\varphi(\boldsymbol{L})\right|, \end{aligned} \tag{A2}$$

where $\rho(\boldsymbol{L})$ is the set of the eigenvalues of $\boldsymbol{L}$ and $\overline{\sigma}(\boldsymbol{L})$ is the largest singular value of $\boldsymbol{L}$.

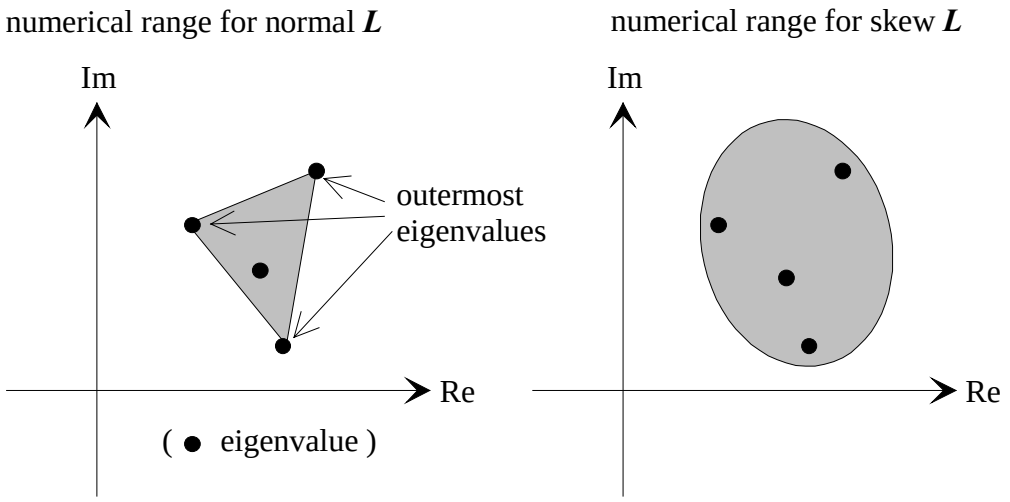

Figure A1. Numerical range for normal and skew matrix with the same eigenvalues.

The numerical range can be plotted as follows: Let us search for the upper and lower limit of $\varphi(\boldsymbol{L})$ in a direction α in a complex plane, see Figure A2.

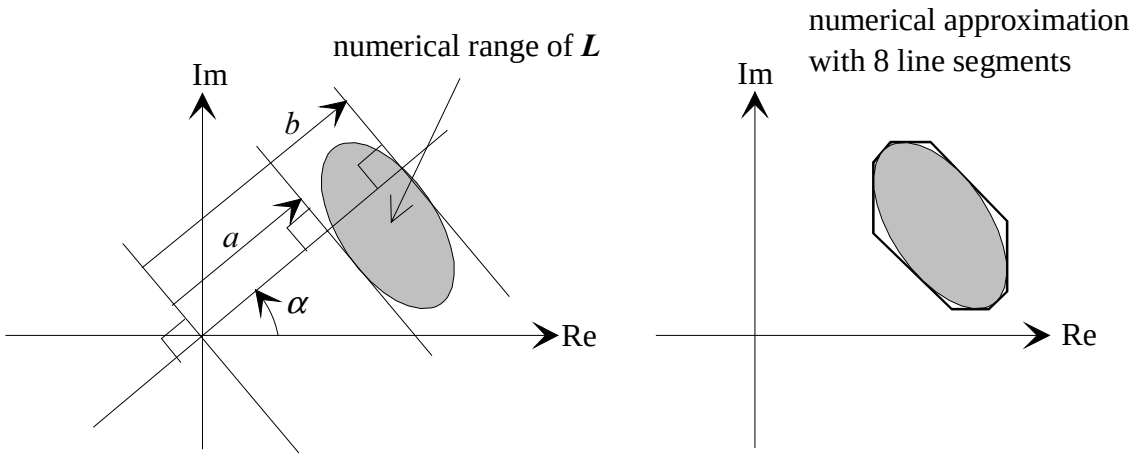

Figure A2. Numerical approximation of the numerical range.

To compute the upper and lower bound in direction α, first compute matrix $\boldsymbol{L}_\alpha = e^{-j\alpha}\boldsymbol{L}$. The bounds ($a$ and b in Figure A2) are obtained as the smallest and largest eigenvalues of $\left(\boldsymbol{L}_\alpha + \boldsymbol{L}_\alpha^{\mathrm{H}}\right)/2$, correspondingly. By choosing different α, the perimeter of the numerical range is approximated by segments.

Numerical range for a set of matrices

Let us consider a situation where matrix $\boldsymbol{L}$ is an affine function of N real parameters: $\boldsymbol{L}(\boldsymbol{a}) = \boldsymbol{L}_0 + \sum_{k=1}^{N} a_k \boldsymbol{L}_k$, where the parameters a_k are assumed real and limited in some closed interval. These parameters are collected into vector $\boldsymbol{a}$. The reason for this discussion becomes clear in the next subsection.

Generally, the union of all $\varphi(\boldsymbol{L}(\mathbf{a}))$ when $\boldsymbol{a}$ achieves all the allowed values is not convex and its computing is laborious. Thus, let us search for the convex hull, named co{}, of this set, i.e. $\mathrm{co}\left\{\cup\varphi\left[\boldsymbol{L}(\boldsymbol{a})\right] | \boldsymbol{a} \in \text{"allowed variations"}\right\}$. This is the smallest convex set which includes the mentioned union.

Let $\left\{\boldsymbol{L}_{\mathrm{bn}}\ , n = 1,2,\ldots,2^N\right\}$ be the set of matrices $\boldsymbol{L}(\boldsymbol{a})$ when all the elements of $\boldsymbol{a}$ are in their bounding values. There are 2^N different bounding combinations. For every $\boldsymbol{x}$ the set $\left\{\boldsymbol{x}^{\mathrm{H}}\boldsymbol{L}(\boldsymbol{a})\boldsymbol{x} \ \middle| \boldsymbol{a} \in \text{"allowed variations"}\right\}$ is a convex polygon, where the corner points are obtained with some bounding combinations of $\boldsymbol{a}$. Therefore,

$$\begin{aligned} \mathrm{co}\left\{\cup\varphi\left[\boldsymbol{L}(\boldsymbol{a})\right] | \boldsymbol{a} \in \text{"allowed variations"}\right\} &= \mathrm{co}\left\{\cup\varphi\left(\boldsymbol{L}_{\mathrm{bn}}\right) \middle| n = 1,2,\ldots,2^N\right\} \\ &= \varphi\left(\mathrm{diag}\left\{\boldsymbol{L}_{\mathrm{b1}}, \boldsymbol{L}_{\mathrm{b1}}, \cdots, \boldsymbol{L}_{\mathrm{b2}^N}\right\}\right) \quad . \end{aligned} \tag{A3}$$

The proof of the second equality is found in Horn and Johnson (1991). So, to compute the convex hull of the union of the numerical ranges, it is enough to compute the convex hull for a finite number of numerical ranges computed for matrices achieved with bounding parameter values.

The following example illustrates this. Let $\boldsymbol{A}$ and $\boldsymbol{B}$ be complex matrices and $\boldsymbol{L}$ be defined as $\boldsymbol{L}(a) = \boldsymbol{A} + a(\boldsymbol{B} - \boldsymbol{A})$ and $0 \le a \le 1$. The bounding matrices are $\boldsymbol{A}$ and $\boldsymbol{B}$. The numerical ranges for $\boldsymbol{A}$ and $\boldsymbol{B}$ are drawn in Figure A3 as well as the numerical ranges for $\boldsymbol{L}$ as a varies from 0 to 1.

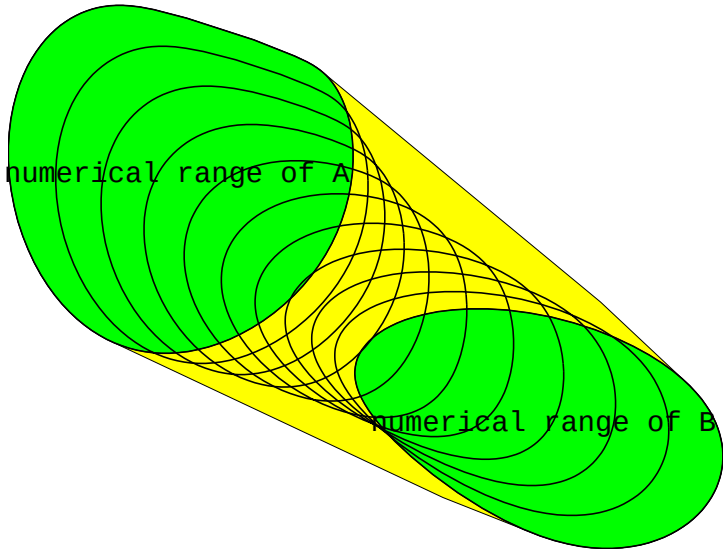

Figure A3. Illustration of the numerical range for a linear combination of matrices. The numerical ranges A and B are achieved for matrices with bounding parameter combinations. The contours are computed for the matrices with non bounding parameters. Clearly, the union of these numerical ranges is not convex. The whole darkened region is the convex hull of the union.

The generalized Nyquist diagram

The numerical range has been proposed for robust stability studies by Owens (1984). He derived a robust stability condition that can be checked from an inverse Nyquist diagram by visual observation. The method explained in this subsection differs from that of Owens only in that the direct Nyquist diagram is used instead of the inverse Nyquist diagram.

Let us consider the open-loop transfer function matrix $\boldsymbol{L}(s)$. The closed loop is formed by connecting the output to the input by negative feedback. The stability of the closed loop can be determined using the generalized Nyquist theorem: If N_P is the number of right half plane poles of $\boldsymbol{L}(s)$ then the closed loop is stable if the eigenloci of $\boldsymbol{L}(s)$ encircles point -1 N_P times anticlockwise as s encircles the right half plane. The eigenloci is the locus of the eigenvalues of $\boldsymbol{L}(s)$ when s is varied. Several proofs of this theorem can be found in the literature, see especially Desoer and Wang (1980).

Let us study the stability of the closed loop, when the open loop is $\boldsymbol{L}=\boldsymbol{K}\boldsymbol{L}_0(s)$. $\boldsymbol{K}$ is an unknown gain matrix whose nominal value is $\mathbf{I}$. $\boldsymbol{K}$ has a certain structure that is considered later. $\boldsymbol{L}_0$ is the known nominal open-loop transfer function matrix. There is no problem in determining whether the closed loop is stable with the nominal open loop. The problem is to estimate how large changes in $\boldsymbol{K}$ the system tolerates without becoming unstable.

The open-loop eigenvalues are achieved from the following eigenvalue problem

$$\boldsymbol{K}\boldsymbol{L}_0\boldsymbol{v}_n = \lambda_n \boldsymbol{v}_n \ . \tag{A4}$$

By assuming that $\boldsymbol{K}$ is invertible and multiplying Equation A8 from the left by $\boldsymbol{K}^{-1}$ and $\boldsymbol{v}_n^{\mathrm{H}}$, an eigenvalue can be written as follows

$$\lambda_n = \frac{\boldsymbol{v}_n^{\mathrm{H}}\boldsymbol{L}_0\boldsymbol{v}_n}{\boldsymbol{v}_n^{\mathrm{H}}\boldsymbol{K}^{-1}\boldsymbol{v}_n}, \tag{A5}$$

where we have further assumed that $\boldsymbol{x}^{\mathrm{H}}\boldsymbol{K}^{-1}\boldsymbol{x} \neq 0$ for all allowed $\boldsymbol{K}$:s and nonzero $\boldsymbol{x}$:s. Unfortunately, the eigenvectors do not remain unchanged as the matrix $\boldsymbol{K}$ varies. So, Equation A5 is of limited use in predicting the eigenvalues of perturbed $\boldsymbol{L}$. However, if the vector $\boldsymbol{v}_{\mathrm{n}}$ is allowed to be any vector $\boldsymbol{x}$, not necessarily the eigenvector, then we can say that

$$\begin{aligned} &\lambda_n \in \left\{ \frac{a}{b} \,\middle|\, a \in \varphi(\boldsymbol{L}_0), b \in \phi(\boldsymbol{K}) \right\}, \\ &\phi(\boldsymbol{K}) = \cup\varphi\left(\boldsymbol{K}^{-1}\right),\ \boldsymbol{K} \in \text{"allowed variations"}, \end{aligned} \tag{A6}$$

where $\phi(\boldsymbol{K})$ is called the uncertainty region of $\boldsymbol{K}$. The proposed generalized Nyquist diagram is simply the plot of $\varphi\left[\boldsymbol{L}_0(j\omega)\right]$ at a sufficient number of frequency points.

In practice, a surprisingly small number of frequency points is enough in the frequency range where there are no poles near the imaginary axis. This is because in a small frequency range we may approximate $\boldsymbol{L}_0(j\omega) \approx \boldsymbol{L}_0(j\omega_0) + (\omega - \omega_0)d\boldsymbol{L}_0(j\omega)/d\omega$. Using Equation A3 it can be seen that the numerical ranges transform smoothly in a small frequency range, where the previous approximation is valid.

Often, there is uncertainty both at the plant input and at the plant output. So, the open loop is $\boldsymbol{L} = \boldsymbol{K}_{\mathrm{in}}\boldsymbol{C}\boldsymbol{K}_{\mathrm{out}}\boldsymbol{P}$ where $\boldsymbol{P}$ is the nominal plant, $\boldsymbol{C}$ is the controller, $\boldsymbol{K}_{\mathrm{in}}$ is the uncertain gain at the plant input and $\boldsymbol{K}_{\mathrm{out}}$ is the uncertain gain at the plant output. Sometimes the uncertainties can be moved beside each other in the loop, and then the situation is reduced to a case of only one uncertain gain matrix. However, usually this is not the case. Let us assume that the other

uncertainty, $\boldsymbol{K}_{\text{out}}$ in this case, is a “small” uncertainty and can be expressed as $\boldsymbol{K}_{\text{out}} = \mathbf{I} + \sum_{n=1}^{N} a_n \boldsymbol{K}_{\text{outn}}$ where the N real parameters a_{n} are limited to some closed interval. Thus, we should consider a set of open loops $\boldsymbol{L}_0(\boldsymbol{a}) = \boldsymbol{C}\boldsymbol{K}_{\text{out}}(\boldsymbol{a})\boldsymbol{P}$ where $\boldsymbol{a}$ achieves all the allowed values. For this kind of a system the generalized Nyquist diagram is the plot of sets $\text{co}\left\{\cup\varphi\left(\boldsymbol{L}_0(\boldsymbol{a})\right), \boldsymbol{a} \in \text{"allowed variations"}\right\}$ at a sufficient number of frequency points. The construction of this convex hull was studied earlier, see Equation A3.

So, robust stability can be seen from the generalized Nyquist diagram using visual observation. If the nominal system is stable and the numerical ranges $\varphi\left[\boldsymbol{L}_0(j\omega)\right]$ do not intersect the forbidden region -$\phi(\boldsymbol{K})$ then robust stability is obtained.

Uncertainty region for AMB

Next, let us see what the uncertainty region $\phi\left(\boldsymbol{K}_{\text{in}}\right)$ looks like for the AMB system. $\boldsymbol{K}_{\text{in}}$ is a 4×4 almost diagonal and almost real matrix. The absolute values of the diagonal elements are limited in the interval [k_{min},k_{max}] and the phase of the diagonal elements is limited in the sector $\pm\alpha_1$. In the present case; k_{min}=0.5, k_{max}=1.5, α_1=5°. There are also small nonzero off-diagonal elements in the locations (1,3), (3,1), (2,4) and (4,2) and the other off-diagonal elements are zero. The absolute values of these off-diagonal elements are smaller than p*”smaller of the corresponding diagonal elements” (for example, $|k_{13}| \le p \min\left\{|k_{11}|, |k_{33}|\right\}$). In the case of AMB, we assume p=0.1. To simplify this analysis, let us allow any value for the phases of the off-diagonal elements.

Let $\boldsymbol{K}_{\text{in}} = \left[k_{nm}\right]$ and $\boldsymbol{x} = \begin{bmatrix} x_1^* & x_2^* & x_3^* & x_4^* \end{bmatrix}^{\text{H}}$ be some complex valued vector for which $\boldsymbol{x}^{\text{H}}\boldsymbol{x} = 1$. Now,

$$\boldsymbol{x}^{\mathrm{H}}\boldsymbol{K}_{\mathrm{in}}^{-1}\boldsymbol{x} = a + b\,,$$

$$a = \overbrace{\left(\frac{k_{11}k_{33}}{k_{11}k_{33}-k_{13}k_{31}}\right)}^{e}\left[\overbrace{\left(x_1x_1^*\frac{1}{k_{11}}+x_3x_3^*\frac{1}{k_{33}}\right)}^{c}-\overbrace{\left(x_1^*x_3\frac{k_{13}}{k_{11}k_{33}}+x_1x_3^*\frac{k_{31}}{k_{11}k_{33}}\right)}^{d}\right], \qquad \text{(A7)}$$

$$b = \left(\frac{k_{22}k_{44}}{k_{22}k_{44}-k_{24}k_{42}}\right)\left[\left(x_2x_2^*\frac{1}{k_{22}}+x_4x_4^*\frac{1}{k_{44}}\right)-\left(x_2^*x_4\frac{k_{24}}{k_{22}k_{44}}+x_2x_4^*\frac{k_{42}}{k_{22}k_{44}}\right)\right].$$

First, notice that the values that a can have for all allowed k_{11}, k_{33}, k_{13} and k_{31} under the constraint that $x_1x_1^* + x_3x_3^* = 1$ is the same that b can have for all allowed k_{22}, k_{44}, k_{24} and k_{42} under the constraint that $x_2x_2^* + x_4x_4^* = 1$. Let us call this set of complex numbers γ. Further, all the values that $a+b$ can have under the constraint $\boldsymbol{x}^{\mathrm{H}}\boldsymbol{x} = 1$ is co(γ), i.e. the smallest convex region containing γ. So, it suffices to analyze what values a may have under the constraint $x_1x_1^* + x_3x_3^* = 1$. The term c (Equation A7) may have values inside a convex hull of a set of complex numbers whose absolute value is in the interval $\left[1/k_{\max}, 1/k_{\min}\right]$ and phase is limited in the sector $\pm\alpha_1$. This is the darker region in the left-hand side plot of Figure A4. The absolute value of d (Equation A7) is smaller than $p/\max\left\{|k_{11}|,|k_{33}|\right\}$ and phase may be any. Thus, the off-diagonal elements make the region γ wider. A geometrical way to describe this effect is to draw a circle with radius $p|z|$ into every point z in the boundary of the region achieved without off-diagonal elements. This is illustrated in Figure A4. The increase of the sector angle due to off-diagonal elements is $\alpha_2 = \arctan(p)$. Finally, the elements of the achieved region should be scaled by all possible values of e in Equation A7. In the present case this scaling is not done, because e deviates from its nominal value 1 only by 1 %. The construction of the set γ and $\phi(\boldsymbol{K}_{\mathrm{in}})$ is shown on the left-hand side plot of Figure A4. Note that γ is already convex, so $a+b$ may have only the values in the set γ. On the right hand side, the forbidden region - $\phi(\boldsymbol{K}_{\mathrm{in}})$ is drawn into complex plane.

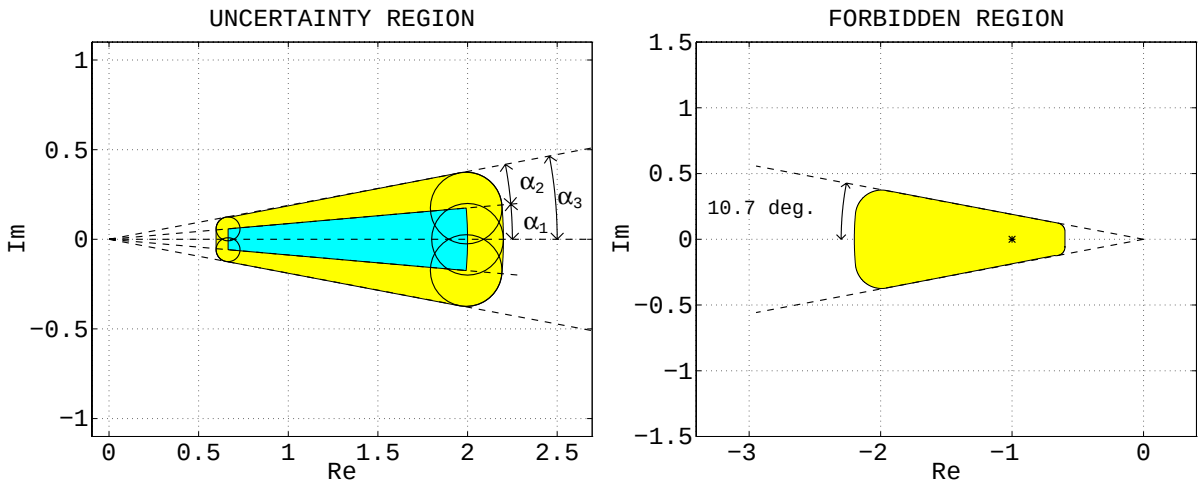

Figure A4. The construction of the uncertainty region $\phi(\boldsymbol{K}_{\text{in}})$ on the left hand side. On the right-hand side the forbidden region - $\phi(\boldsymbol{K}_{\text{in}})$ is shown.

Performance analysis

Previously it was shown that the generalized Nyquist diagram can be used to analyze robust stability. In this subsection it is shown how it can be used to analyze nominal performance and under certain assumptions robust performance also. Useful performance measures are the greatest and smallest singular values of the sensitivity function $\boldsymbol{S}$ and the complementary sensitivity function $\boldsymbol{T}$. An interesting question is whether we can say something about these singular values, using the numerical range drawn for the open-loop frequency response matrix $\boldsymbol{L}$.

Let $\boldsymbol{S}$ denote sensitivity function and $\boldsymbol{T}$ complementary sensitivity function. $\boldsymbol{A}$ is a function that arises in the analysis of the active magnetic bearing unbalance compensation algorithm. Let S, T and A denote scalar versions of the corresponding matrix functions:

$$\begin{aligned} \boldsymbol{S}(\boldsymbol{L}) &= (\mathbf{I}+\boldsymbol{L})^{-1}, & S(l) &= \frac{1}{1+l}, \\ \boldsymbol{T}(\boldsymbol{L}) &= \boldsymbol{L}(\mathbf{I}+\boldsymbol{L})^{-1}, & T(l) &= \frac{l}{1+l}, \\ \boldsymbol{A}(\boldsymbol{L}) &= \left((1-k_{\text{unb}})\mathbf{I}+\boldsymbol{L}\right)(\mathbf{I}+\boldsymbol{L})^{-1}, & A(l) &= \frac{1-k_{\text{unb}}+l}{1+l}. \end{aligned} \tag{A8}$$

where k_{unb} is a possibly complex valued scalar. The following inequalities hold:

$$
\begin{aligned}
&\text{(a):} \quad \overline{\sigma}(\boldsymbol{S}) \le \max_{l\in\varphi(\boldsymbol{L})}\left|S(l)\right|,\\
&\text{(b):} \quad \underline{\sigma}(\boldsymbol{S}) \le \min_{l\in\varphi(\boldsymbol{L})}\left|S(l)\right|,\\
&\text{(c):} \quad \min\left\{\max_{l\in\varphi(\boldsymbol{L})}\left|T(l)\right|,1\right\} \le \overline{\sigma}(\boldsymbol{T}) \le \max\left\{\max_{l\in\varphi(\boldsymbol{L})}\left|T(l)\right|,1\right\},\\
&\text{(d):} \quad \min\left\{\min_{l\in\varphi(\boldsymbol{L})}\left|T(l)\right|,1\right\} \le \underline{\sigma}(\boldsymbol{T}) \le \max\left\{\min_{l\in\varphi(\boldsymbol{L})}\left|T(l)\right|,1\right\},\\
&\text{(e):} \quad \min\left\{\max_{l\in\varphi(\boldsymbol{L})}\left|A(l)\right|,1\right\} \le \overline{\sigma}(\boldsymbol{A}) \le \max\left\{\max_{l\in\varphi(\boldsymbol{L})}\left|A(l)\right|,1\right\},\\
&\text{(f):} \quad \min\left\{\min_{l\in\varphi(\boldsymbol{L})}\left|A(l)\right|,1\right\} \le \underline{\sigma}(\boldsymbol{A}) \le \max\left\{\min_{l\in\varphi(\boldsymbol{L})}\left|A(l)\right|,1\right\},
\end{aligned}
\tag{A9}
$$

To analyze the singular values of some closed loop function, the constant absolute value curves for the corresponding scalar function are drawn into the generalized Nyquist diagram. Then, the minimum and maximum absolute value that the scalar function achieves with the complex numbers inside the numerical range is determined using visual observation. The first inequality (a) is useful at low frequencies, where the largest singular value of $\boldsymbol{S}$ is an interesting performance measure. The upper bound for $\overline{\sigma}(\boldsymbol{S})$ can be determined using the generalized Nyquist diagram. The inequalities (a) and (c) are useful especially near the cross-over frequencies where the largest singular values of both $\boldsymbol{S}$ and $\boldsymbol{T}$ are typically bigger than 1. The upper bounds achieved from the generalized Nyquist diagram can be used to ensure that neither is too large. Figure A5 illustrates the use of Equation A9 to analyze the singular values of $\boldsymbol{S}$ and $\boldsymbol{T}$.

Note that the inequalities (c..f) actually provide necessary and sufficient conditions for checking whether all the singular values of $\boldsymbol{T}$ or $\boldsymbol{A}$ are larger or smaller than 1. The curve at where $\left|T(l)\right| = 1$ is the line Re(l)=-0.5. If this line is left tangent to the numerical range $\varphi(\boldsymbol{L})$ then the largest singular value of $\boldsymbol{T}$ is exactly 1 and if this line is right tangent to $\varphi(\boldsymbol{L})$ (this is the case in Figure A5) then the smallest singular value of $\boldsymbol{T}$ is exactly 1. Whether the singular values of $\boldsymbol{A}$ are less or higher than 1 can be checked in a similar way by comparing $\varphi(\boldsymbol{L})$ to the line where $\left|A(l)\right| = 1$. This line constitutes of the points that are in equal distance from point -1 and $-1+k_{\text{unb}}$.

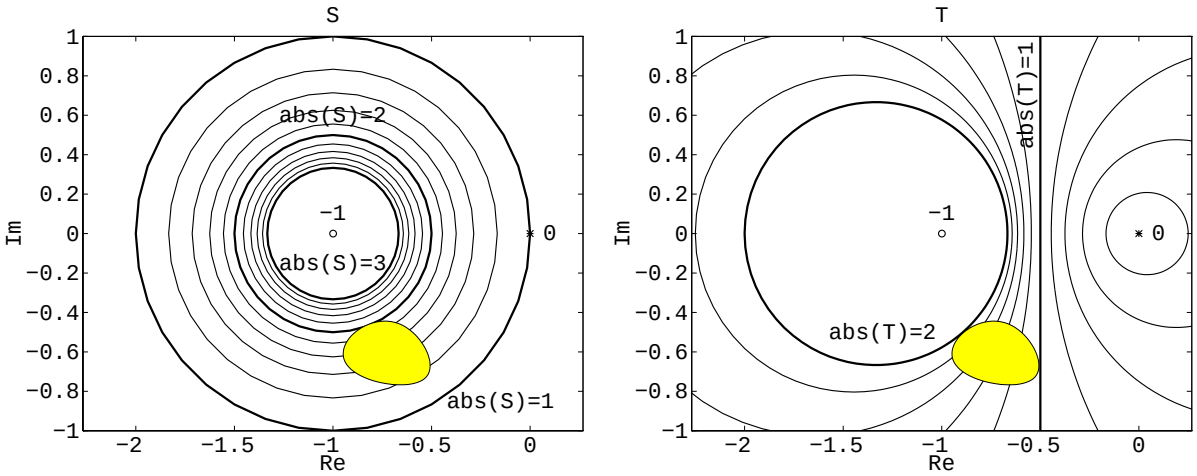

Figure A5. An example of analyzing the closed-loop singular values using the numerical range of the open-loop frequency response matrix. The gray region is the numerical range $\varphi(\boldsymbol{L})$. The step between the constant absolute value curves is 0.2. From the curves it is seen that the largest singular value of $\boldsymbol{S}$ is less than 2. The smallest singular value of $\boldsymbol{T}$ is exactly 1, and the largest singular value of $\boldsymbol{T}$ is less than 2.

Proof of Equation A9: Let us first analyze a more general problem. Define following functions:

$$\boldsymbol{F}(\boldsymbol{L}) = (q\,\mathbf{I} + v\boldsymbol{L})(r\,\mathbf{I} + w\boldsymbol{L})^{-1}, \quad F(l) = \frac{q + vl}{r + wl}, \tag{A10}$$

where q, r, v and w are, possibly complex valued, scalars and $\boldsymbol{L}$ is a complex valued $N\times N$ matrix. Let a be the 2-norm gain of $\boldsymbol{F}$ in certain direction $\boldsymbol{x}$:

$$a^2 = \frac{\boldsymbol{x}^{\mathrm{H}}\boldsymbol{F}^{\mathrm{H}}\boldsymbol{F}\boldsymbol{x}}{\boldsymbol{x}^{\mathrm{H}}\boldsymbol{x}}. \tag{A11}$$

After short manipulation this can be written as

$$\begin{aligned} a^2 &= \frac{\alpha + vv^* c^2}{\beta + ww^* c^2}, \\ \alpha &= qq^* + 2\mathrm{Re}\left(q^* v \frac{\boldsymbol{y}^{\mathrm{H}}\boldsymbol{L}\boldsymbol{y}}{\boldsymbol{y}^{\mathrm{H}}\boldsymbol{y}}\right), \beta = rr^* + 2\mathrm{Re}\left(r^* w \frac{\boldsymbol{y}^{\mathrm{H}}\boldsymbol{L}\boldsymbol{y}}{\boldsymbol{y}^{\mathrm{H}}\boldsymbol{y}}\right), c^2 = \frac{\boldsymbol{y}^{\mathrm{H}}\boldsymbol{L}^{\mathrm{H}}\boldsymbol{L}\boldsymbol{y}}{\boldsymbol{y}^{\mathrm{H}}\boldsymbol{y}}, \end{aligned} \tag{A12}$$

where $\boldsymbol{y} = (r\,\mathbf{I} + w\boldsymbol{L})^{-1}\boldsymbol{x}$. Next, let $b = \left|F\left(\boldsymbol{y}^{\mathrm{H}}\boldsymbol{L}\boldsymbol{y} / \boldsymbol{y}^{\mathrm{H}}\boldsymbol{y}\right)\right|$. This leads to

$$b^2 = \frac{\alpha + vv^* d^2}{\beta + ww^* d^2},\ d^2 = \left|\frac{\boldsymbol{y}^{\mathrm{H}}\boldsymbol{L}\boldsymbol{y}}{\boldsymbol{y}^{\mathrm{H}}\boldsymbol{y}}\right|^2. \tag{A13}$$

The expressions for a^2 and b^2 differ only in that one contains c^2 and the other d^2. It is easy to show that always $c^2 \geq d^2$. Now, let us study the complementary sensitivity function $\boldsymbol{T}$ for which $r = v = w = 1$, q=0. This leads to:

$$a^2 = \frac{c^2}{\beta + c^2},\ b^2 = \frac{d^2}{\beta + d^2},\ \beta = 1 + 2\mathrm{Re}\left(\frac{\boldsymbol{y}^{\mathrm{H}}\boldsymbol{L}\boldsymbol{y}}{\boldsymbol{y}^{\mathrm{H}}\boldsymbol{y}}\right). \tag{A14}$$

If β>0, then both a^2 and b^2 are smaller than unity and $a^2 \geq b^2$. Conversely, if β<0, both a^2 and b^2 are bigger than unity and $a^2 \leq b^2$. Thus, the inequalities (c) and (d) in Equation A9 hold. The proof of (e) and (f) goes the same way as the above proof and the proof of (a) and (b) is simple (end of proof).

So far, it has become obvious that the generalized Nyquist diagram can be used to analyze robust stability and nominal performance. Now, let us study whether the generalized Nyquist-diagram can be used to analyze robust performance as well. Consider open loop $\boldsymbol{L}=\boldsymbol{K}\boldsymbol{L}_0$. Assume that $\varphi(\boldsymbol{L}_0)$ and $\phi(\boldsymbol{K})$ are known, and $c \in \cup\varphi(\boldsymbol{K}\boldsymbol{L}_0)$, $\boldsymbol{K} \in$"allowed variations". The question is whether there always exist $a \in \varphi(\boldsymbol{L}_0)$ and $b \in \phi(\boldsymbol{K})$ such that $c=a/b$. Generally, the answer is no. This means that we can not make conclusions, using Equation A9, about the closed-loop singular values in the worst case if we only know $\varphi(\boldsymbol{L}_0)$ and $\phi(\boldsymbol{K})$.

Assume that $\boldsymbol{K}$ belongs to a set of real diagonal matrices with elements limited in the closed interval $[k_{\min}, k_{\max}]$ and $\boldsymbol{K}^{0.5}$ is the (positive) square root of $\boldsymbol{K}$. Then,

$$\frac{\boldsymbol{x}^{\mathrm{H}}\boldsymbol{K}^{0.5}\boldsymbol{L}_0\boldsymbol{K}^{0.5}\boldsymbol{x}}{\boldsymbol{x}^{\mathrm{H}}\boldsymbol{x}} = \frac{\boldsymbol{y}^{\mathrm{H}}\boldsymbol{L}_0\boldsymbol{y}}{\boldsymbol{y}^{\mathrm{H}}\boldsymbol{K}^{-1}\boldsymbol{y}}. \tag{A15}$$

So, it is easy to construct the union of all the numerical ranges if the open loop is cut in an artificial midpoint inside the uncertain gain matrix. This region is simply constructed by scaling the original $\varphi(\boldsymbol{L}_0)$ by all the real values $[k_{\min}, k_{\max}]$. Thus, using Equation A9, we can make some robust performance statements at this point of the plant. Of course, it depends on the application whether this "midpoint performance" is useful and the assumption of real diagonal perturbation is valid.

The structured Nyquist diagram

The stability robustness statements deduced from the generalized Nyquist diagram may be conservative, especially when the nominal open loop is considerably skew. In this subsection the conservativeness of this method is minimized by introducing a structured Nyquist diagram.

Let us consider open loop $\boldsymbol{L}=\boldsymbol{K}\boldsymbol{L}_0$. Let $\mathbf{D}$ be an invertible matrix that commutes with all allowed $\boldsymbol{K}$:s i.e. $\boldsymbol{K}\mathbf{D}=\mathbf{D}\boldsymbol{K}$. The eigenvalues of a matrix remain unchanged when the matrix is multiplied from the left by $\mathbf{D}$ and from the right by $\mathbf{D}^{-1}$. Thus, to analyze the system stability we can analyze eigenvalues of matrix $\mathbf{D}\,\boldsymbol{L}\,\mathbf{D}^{-1} = \mathbf{D}\,\boldsymbol{K}\boldsymbol{L}_0\,\mathbf{D}^{-1} = \boldsymbol{K}\left(\mathbf{D}\,\boldsymbol{L}_0\,\mathbf{D}^{-1}\right)$. Therefore, we can set tighter conditions for the open-loop eigenvalues.

$$\begin{aligned} \lambda_n &\in \left\{ \frac{a}{b} \,\middle|\, a \in \varphi_{\mathrm{S}}(\boldsymbol{L}_0), b \in \phi(\boldsymbol{K}) \right\}, \\ \varphi_{\mathrm{S}}(\boldsymbol{L}_0) &= \cap\varphi\left(\mathbf{D}\,\boldsymbol{L}_0\,\mathbf{D}^{-1}\right), \mathbf{D} \in \text{"allowed scalings"}, \end{aligned} \tag{A16}$$

where "allowed scalings" means the set of all invertible matrices which commute with all allowed $\boldsymbol{K}$:s and $\varphi_{\mathrm{S}}(\boldsymbol{L}_0)$ is called the structured numerical range. Obviously, $\varphi_{\mathrm{S}}(\boldsymbol{L}_0) \subset \varphi(\boldsymbol{L}_0)$. Also $\varphi_{\mathrm{S}}(\boldsymbol{L}_0)$ is convex, because it is an intersection of convex sets.

The structured Nyquist diagram is a plot of these structured numerical ranges at a sufficiently large number of frequency points. If the original diagram gives predictions which are too conservative, then this structured version is used. The unstructured version is, however, preferred because it provides also performance information which is lost when the

structured diagram is used. Furthermore, the computing of the structured numerical range is considerably harder.

Also this structured Nyquist diagram can be constructed for plants with two uncertainties, i.e. the $\boldsymbol{L}_0$ includes a "small" uncertainty. In this case $\varphi\left(\mathbf{D}\,\boldsymbol{L}_0\,\mathbf{D}^{-1}\right)$ in Equation A16 is replaced by $\mathrm{co}\left\{\cup\varphi\left(\mathbf{D}\,\boldsymbol{L}_0(\boldsymbol{a})\,\mathbf{D}^{-1}\right),\ \boldsymbol{a}\in\text{"allowed variations"}\right\}$. This convex hull is computed using the bounding matrices, as shown in Equation A3.

Let us now suppose that the structure of the uncertain gain matrix is such that the scaling matrix **D** is at least diagonal. Let us also assume that there are N bounding matrices $\boldsymbol{L}_{0n}$. First, notice that one of the diagonal elements of the scaling matrices can be assumed to be unity, because multiplying the scaling matrix by a constant does not change matrix $\mathbf{D}\boldsymbol{L}\mathbf{D}^{-1}$. Now, let us search for the smaller bound a in direction α, see Figure A2. Define $\boldsymbol{L}_{0n\alpha}=e^{-j\alpha}\boldsymbol{L}_{0n}$. The demand that all $\varphi\left(\mathbf{D}\,\boldsymbol{L}_{0n\alpha}\,\mathbf{D}^{-1}\right)$ have the smallest real parts bigger than a is equal to requiring that all the following matrix inequalities hold

$$\left(\mathbf{D}\,\boldsymbol{L}_{0n\alpha}\,\mathbf{D}^{-1}+\left(\mathbf{D}^{-1}\right)^{\mathrm{H}}\boldsymbol{L}_{0n\alpha}^{\mathrm{H}}\,\mathbf{D}^{\mathrm{H}}\right)-2a\,\mathbf{I}\geq 0\ ,\ n=1,2,\ldots,N\ , \tag{A17}$$

where "≥" means that the matrix is at least positive semidefinite. The truth of the inequalities remains unchanged when they are multiplied from the left by $\mathbf{D}^{\mathrm{H}}$ and from the right by **D**. The resulting inequalities reads

$$\left(\mathbf{D}^{\mathrm{H}}\mathbf{D}\right)\boldsymbol{L}_{0n\alpha}+\boldsymbol{L}_{0n\alpha}^{\mathrm{H}}\left(\mathbf{D}^{\mathrm{H}}\mathbf{D}\right)-2a\left(\mathbf{D}^{\mathrm{H}}\mathbf{D}\right)\geq 0\ ,\ n=1,2,\ldots,N\ . \tag{A18}$$

From this it is clear that the elements of the diagonal scaling matrix can be restricted to be positive real numbers. Also, it is obvious that the set of matrices where all the inequalities hold is convex, i.e. if all the inequalities hold for two scaling matrices, then they hold for all the weighted means of these two matrices. Even though this nice convexity property suggests that a reliable numerical method for finding maximum a can be constructed, the search is tedious in the general case.

Let us now concentrate on the 2×2 case and let $\mathbf{D} = \mathrm{diag}\left\{1, \sqrt{\mathrm{d}}\right\}$, $\boldsymbol{L}_{0n\alpha} = \left[l_{nij}\right]$. A bisection search is proposed. It is obvious that the optimum a_{opt} is in the interval

$$\begin{aligned} & a_{\min} \le a_{\mathrm{opt}} \le a_{\max}\ , \\ & a_{\min} = \min\left\{\lambda_m\left[\frac{1}{2}\left(\boldsymbol{L}_{0n\alpha} + \boldsymbol{L}_{0n\alpha}^{\mathrm{H}}\right)\right], m = 1,2\ , n = 1,2,\ldots,N\right\}, \\ & a_{\max} = \min\left\{\mathrm{real}\left[\lambda_1\left(\boldsymbol{L}_{0n\alpha}\right), \lambda_2\left(\boldsymbol{L}_{0n\alpha}\right), l_{n1,1}, l_{n2,2}\right], n = 1,2,\ldots,N\right\}. \end{aligned} \tag{A19}$$

Now a test a is chosen as an arithmetic mean of the minimum and maximum. Both the eigenvalues of the left-hand side matrix in Equation A22 are ≥0, if

$$-l_{n1,2}l_{n1,2}^{*}d^2 + \left[\left(l_{n1,1} + l_{n1,1}^{*} - 2a\right)\left(l_{n2,2} + l_{n2,2}^{*} - 2a\right) - \left(l_{n1,2}^{*}l_{n2,1}^{*} + l_{n1,2}l_{n2,1}\right)\right]d - l_{n2,1}l_{n2,1}^{*} \ge 0\ , \tag{A20}$$

where * means complex conjugate. Now, for every inequality, an interval for d is computed where the inequality holds. If these intervals have an nonempty intersection, then $a_{\mathrm{opt}} \ge a$ and otherwise $a_{\mathrm{opt}} < a$. This search proceeds until the difference between the upper bound and lower bound is smaller than a certain tolerance. Finally, the lower limit is chosen as an estimate of a_{opt}. If there is only one $\boldsymbol{L}_0$, then it is easy to show that the optimum scaling is independent of the direction α: $\mathbf{D} = \mathrm{diag}\left\{1, \sqrt{\left|l_{1,2}\ / l_{2,1}\right|}\right\}$.

The radial AMB suspension is a 4×4 system. However, due to its symmetrical nature, it is generally possible to change the problem of finding the structured numerical range for a 4×4 matrix into a problem of finding the smallest convex hull of structured numerical ranges of two 2×2 matrices. In the analysis of the magnetic bearing suspension we are faced with the following open-loop frequency response matrix

$$
\begin{aligned}
&\boldsymbol{L} = \boldsymbol{K}_{\text{in}}\left(\boldsymbol{C}\boldsymbol{K}_{\text{out}}\boldsymbol{R}\right),\\
&\boldsymbol{K}_{\text{in}} = \begin{bmatrix} k_{\text{in1,1}} & 0 & k_{\text{in1,3}} & 0\\ 0 & k_{\text{in2,2}} & 0 & k_{\text{in2,4}}\\ k_{\text{in3,1}} & 0 & k_{\text{in3,3}} & 0\\ 0 & k_{\text{in4,2}} & 0 & k_{\text{in4,4}} \end{bmatrix},\\
&\boldsymbol{C} = \begin{bmatrix} \boldsymbol{C}_1 & \boldsymbol{C}_2\\ -\boldsymbol{C}_2 & \boldsymbol{C}_1 \end{bmatrix},\ \boldsymbol{K}_{\text{out}} = \begin{bmatrix} \boldsymbol{K}_{\text{out1}}(\boldsymbol{a}) & \boldsymbol{0}\\ \boldsymbol{0} & \boldsymbol{K}_{\text{out1}}(\boldsymbol{a}) \end{bmatrix},\ \boldsymbol{R} = \begin{bmatrix} \boldsymbol{R}_1 & \boldsymbol{R}_2\\ -\boldsymbol{R}_2 & \boldsymbol{R}_1 \end{bmatrix}.
\end{aligned}
\tag{A21}
$$

Obviously, a matrix commuting with all possible $\boldsymbol{K}_{\text{in}}$:s is of the form $\mathbf{D} = \text{diag}\{\mathbf{D}_1, \mathbf{D}_1\}$, where $\mathbf{D}_1$ is a 2×2 diagonal matrix. If a matrix is multiplied from the left by a unitary matrix and from the right by its complex conjugate transpose, its numerical range remains unchanged, see Horn and Johnson (1991). Thus,

$$
\begin{aligned}
&\varphi\left(\mathbf{D}\,\boldsymbol{C}\boldsymbol{K}_{\text{out}}\boldsymbol{R}\,\mathbf{D}^{-1}\right) = \varphi\left(\mathbf{U}\mathbf{D}\,\boldsymbol{C}\boldsymbol{K}_{\text{out}}\boldsymbol{R}\boldsymbol{D}^{-1}\,\mathbf{U}^{\text{H}}\right)\\
&= \varphi\left(\begin{bmatrix} \mathbf{D}_1\left(\boldsymbol{C}_1 - j\boldsymbol{C}_2\right)\boldsymbol{K}_{\text{out1}}\left(\boldsymbol{R}_1 - j\boldsymbol{R}_2\right)\mathbf{D}_1^{-1} & \mathbf{0}\\ \mathbf{0} & \mathbf{D}_1\left(\boldsymbol{C}_1 + j\boldsymbol{C}_2\right)\boldsymbol{K}_{\text{out1}}\left(\boldsymbol{R}_1 + j\boldsymbol{R}_2\right)\mathbf{D}_1^{-1} \end{bmatrix}\right),\\
&= \text{co}\left\{\varphi\left[\mathbf{D}_1\left(\boldsymbol{C}_1 - j\boldsymbol{C}_2\right)\boldsymbol{K}_{\text{out1}}\left(\boldsymbol{R}_1 - j\boldsymbol{R}_2\right)\mathbf{D}_1^{-1}\right], \varphi\left[\mathbf{D}_1\left(\boldsymbol{C}_1 + j\boldsymbol{C}_2\right)\boldsymbol{K}_{\text{out1}}\left(\boldsymbol{R}_1 + j\boldsymbol{R}_2\right)\mathbf{D}_1^{-1}\right]\right\},\\
&\mathbf{U} = \frac{1}{\sqrt{2}}\begin{bmatrix} \mathbf{I}_2 & j\,\mathbf{I}_2\\ j\,\mathbf{I}_2 & \mathbf{I}_2 \end{bmatrix},
\end{aligned}
\tag{A22}
$$

where $\mathbf{I}_2$ is a 2×2 unity matrix. So, we can reduce the computing of the structured numerical range of this kind of a 4×4 matrix to a search of a convex hull of the structured numerical ranges of two 2×2 matrices. This is similar to the search for the convex hull of two bounding matrices, introduced earlier. If the matrix $\boldsymbol{K}_{\text{out1}}$ has N uncertain parameters, then the number of these matrices is multiplied by 2^N.

APPENDIX B: Gain phase relationships

The following equations were derived by Bode (1945). They are given here as a reminder of two basic phenomena appearing in the synthesis of control circuits using stable minimum phase transfer functions. First, if the controller has a wide phase advance region, it leads to high amplitude at high frequency. Secondly, a rapid phase drop leads to an amplitude increase in the frequency band where the phase drops. These consequences are quite easy to see from Equations B1 and B2.

Let G(s) be a stable minimum phase transfer function (no time delay or poles or zeros in the right half plane) and scaled so that $G(0)=1$. Let $\nu = \ln(\omega)$ be a logarithmic frequency, where ln means natural logarithm. Let $\alpha(\nu)$ be the phase of $G(j\omega)$ (in radians) and $g(\nu) = \ln\left|G(j\omega)\right|$. Using these assumptions, the phase and amplitude curves are related as

$$\alpha(\nu_0) = \frac{2}{\pi}\int_{-\infty}^{\infty} w_1(\nu-\nu_0)\frac{dg}{d\nu}d\nu\,, \tag{B1}$$

$$g(\nu_0) = \frac{2}{\pi}\int_{-\infty}^{\infty} w_2(\nu-\nu_0)\left[\alpha(\nu) - \frac{d\alpha(\nu)}{d\nu}\right]d\nu\,, \tag{B2}$$

where the weights are $w_1(\nu) = \frac{1}{2}\ln\left(\coth\left|\frac{\nu}{2}\right|\right)$ and $w_2(\nu) = e^{-\nu}\frac{1}{2}\ln\left(\coth\left|\frac{\nu}{2}\right|\right)$.

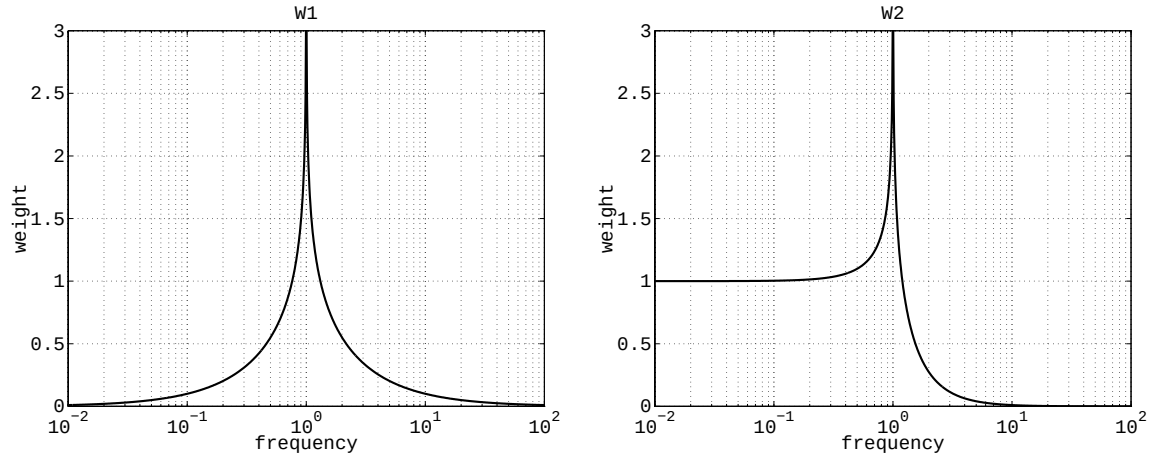

Figure B1. The weights w_1 and w_2 as a function of frequency. The peak at frequency 1 is infinite.

APPENDIX C: The test machine

The test machine is a 250 kW, 32000 1/min. water treatment compressor made by High Speed Tech Ltd. In the following, the main parameters of the machine considering magnetic bearings are given. The radial bearings are traditional 8-pole bearings. The bearing dimensions are given in Table C1 and the parameters of the linearized model in Table C2. The bearing geometry and the material magnetization curve are shown in Figure C1.

Table C1. The radial bearing dimensions.

Parameter	Value
Shaft diameter	69 mm
Rotor diameter	93.9 mm
Slot diameter	154 mm
Stator outer diameter	190 mm
Teeth width	18 mm
Nominal mechanical air gap	0.55 mm
Pole configuration	NSNSNSNS
Number of turns per pole	80
Coil connection	in series
Maximum voltage	150 V
Maximum current	10 A
Bias current	2.75 A

Table C2. Radial bearing parameters and performance.

Parameter	minimum	maximum	nominal
current stiffness	150 N/A	410 N/A	280 N/A
position stiffness	$1.5*10^6$ N/m	$3.5*10^6$ N/m	$2.3*10^6$ N/m
dynamic inductance	15 mH	45 mH	42 mH
Load capacity	1300 N	1800 N *	
Force bandwidth			177 Hz

* In the direction between the electromagnets.

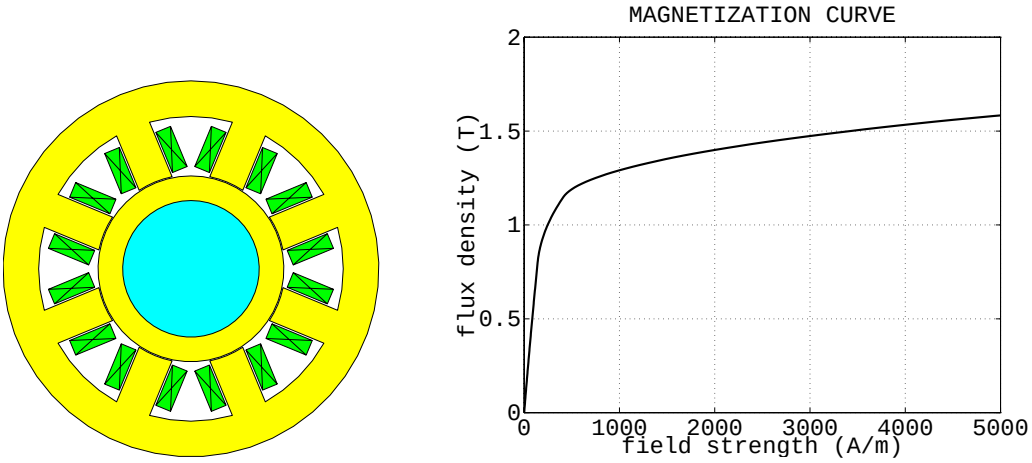

Figure C1. The radial bearing geometry on the left and the magnetization curve on the right.

The rotor geometry and the first two bending modes are shown in Figure C2.

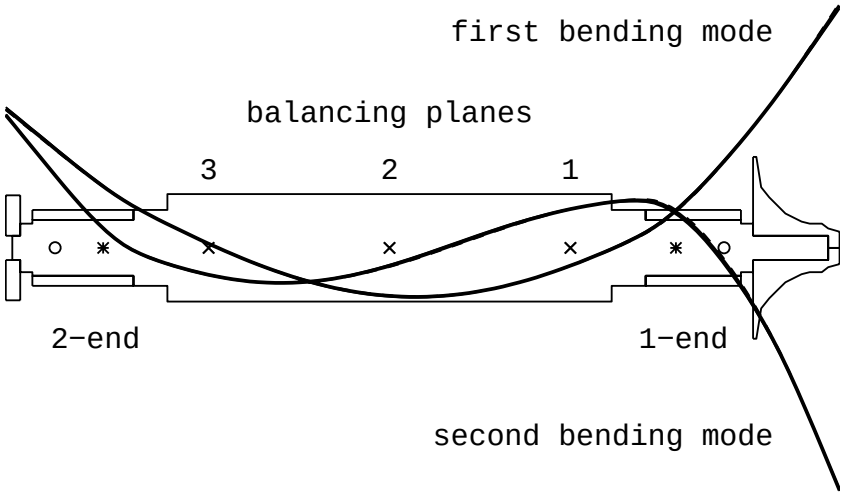

Figure C2. The rotor geometry. The mode shapes are computed for zero speed and at a maximum speed 540 Hz. The forward and backward modes are shown even though they cannot be distinguished from the zero speed mode shapes.

The rotor weight is 79.6 kg. The matrices of the rotordynamic model (Lantto 1997) are the following

$$\boldsymbol{M}_{\text{rot}} = \text{diag}\{79.6, 4.75, 3.84, 2.27\},$$

$$\boldsymbol{K}_{\text{rot}} = \text{diag}\left\{0, 0, 64.5 * 10^{6}, 127 * 10^{6}\right\},$$

$$\boldsymbol{D}_{\text{rot}} = \text{diag}\{0, 0, 64, 69\},$$

$$\boldsymbol{G}_{\text{rot}} = \begin{bmatrix} 0 & 0 & 0 & 0 \\ 0 & 0.152 & 0.006 & 0.040 \\ 0 & 0.006 & 0.368 & 0.086 \\ 0 & 0.040 & 0.086 & 0.421 \end{bmatrix}, \boldsymbol{B}_{\text{b}} = \begin{bmatrix} 1 & 1 \\ 0.344 & -0.365 \\ 0.153 & 0.252 \\ -0.148 & -0.080 \end{bmatrix},$$

$$\boldsymbol{B}_{\text{bal}} = \begin{bmatrix} 1 & 1 & 1 \\ 0.21 & -0.01 & -0.23 \\ -0.07 & -0.20 & 0.02 \\ -0.16 & 0.07 & 0.11 \end{bmatrix}, \quad \boldsymbol{C}_{\text{S}} = \begin{bmatrix} 1 & 0.404 & 0.354 & 0.055 \\ 1 & -0.425 & 0.406 & -0.297 \end{bmatrix}, \tag{C1}$$

where $\boldsymbol{M}_{\text{rot}}$ is the modal mass matrix,
$\boldsymbol{K}_{\text{rot}}$ is the modal stiffness matrix,
$\boldsymbol{D}_{\text{rot}}$ is the modal damping matrix,
$\boldsymbol{G}_{\text{rot}}$ is the gyroscopic matrix,
$\boldsymbol{B}_{\text{b}}$ is the bearing force to generalized force transformation matrix,
$\boldsymbol{B}_{\text{bal}}$ is the balancing plane force to generalized force transformation matrix and
$\boldsymbol{C}_{\text{S}}$ is the generalized coordinates to displacements transformation matrix.